Shock and Vibration

Wave-induced Structural Vibrations and Water Impacts of Ships and Marine Structures

Lead Guest Editor: Jialong Jiao
Guest Editors: Pengyao Yu and Spyros Hirdaris

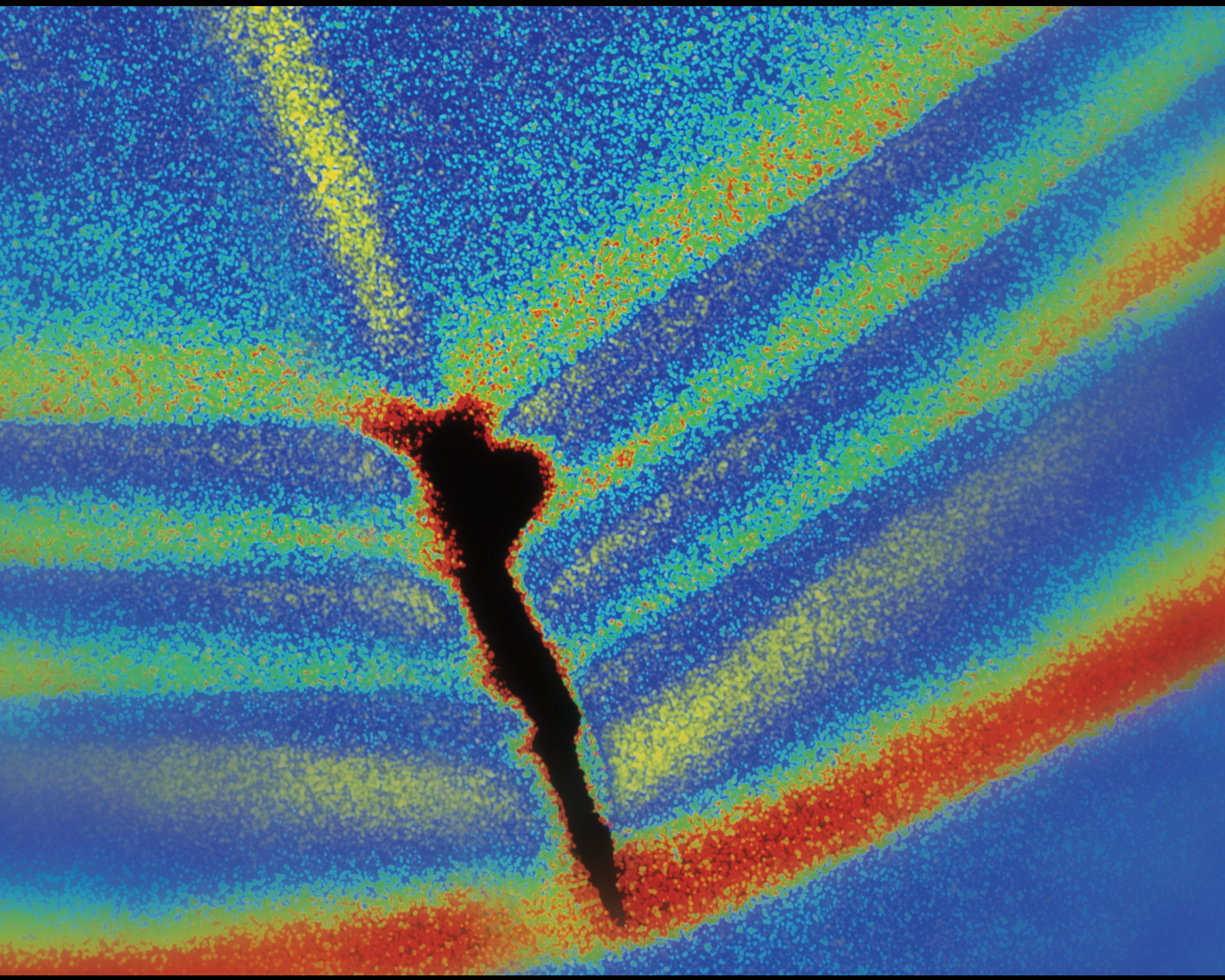

Wave-induced Structural Vibrations and Water Impacts of Ships and Marine Structures

Shock and Vibration

Wave-induced Structural Vibrations and Water Impacts of Ships and Marine Structures

Lead Guest Editor: Jialong Jiao
Guest Editors: Pengyao Yu and Spyros Hirdaris

Copyright © 2022 Hindawi Limited. All rights reserved.

This is a special issue published in “Shock and Vibration.” All articles are open access articles distributed under the Creative Commons Attribution License, which permits unrestricted use, distribution, and reproduction in any medium, provided the original work is properly cited.

Chief Editor

Huu-Tai Thai, Australia

Associate Editors

Ivo Caliò, Italy
Nawawi Chouw, New Zealand
Longjun Dong, China
Farzad Ebrahimi, Iran
Mickaël Lallart, France
Vadim V. Silberschmidt, United Kingdom
Mario Terzo, Italy
Angelo Marcelo Tusset, Brazil

Academic Editors

Omid A. Yamini, Iran
Maher Abdelghani, Tunisia
Haim Abramovich, Israel
Desmond Adair, Kazakhstan
Manuel Aenlle Lopez, Spain
Brij N. Agrawal, USA
Ehsan Ahmadi, United Kingdom
Felix Albu, Romania
Marco Alfano, Italy
Sara Amoroso, Italy
Huaming An, China
P. Antonaci, Italy
José V. Araújo dos Santos, Portugal
Lutz Auersch, Germany
Matteo Aureli, USA
Azwan I. Azmi, Malaysia
Antonio Batista, Brazil
Mattia Battarra, Italy
Marco Belloli, Italy
Francisco Beltran-Carbajal, Mexico
Denis Benasciutti, Italy
Marta Berardengo, Italy
Sébastien Besset, France
Giosuè Boscato, Italy
Fabio Botta, Italy
Giuseppe Brandonisio, Italy
Francesco Bucchi, Italy
Rafał Burdzik, Poland
Salvatore Caddemi, Italy
Wahyu Caesarendra, Brunei Darussalam
Baoping Cai, China
Sandro Carbonari, Italy
Cristina Castejón, Spain
Nicola Caterino, Italy
Gabriele Cazzulani, Italy
Athanasios Chasalevris, Greece
Guoda Chen, China
Xavier Chiementin, France
Simone Cinquemani, Italy
Marco Civera, Italy
Marco Cocconcelli, Italy
Alvaro Cunha, Portugal
Giorgio Dalpiaz, Italy
Thanh-Phong Dao, Vietnam
Arka Jyoti Das, India
Raj Das, Australia
Silvio L.T. De Souza, Brazil
Xiaowei Deng, Hong Kong
Dario Di Maio, The Netherlands
Raffaella Di Sante, Italy
Luigi Di Sarno, Italy
Enrique Lopez Droguett, Chile
Mădălina Dumitriu, Romania
Sami El-Borgi, Qatar
Mohammad Elahinia, USA
Said Elias, Iceland
Selçuk Erkaya, Turkey
Gaoliang Fang, Canada
Fiorenzo A. Fazzolari, United Kingdom
Luis A. Felipe-Sese, Spain
Matteo Filippi, Italy
Piotr Folęga, Poland
Paola Forte, Italy
Francesco Franco, Italy
Juan C. G. Prada, Spain
Roman Gabl, United Kingdom
Pedro Galvín, Spain
Jinqiang Gan, China
Cong Gao, China
Arturo García Garcia-Perez, Mexico
Rozaimi Ghazali, Malaysia
Marco Gherlone, Italy
Anindya Ghoshal, USA
Gilbert R. Gillich, Romania
Antonio Giuffrida, Italy
Annalisa Greco, Italy
Jiajie Guo, China

Amal Hajjaj, United Kingdom
Mohammad A. Hariri-Ardebili, USA
Seyed M. Hashemi, Canada
Xue-qiu He, China
Agustin Herrera-May, Mexico
M.I. Herreros, Spain
Duc-Duy Ho, Vietnam
Hamid Hosano, Japan
Jin Huang, China
Ahmed Ibrahim, USA
Bernard W. Ikua, Kenya
Xingxing Jiang, China
Jiang Jin, China
Xiaohang Jin, China
MOUSTAFA KASSEM, Malaysia
Shao-Bo Kang, China
Yuri S. Karinski, Israel
Andrzej Katunin, Poland
Manoj Khandelwal, Australia
Denise-Penelope Kontoni, Greece
Mohammadreza Koopialipoor, Iran
Georges Kouroussis, Belgium
Genadijus Kulvietis, Lithuania
Pradeep Kundu, USA
Luca Landi, Italy
Moon G. Lee, Republic of Korea
Trupti Ranjan Lenka, India
Arcanjo Lenzi, Brazil
Marco Lepidi, Italy
Jinhua Li, China
Shuang Li, China
Zhixiong Li, China
Xihui Liang, Canada
Tzu-Kang Lin, Taiwan
Jinxin Liu, China
Ruonan Liu, China
Xiuquan Liu, China
Siliang Lu, China
Yixiang Lu, China
R. Luo, China
Tianshou Ma, China
Nuno M. Maia, Portugal
Abdollah Malekjafarian, Ireland
Stefano Manzoni, Italy
Stefano Marchesiello, Italy
Francesco S. Marulo, Italy
Traian Mazilu, Romania
Vittorio Memmolo, Italy
Jean-Mathieu Mencik, France
Laurent Mevel, France
Letícia Fleck Fadel Miguel, Brazil
FuRen Ming, China
Fabio Minghini, Italy
Marco Miniaci, USA
Mahdi Mohammadpour, United Kingdom
Rui Moreira, Portugal
Emiliano Mucchi, Italy
Peter Múčka, Slovakia
Fehmi Najar, Tunisia
M. Z. Naser, USA
Amr A. Nassr, Egypt
Sundararajan Natarajan, India
Toshiaki Natsuki, Japan
Miguel Neves, Portugal
Sy Dzung Nguyen, Republic of Korea
Trung Nguyen-Thoi, Vietnam
Gianni Niccolini, Italy
Rodrigo Nicoletti, Brazil
Bin Niu, China
Leilei Niu, China
Yan Niu, China
Lucio Olivares, Italy
Erkan Oterkus, United Kingdom
Roberto Palma, Spain
Junhong Park, Republic of Korea
Francesco Pellicano, Italy
Paolo Pennacchi, Italy
Giuseppe Petrone, Italy
Evgeny Petrov, United Kingdom
Franck Poisson, France
Luca Pugi, Italy
Yi Qin, China
Virginio Quaglini, Italy
Mohammad Rafiee, Canada
Carlo Rainieri, Italy
Vasudevan Rajamohan, India
Ricardo A. Ramirez-Mendoza, Mexico
José J. Rangel-Magdaleno, Mexico

Didier Rémond, France
Dario Richiedei, Italy
Fabio Rizzo, Italy
Carlo Rosso, Italy
Riccardo Rubini, Italy
Salvatore Russo, Italy
Giuseppe Ruta, Italy
Edoardo Sabbioni, Italy
Pouyan Roodgar Saffari, Iran
Filippo Santucci de Magistris, Italy
Fabrizio Scozzese, Italy
Abdullah Seçgin, Turkey
Roger Serra, France
S. Mahdi Seyed-Kolbadi, Iran
Yujie Shen, China
Bao-Jun Shi, China
Chengzhi Shi, USA
Gerardo Silva-Navarro, Mexico
Marcos Silveira, Brazil
Kumar V. Singh, USA
Jean-Jacques Sinou, France
Isabelle Sochet, France
Alba Sofi, Italy
Jussi Sopanen, Finland
Stefano Sorace, Italy
Andrea Spaggiari, Italy
Lei Su, China
Shuaishuai Sun, Australia
Fidelis Tawiah Suorineni, Kazakhstan
Cecilia Surace, Italy
Tomasz Szolc, Poland
Iacopo Tamellin, Italy
Zhuhua Tan, China
Gang Tang, China
Chao Tao, China
Tianyou Tao, China
Marco Tarabini, Italy
Hamid Toopchi-Nezhad, Iran
Carlo Trigona, Italy
Federica Tubino, Italy
Nerio Tullini, Italy
Nicolò Vaiana, Italy
Marcello Vanali, Italy
Christian Vanhille, Spain
Dr. Govind Vashishtha, Poland
F. Viadero, Spain
M. Ahmer Wadee, United Kingdom
C. M. Wang, Australia
Gaoxin Wang, China
Huiqi Wang, China
Pengfei Wang, China
Weiqiang Wang, Australia
Xian-Bo Wang, China
YuRen Wang, China
Wai-on Wong, Hong Kong
Yuanping XU, China
Biao Xiang, China
Qilong Xue, China
Xin Xue, China
Diansen Yang, China
Jie Yang, Australia
Chang-Ping Yi, Sweden
Nicolo Zampieri, Italy
Chao-Ping Zang, China
Enrico Zappino, Italy
Guo-Qing Zhang, China
Shaojian Zhang, China
Yongfang Zhang, China
Yaobing Zhao, China
Zhipeng Zhao, Japan
Changjie Zheng, China
Chuanbo Zhou, China
Hongwei Zhou, China
Hongyuan Zhou, China
Jiaxi Zhou, China
Yunlai Zhou, China
Radoslaw Zimroz, Poland

Contents

Hindawi
Shock and Vibration
Volume 2022, Article ID 2068218, 11 pages
https://doi.org/10.1155/2022/2068218

Research Article

An Efficient Noise Elimination Method for Non-stationary and Non-linear Signals by Averaging Decomposed Components

Zhenzhou Sun,[1,2] Hongchao Lu,[3] Jiefeng Chen,[1,2] and Jialong Jiao[3,4]

[1]*Key Laboratory of Far-shore Wind Power Technology of Zhejiang Province, Hangzhou 311122, China*
[2]*Renewable Energy Engineering Institute, Power China Huadong Engineering Corporation, Hangzhou 311122, China*
[3]*School of Civil Engineering and Transportation, South China University of Technology, Guangzhou 510641, China*
[4]*State Key Laboratory of Coastal and Offshore Engineering, Dalian University of Technology, Dalian 116024, China*

Correspondence should be addressed to Hongchao Lu; luhclhc@scut.edu.cn and Jialong Jiao; jiaojl@scut.edu.cn

Received 5 October 2021; Revised 16 April 2022; Accepted 20 April 2022; Published 21 May 2022

Academic Editor: Abdollah Malekjafarian

Copyright © 2022 Zhenzhou Sun et al. This is an open access article distributed under the Creative Commons Attribution License, which permits unrestricted use, distribution, and reproduction in any medium, provided the original work is properly cited.

In this paper, a moving-average method of smoothing noise based on complex exponential decomposition is applied to eliminate noise of a non-stationary signal and a non-linear signal produced by Bouc–Wen model, which are added to white Gaussian noise to simulate the noise in measured signal. The method uses a sliding window cutting the entire non-stationary and/or non-linear signal into small segments and considers that the small segments are stable and linear. The segments are decomposed into a series of components via complex exponential decomposition, and the high-energy components are reserved to reconstruct de-noised signal. Then, due to the overlap of the reconstructed segments, the average value at the same time point of reconstruction signal is regarded as the de-noised data. A non-stationary signal and a non-linear signal are selected to investigate the performance of the proposed method, the results show that the proposed method has better de-noising efficiency compared with the wavelet shrinkage method and the Savitzky–Golay filter method based on EMD (EMD-SG) for dealing with the signals with SNR of 10 dB, 15 dB, and 20 dB, and de-noised signal using the proposed method has the highest signal-to-noise ratio (SNR) and the least root mean square error (RMSE).

1. Introduction

Vibration monitoring is an important method to obtain information of operating conditions of structure, which is commonly used in mechanical engineering, and can be applied to research the vibration performance of mechanical device and monitor possible damage of structure and so on [1–5]. However, noise is an inevitable part existing in measured vibrating response data, which is induced by many factors, such as the processes generated by local and intermittent instabilities, the concurrent phenomena in the environment of data test, and the sensors, and recording systems [6]. Figure 1 shows the measured vibrating signal of an offshore substation located at the East China Sea, which indicates that the noise is obvious. The noise presenting in signal may affect the accuracy of analysis result seriously. After obtaining the vibrating data of vibrating systems, the information of the systems should be further extracted. Hilbert–Huang transform is a commonly used signal processing method, which is widely applied to deal with the vibrating signal of non-linear and time-varying system [7–9]. Empirical mode decomposition (EMD) is essential when implementing Hilbert-Huang transform, which is vulnerable for noise [10]. The study of bearing damage shows that the accuracy can be severely limited by noise [11]. Therefore, data pretreatment of de-noising is necessary to obtain accurate result of analysis when the signal is contaminated by noise.

In many applications, signal de-noising is the process of estimating the uncontaminated signal from measured data. The estimated signal should be as close as possible to the original one and contain most of its important properties [12]. Traditional de-noising schemes are usually based on linear methods, the Fourier filters are commonly used to

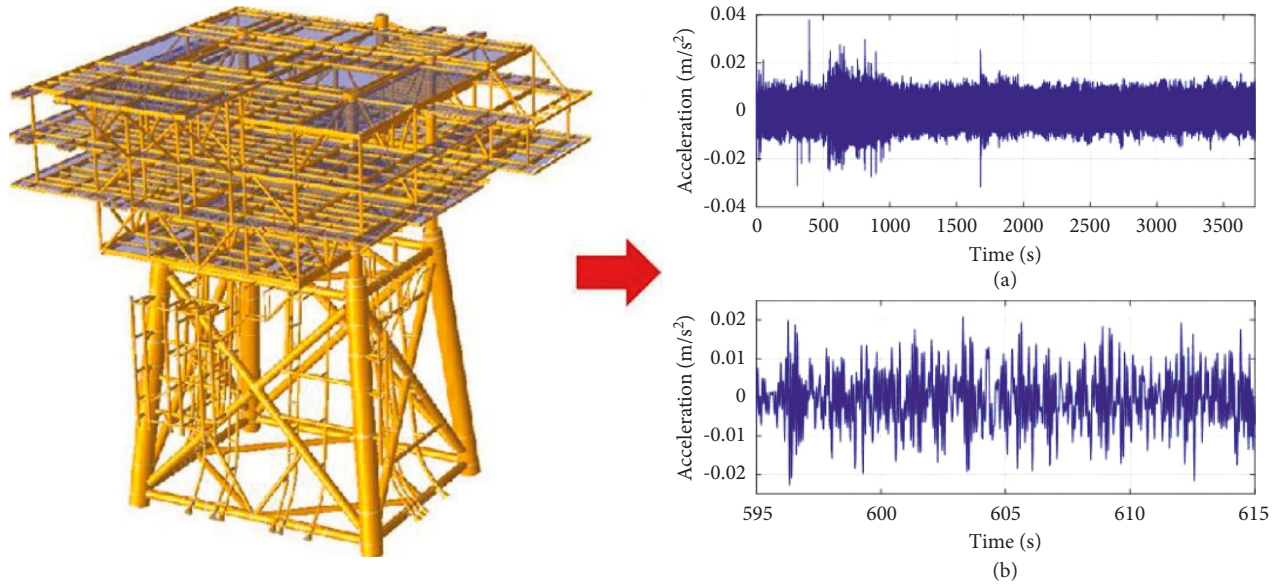

Figure 1: Measured vibrating signal of offshore substation: (a) model of offshore substation; (b) measured vibrating signal.

separate the noise from the measured signal when the data generation processes are linear and the noises have distinct time or frequency scales different from the true signal [13]. Wiener filter is another frequently used linear de-noising method, which adopts minimum value of mean square error between estimated random process and desired process as an optimal criterion [14]. Linear de-noising methods are easy to implement and to design, but they have limitations as well. The methods are not effective when signals have sharp edges and impulses in short duration [12]. Furthermore, filter methods will be failed when the processes are either non-linear or non-stationary because the filter methods are based on linear theory. One adverse effect is mixing when using filter methods to deal with non-linear signal, even though the real signal and the noises have distinct fundamental frequencies. The mixing of harmonics with noises will lead to terrible results of noise separation. Under such conditions, many non-linear de-nosing methods are proposed, especially for the methods based on wavelet thresholding and EMD. The wavelet method considers that the energy of a signal will commonly focus on a few coefficients in wavelet domain while the energy of noise is spread among all coefficients, which are relatively small in general. Donoho [15, 16] proposed the hard and soft thresholding methods for de-noising based on wavelet transform, where the former reserves coefficients if their magnitudes are larger than a given threshold, or makes other coefficients zero, while the latter just shrinks coefficients whose magnitudes are larger than threshold to zero by the threshold value. The methods are widely used to de-noising and have good results. However, the drawbacks of the hard and soft thresholding methods are obvious. The obtained coefficients using hard thresholding are discontinuous at threshold value, which may lead to the reconstruction signal oscillating. The latter makes coefficients used to reconstruct signal different from original coefficients with permanent bias, which influences the degree of the closeness between reconstructed and true signals, and brings unavoidable errors. Besides, the basis functions of wavelet approaches are fixed, which do not necessarily match the varying natures of signals.

EMD is an adaptive method proposed by Huang et al. [17], which can decompose any complicated data into a finite and often small number of intrinsic mode functions (IMFs). The IMFs become the basis representing the data, which offer a physically meaningful representation of the underlying processes. The basis functions are extracted from the original data, which means the analysis is adaptive. Since the basis is adaptive, EMD is ideally applicable to the measured data from non-linear and non-stationary processes. The sifting process of EMD starts from high frequency modes to low frequency modes with various intrinsic time scales, which signifies that the first IMFs are dominated by noise than the last ones if the analyzed signal contains noise. Based on the properties of EMD, Boudraa et al. [12] proposed a de-noising method combining with thresholding. The method of eliminating noise is based on estimated IMFs, which are obtained from sifted IMFs from original signal and threshold value. After obtaining the estimated IMFs of signal, the de-noising process is implemented by reconstructing the estimated IMFs. In addition, Flandrin et al. [18] implemented numerical experiments based on fractional Gaussian noise to understand the way of EMD behaves in stochastic situations related to broadband. Wu and Zhang [6] indicated that the EMD was an effective dyadic filter with the ability of separating the white noise into IMF components, which have mean periods exactly twice the value of the previous components. Ensemble EMD (EEMD) is a noise-assisted technique, which is applied to attenuate mode mixing and noise to some extent [19]. Rehman and Mandic [20] further investigated the behavior of EEMD in the presence of white Gaussian noise. Li and Wang [21] proposed a novel noise reduction method based on complete

EEMD, which was applied to deal with underwater acoustic signals and obtained good results. Li et al. [22] proposed a time-varying filter to implement EMD, which is robust against noise interference. Excluding the methods based on EMD, Iqbal et al. [23, 24] proposed de-noising methods based on singular value decomposition technique, which achieved promising results.

The purpose of this paper is to propose a more suitable de-noising method to deal with non-stationary and non-linear signal corrupted by noise. The method has a better de-noising efficiency and stable performance in different noise levels. In the process of de-noising using the proposed method, the original non-stationary and non-linear signal is cut into small segments, and the segments are assumed to be stable and linear. The noises in the small segments are eliminated via signal decomposition and reconstruction. Two numerical examples, a non-stationary signal and a non-linear signal produced by Bouc–Wen model, are used to investigate the performance of the proposed method, which show that the proposed method can eliminate added Gaussian white noise efficiently.

2. Preliminaries

Noise is inevitably exiting in all kinds of measured signals, which may be caused by a number of factors. As a result, the collected data are always described as an amalgamation of true signal and noise, which can be expressed as follows:

$$y(t) = s(t) + n(t), \tag{1}$$

where $y(t)$ is the observed signal corrupted by noise, $s(t)$ is the true signal, and $n(t)$ is the noise.

2.1. Wavelet Shrinkage Method. A measurable square integral function space $L^2(R)$ on the real axis should be defined to carry out the wavelet transform of a signal. Then, the continuous wavelet transform of a signal $f(t) \in L^2(R)$ can be expressed as follows:

$$WT(a,b) = |a|^{-1/2} \int_{-\infty}^{\infty} y(t) \psi^* \left(\frac{t-b}{a} \right) \mathrm{d}t, \tag{2}$$

where a is a temporal scale factor which reflects the periodic length of a wavelet, b is a time position factor, $\psi * (t)$ is the complex conjugate of wavelet function, and $WT(a, b)$ are the so-called wavelet coefficients.

The wavelet shrinkage method was proposed by Donoho [16], which is implemented by the following steps: Step 1: Selecting an appropriate wavelet function and decomposition level, the wavelet coefficients of signal corrupted by noise are obtained by applying wavelet decomposition using selected parameters; Step 2: Choosing a suitable threshold of wavelet coefficient τ, the obtained coefficients in Step 1 are sifted by the threshold, which includes soft-threshold and hard-threshold; Step 3: The obtained coefficients sifted by the threshold are reconstructed to eliminate the noises in signal.

2.2. Savitzky – Golay Filter Method Based on EMD. EMD is an adaptive signal analysis method first proposed by Huang et al. [17], which can be used to deal with non-linear and non-stationary signals because of the adaptive nature of the basis. The formula of EMD is expressed as follows:

$$y(t) = \sum_{i=1}^{N} \mathrm{IMF}_i(t) + r(t), \tag{3}$$

where i is the decomposition order, IMF$i(t)$ is the ith IMF, and $r(t)$ is the residue.

The Savitzky–Golay filter method is a time-domain smoothing method, which uses least squares approach to replace the original signal points with the fitted polynomial. Boudraa [12] combined the EMD and SavitzkyGolay filter (EMD-SG) to eliminate the noises in measured signal. The method decomposes the signal corrupted by noise into a series of IMFs using (3), smooths each IMFs applying SavitzkyGolay filter, and then uses the smoothing IMFs to reconstruct de-noised signal.

3. Moving-Average Method of Smoothing Noisy Signal Based on Complex Exponential Decomposition

3.1. Signal Partition Using Sliding Window and Decomposition. For a non-stationary or/and non-linear signal, it is hard to use invariant parameters to describe the signal. One solving method is dividing the signal into litter fragments and considering that the signal segments are stationary and linear. Then, the linear method is applied to deal with the de-noising problem of small fragments. Denoting the sampling interval as Δt, $t_k = k\Delta t$, the discrete digital signal y_k with $k = 0, 1, \ldots, N-1$ can be cut into small fragments using a rectangular window. To guarantee the continuity of the signal in the process of noise elimination using the proposed method, the step of sliding window is set as 1. Then, the small fragments can be expressed as

$$y_{m,n} = y_{m+n-1}, \tag{4}$$

where m is the number of signal fragments, $m = 1, 2, \ldots, N - L + 1$, and L is the length of each signal fragment; n is the number of fragments, $n = 0, 1, \ldots, L - 1$.

The obtained segment $y_{m,n}$ can be decomposed into a sum of exponential form with real-valued and/or complex-valued exponents, which is so-called Prony series expressed as follows [25]:

$$y_{m,n} = \sum_{l=1}^{p_m} \gamma_{m,l} z_{m,l}^n, \tag{5}$$

where p_m is the number of terms corresponding to segment $y_{m,n}$, $z_{m,l} = e^{\lambda_{m,l}\Delta t}$. Since $y_{m,n}$ is a real-valued signal, $\lambda_{m,l}$ must either be real numbers or occur in complex conjugate pairs and $\gamma_{m,l}$ have the same corresponding form. Let $\lambda_{m,l} = -\alpha_{m,l} + \mathrm{j}2\pi f_{m,l}$, then $\alpha_{m,l}$ is the damping factor in seconds -1 and $f_{m,l}$ is the frequency in Hertz; j is imaginary unit. Let $\gamma_{m,l} \equiv A_{m,l} e^{\mathrm{j}\theta_{m,l}}$, then $A_{m,l}$ is the amplitude and $\theta_{m,l}$ is the sinusoidal initial phase in radians associated with $e^{\lambda_{m,l}t}$.

3.2. Parameters Estimation of Prony Series. Obviously, the discrete Prony series in (5) can be viewed as the general solution of a pth-order difference equation as follows:

$$\sum_{l=0}^{p_m} a_{m,l} y_{m,n+l} = 0 \quad for\, n = 0, 1, \ldots, L - p_m - 1, \tag{6}$$

where $a_{m,l}$ are real-valued constants. Without losing the generality, let $a_{m,p_m} = 1$. The characteristic equation corresponded to (6) can be expressed as follows:

$$\sum_{l=0}^{p_m} a_{m,l} z^l = 0. \tag{7}$$

As discussed in reference [25], an ill-conditioned problem would occur in the solution process of (6) using the direct method. One method of dealing with the ill-conditioned problem is converting the high-order difference equation to a first-order matrix difference equation. Thus, new auxiliary variables are introduced as follows [26]:

$$x_{1m,n} = y_{m,n}, x_{2m,n} = y_{m,n+1}, \ldots, x_{p_m m,n} = y_{m,n+p_m-1}. \tag{8}$$

Then, a first-order matrix difference equation equivalent to (6) can be obtained as follows:

$$\mathbf{x}_{m,n+1} = \mathbf{G}_m \mathbf{x}_{m,n}, \tag{9}$$

where

$$\mathbf{G}_m = \begin{bmatrix} 0 & 1 & 0 & 0 & \cdots & 0 & 0 \\ 0 & 0 & 1 & 0 & \cdots & 0 & 0 \\ 0 & 0 & 0 & 1 & \cdots & 0 & 0 \\ \vdots & \vdots & \vdots & \vdots & \ddots & \vdots & \vdots \\ 0 & 0 & 0 & 0 & \cdots & 0 & 1 \\ -a_{m,0} & -a_{m,1} & -a_{m,2} & -a_{m,3} & \cdots & -a_{m,p_m-2} & -a_{m,p_m-1} \end{bmatrix} \in R^{p_m \times p_m}. \tag{10}$$

and

$$\mathbf{x}_{m,n} = \begin{bmatrix} x_{1m,n} & x_{2m,n} & \cdots & x_{p_m m,n} \end{bmatrix}^T \in R^{p_m \times 1}. \tag{11}$$

Mathematically, the p_m roots of the characteristic equation of (7) are exactly corresponding to the p_m eigenvalues of the matrix G_m. To avoid ill-condition problem, the eigenvalue analysis of matrix G_m is implemented to determine the roots of (7).

To compute eigenvalues of matrix G_m, a Hankel matrix is introduced, which is defined as follows:

$$\mathbf{H}_m(1) = \begin{bmatrix} y_{m,k} & y_{m,k+1} & \cdots & y_{m,k+\eta-1} \\ y_{m,k+1} & y_{m,k+2} & \cdots & y_{m,k+\eta} \\ \vdots & \vdots & \ddots & \vdots \\ y_{m,k+\xi-1} & y_{m,k+\xi} & \cdots & y_{m,k+\xi+\eta-2} \end{bmatrix}, \tag{12}$$

where ξ and η are the selected row and column of the Hankel matrix.

Substituting $k = 0$ into (12) and implementing the singular value decomposition of $H_m(0)$, one can obtain [27]

$$\mathbf{H}_m(0) = \begin{bmatrix} \mathbf{U}_{m,1} & \mathbf{U}_{m,2} \end{bmatrix} \begin{bmatrix} \mathbf{\Sigma}_{m,1} & 0 \\ 0 & 0 \end{bmatrix} \begin{bmatrix} \mathbf{V}_{m,1}^T \\ \mathbf{V}_{m,2}^T \end{bmatrix} = \mathbf{U}_{m,1} \mathbf{\Sigma}_{m,1} \mathbf{V}_{m,1}^T. \tag{13}$$

In theory, the number of non-zero singular values in (7) is equal to p_m, $\mathbf{U}_{m,1} \in R^{\xi \times p}$, $\Sigma_{m,1} \in R^{p \times p}$ and $V_{m,1} \in R^{\eta \times p}$. While noise exists in the signal, the number of non-zero singular values is larger than p_m. Because of the singular values sorting from largest to smallest, the first pm singular values are regarded as corresponding to the real signal and other singular values are set as zero, which is the de-noising approach of the proposed method.

Letting $k = 1$, $\mathbf{H}_m(1)$ can be expressed as follows [25]:

$$\mathbf{H}_m(1) = \mathbf{U}_{m,1} \mathbf{\Sigma}_{m,1}^{\frac{1}{2}} \mathbf{A}_m \mathbf{\Sigma}_{m,1}^{\frac{1}{2}} \mathbf{V}_{m,1}^T. \tag{14}$$

Then, a realization of system matrix is yielded as follows:

$$\mathbf{A}_m = \mathbf{\Sigma}_{m,1}^{\frac{-1}{2}} \mathbf{U}_{m,1}^T \mathbf{H}_m(1) \mathbf{V}_{m,1} \mathbf{\Sigma}_{m,1}^{\frac{-1}{2}}. \tag{15}$$

While the calculated eigenvalues of $\mathbf{A}_m$ are $\widehat{z}_{m,l}$, $l = 1, 2, \ldots, p_m$, the corresponding $\widehat{\lambda}_{m,l}$ are estimated using $\widehat{\lambda}_{m,l} = \ln(\widehat{z}_{m,l})/\Delta t$. Substituting $\widehat{\lambda}_{m,l}$ into (5), the corresponding $\widehat{\gamma}_{m,l}$ can be obtained.

3.3. Noise Elimination Using Moving-Average Method Based on the Estimated Parameters. When the parameters of Prony series are obtained, each de-noised signal segments are reconstructed by (5).

$$\widehat{y}_{m,n} = \sum_{l=1}^{p_m} \widehat{\gamma}_{m,l} e^{\widehat{\lambda}_{m,l} n \Delta t}. \tag{16}$$

With the sliding window moving, the noises in small segments are eliminated. Due to the step of sliding window is 1, the overlap of post-segment and pre-segment is L–1. For the whole duration signal, the reconstructed segments at the same time point should be calculated average, which is the de-noised data at the time point. When the sliding window moves across the entire signal, the de-noised signal $\widehat{y}_k$ with $k = 0, 1, \ldots, N$–1 is obtained.

4. Example Studies

In this paper, two different numerical examples are applied to test the performance of the proposed de-noising method. The process and de-noising results are exhibited in detail.

4.1. Test Case 1: Non-stationary Example. In this example, a non-stationary signal is chosen to investigate the performance of proposed method. The frequency of the non-stationary signal is time varying, which is synthesized using the following formula [22]:

$$y(t) = \cos\left(20\pi t + 4\pi t^2\right) + \cos\left(4\pi t + 4\pi t^2\right). \tag{17}$$

To investigate the capability of the proposed de-noising method, the different levels of noise are added to the non-stationary signal, which is simulated using the additive model as follows:

$$y_{noi}(t) = y(t) + y_N(t), \tag{18}$$

where $y_{noi}(t)$ is the signal contaminated by noise, $y(t)$ is the clear signal, and $y_N(t)$ is the noise signal exiting in the measured signal.

For testing purposes, the white Gaussian noise is added to the clear signal to simulate the test noise of measured signal. The signal-to-noise ratios (SNRs) are set as 10 dB, 15 dB, and 20 dB. With the sampling interval $\Delta t = 0.001$ s and the number of simulation points $N = 5120$, the discrete signals with total duration of 5.12 s are obtained. For simplicity, the signal with an SNR of 10 dB is shown in Figure 2, the upper part is clear signal compared with noise signal, and the bottom part is the clear signal compared with the signal corrupted by noise.

Typically, the wavelet shrinkage and EMD-SG methods are implemented to eliminate the noise embedded in the non-stationary signal as comparisons. Hard thresholding is selected as shrinkage rule in this example, and sym8 wavelet at level 10 is applied when using wavelet shrinkage to eliminate the noise in the signal. Implementing EMD to the non-stationary signal corrupted by noise, 11 IMFs can be obtained. The SavitzkyGolay smoothing filter is applied to each IMF with an order of 5 and a frame length of 21. The comparison of de-noised signals using above two methods and clear signals is exhibited in Figure 3 (SNR = 10 dB). The figure shows that the two methods are able to smooth the embedded noise of the non-stationary signal, but the discrepancies are obvious compared with the clear signal.

To illuminate the proposed de-noising method, the comparison diagrams between clear signal and de-noised signals with the three noise levels are exhibited in Figures 4–6. When using the proposed method to deal with the signal with an SNR of 10 dB, the length of moving window is set as 160, which means that the duration of moving window used to select data is 1.6 s and the segments are regarded as linear and stationary in the procedure. With movement of the window, the non-stationary is cut into small segments, which are decomposed as linear and stationary signal. Applying Prony decomposition to the small segments and reconstructing the signal using reserved $\lambda_{m,l}$ and $\gamma_{m,l}$, the noise is removed in the procedure of decomposition and reconstruction. To demonstrate the computational efficiency of the proposed method, the elapsed time of canceling noise process is recorded. For the signal corrupted by the noise with an SNR of 10 dB, the elapsed time is 69.7 s (CPU Inter Core i7-8700, 3.2 GHz). Enlarging the de-noised signal during 3.5 s to 3.7 s, the details show that the de-noised signals using the proposed method match well with the original signals under the influence of noises with SNRs of 10 dB, 15 dB, and 20 dB.

EMD is an adaptive data analysis method, which is widely used for non-stationary and non-linear signals. However, EMD is sensitive to noise. To analyze the efficiency of proposed method further, the de-noised signal containing noise with 15 dB is decomposed into a series IMFs using EMD. The first three IMFs are extracted because the low-order IMFs contain the main information of signal. Comparing the first three IMFs of the clear and de-noised signals, the results indicated that the first IMFs match with each other well and the second and third IMFs have small discrepancies, which are shown in Figure 7.

To quantify the de-noising efficiency, the SNR and root mean square error (RMSE) are introduced as criteria to estimate the efficiency of noise reduction. Before de-noising, the SNR of the three signals are 10 dB, 15 dB, and 20 dB. The SNR and RMSE of de-noised signals using the three methods are listed in Table 1. It indicates that the SNR of de-noised signal using proposed method is maximal and the corresponding RMSE is minimal under different noise levels. Compared with the signal contaminated noise with the SNRs of 10 dB, 15 dB, and 20 dB, the SNRs are increased by 14.724 dB, 14.428 dB, and 14.688 dB using proposed method, and the corresponding RMSEs have reductions of 53.56%, 51.99%, and 53.54% compared with the better traditional method (EMD-SG), which suggests that the de-noising efficiency of proposed method is obvious.

4.2. Test Case 2: Non-Linear Example. Bouc–Wen model is a typical non-linear model to describe hysteretic phenomena, and it is encountered in many scientific fields. For example, hysteretic behavior of engineering structures often shows up under severe cyclic loads such as earthquakes, high winds, and waves. In this example, a Bouc–Wen model is selected to investigate the performance of the proposed method dealing with non-linear signal contaminated by noise since it is widely used. The following set of differential equations describes the motion of a single degree of freedom (SDOF) system with Bouc–Wen hysteresis:

$$\begin{cases} \ddot{x}(t) + 2\zeta\omega\dot{x}(t) + \gamma\omega^2 x(t) + (1-\gamma)\omega^2 z(t) = f(t), \\ \dot{z}(t) = A\dot{x}(t) - \alpha|\dot{x}(t)|z(t)|z(t)|^{n-1} - \beta\dot{x}(t)|z(t)|^n, \end{cases} \tag{19}$$

where $x(t)$, $\dot{x}(t)$ and $\ddot{x}(t)$ are the displacement, velocity, and acceleration, respectively; ζ is the damping; ω is the natural frequency; γ is the ratio of post-yield to pre-yield stiffness; $f(t)$ is the external excitation acts on the system; $z(t)$ is the hysteretic displacement; and A, n, α, β are the parameters to regulate shape of the hysteresis loop.

Letting $A = 1$, $n = 3$, $\alpha = 2.1$, $\beta = 1$, the frequency $\omega = 3$, damping $\zeta = 0.15$, and assuming that the external exaction is harmonic, $f(t) = 10\cos(0.5\,\mathrm{t})$ in this example, the response of the Bouc–Wen model governed by (19) can be calculated using Runge–Kutta method. With the calculation step $\Delta t = 0.01$ s and the number of computation points $N = 10000$, the response of the Bouc–Wen model with total duration of 100 s is obtained. The hysteretic loop of the system is shown as Figure 8, which reflects the non-linearity of the Bouc–Wen model.

As well as non-stationary signal above, the noises are added to the clear signal calculated by the Bouc–Wen model with the SNRs of 10 dB, 15 dB, and 20 dB, which will be used

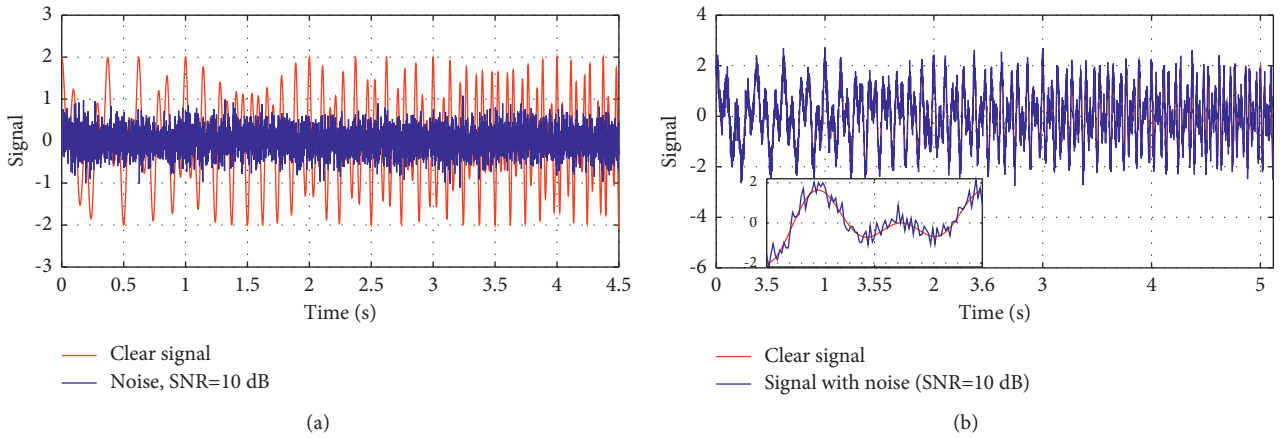

Figure 2: Non-stationary signal: (a) comparison of clear signal and noise; (b) comparison of contaminated and clear signal.

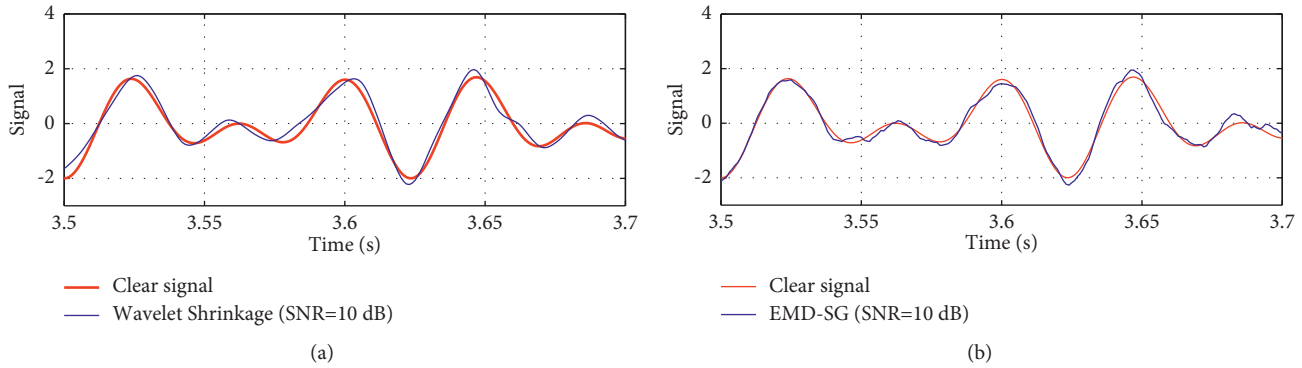

Figure 3: Noise elimination of non-stationary signal using traditional methods: (a) Wavelet shrinkage method; (b) EMD-SG method.

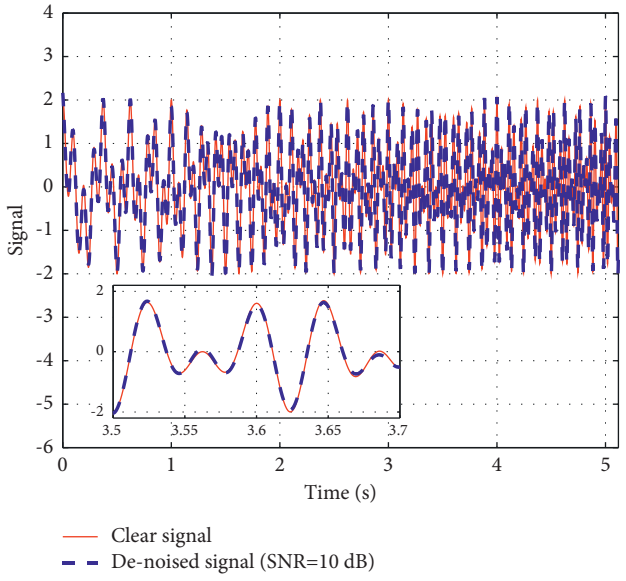

Figure 4: Noise elimination of non-stationary signal using proposed method when SNR = 10 dB.

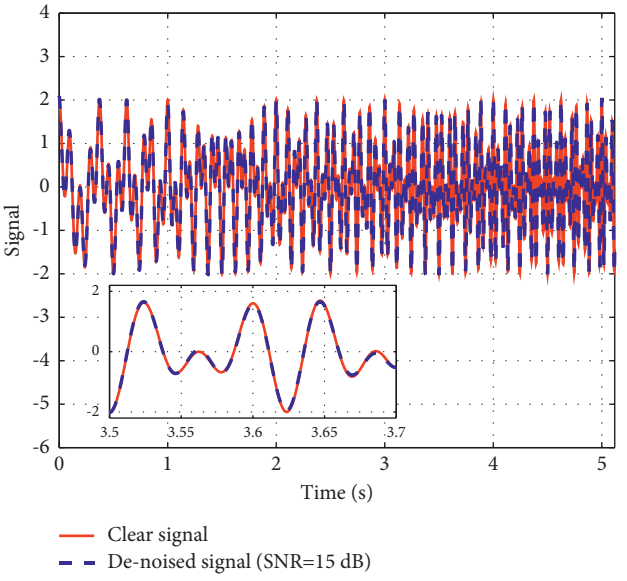

Figure 5: Noise elimination of non-stationary signal using proposed method when SNR = 15 dB.

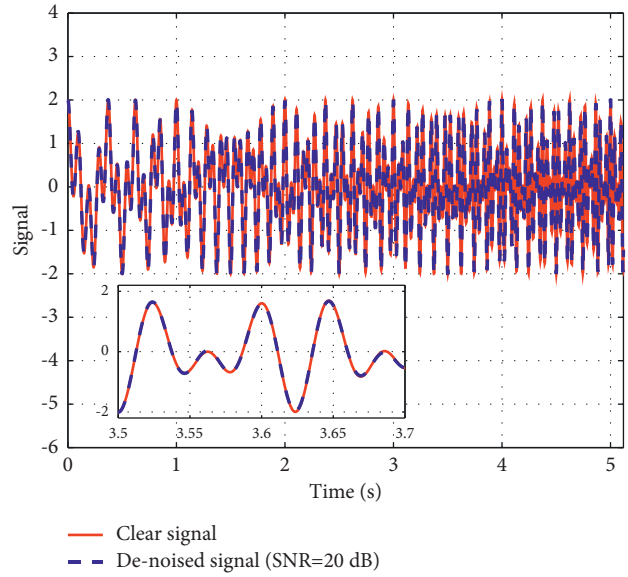

Figure 6: Noise elimination of non-stationary signal using proposed method when SNR = 20 dB.

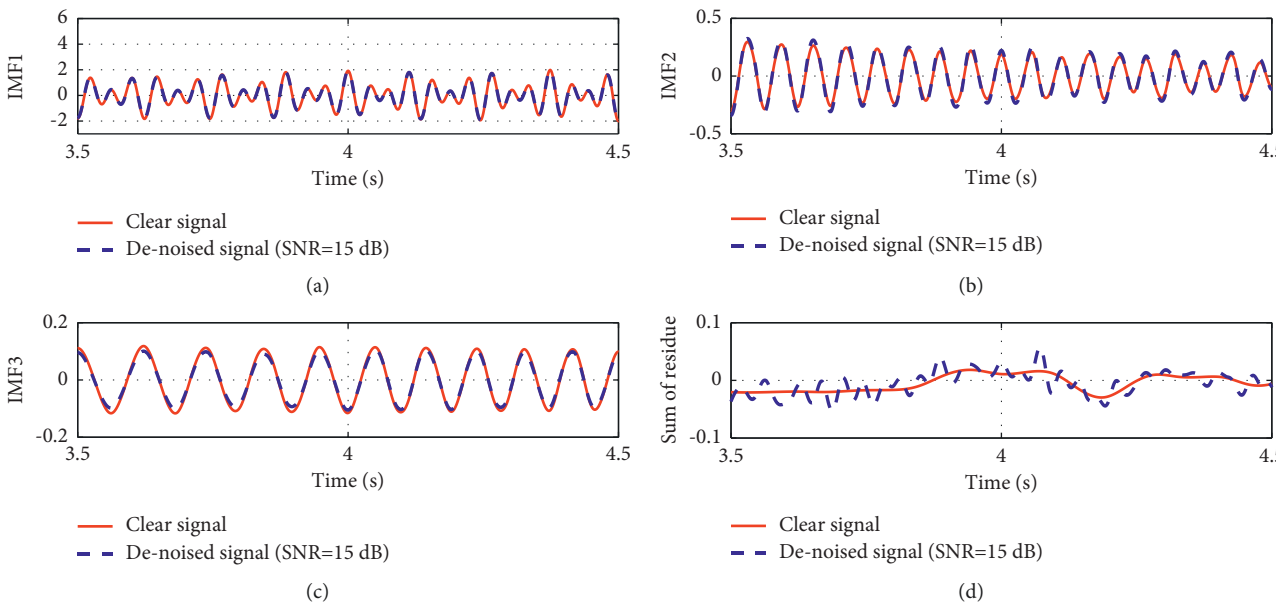

Figure 7: IMFs comparison between clear signal and de-noised signal using proposed method.

Table 1: De-noised results in SNR and RMSE of non-stationary signal corrupted by different noise levels.

Noise level	10 dB		15 dB		20 dB	
Criteria	SNR (dB)	RMSE	SNR (dB)	RMSE	SNR (dB)	RMSE
Wavelet shrinkage method	15.587	0.1663	20.970	0.0895	26.604	0.0468
EMD-SG method	18.055	0.1251	23.055	0.0704	28.056	0.0396
Proposed method	24.724	0.0581	29.428	0.0338	34.688	0.0184

to investigate the noise elimination efficiency using proposed method to non-linear signal. Acceleration response of the system corrupted by the noise with an SNR of 10 dB is shown in Figure 9, where the adverse effect is obvious compared with clear signal. Wavelet shrinkage and EMD-SG methods are used to reduce the noises, and the de-noised results of acceleration corrupted by 10% of the noise (SNR = 10 dB) applying the two methods are exhibited in

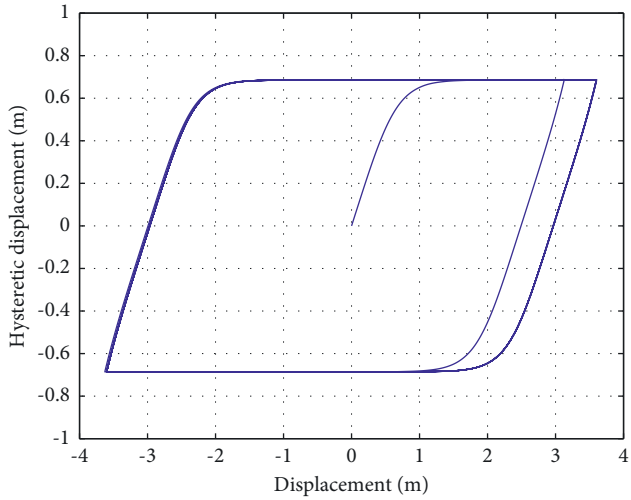

Figure 8: Hysteresis loop of the non-linear system.

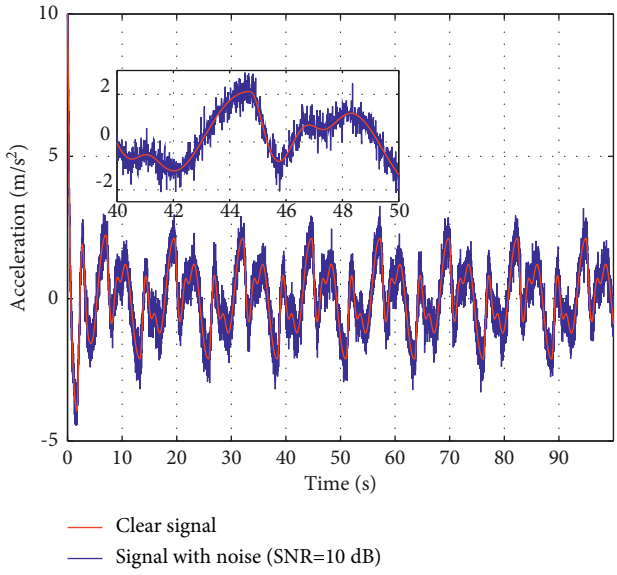

Figure 9: Comparison of clear and contaminated acceleration signals of hysteretic system.

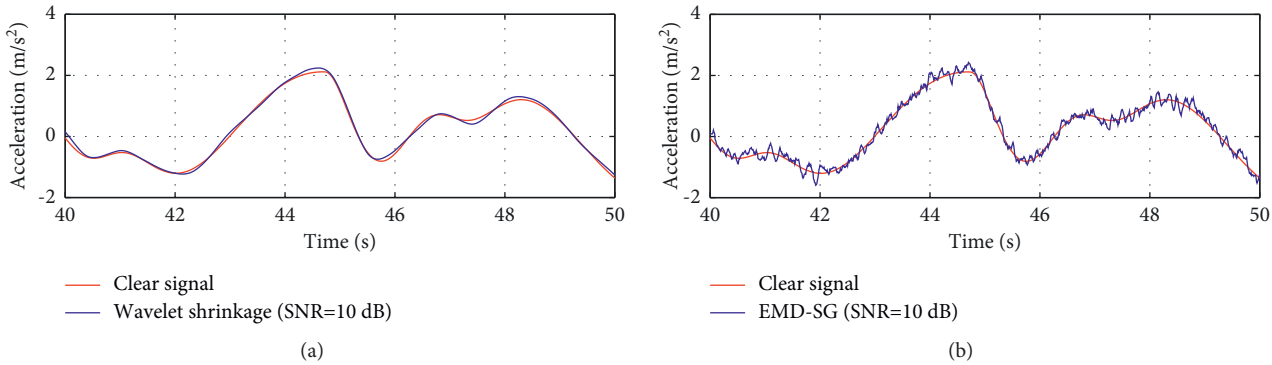

Figure 10: Noise elimination of non-linear signal using traditional methods: (a) wavelet shrinkage method; (b) EMD-SG method.

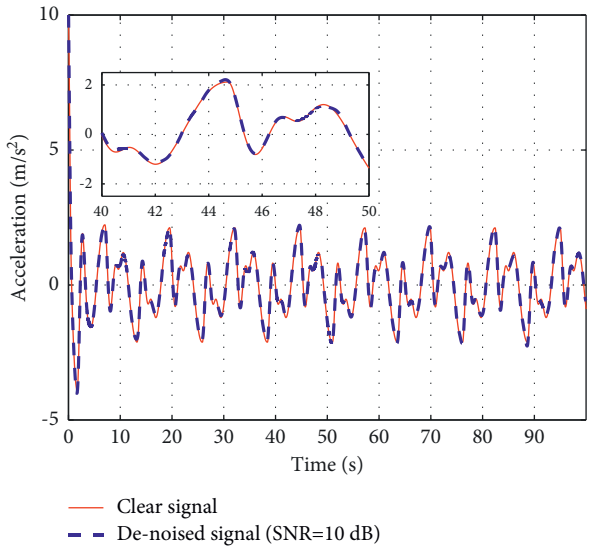

Figure 11: Noise elimination of non-linear signal using proposed method when SNR = 10 dB.

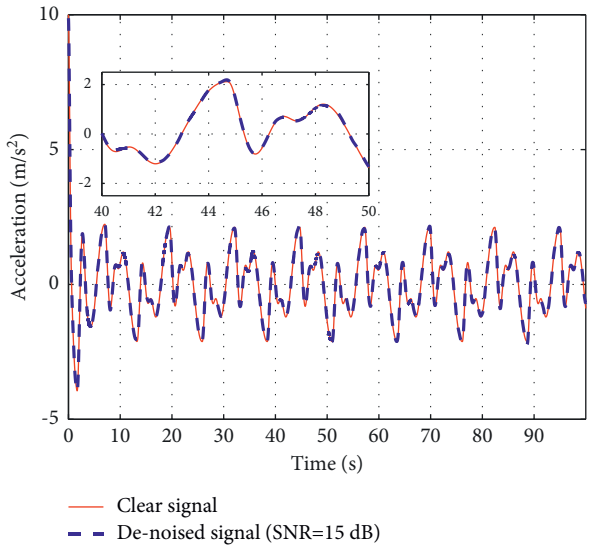

Figure 12: Noise elimination of non-linear signal using proposed method when SNR = 15 dB.

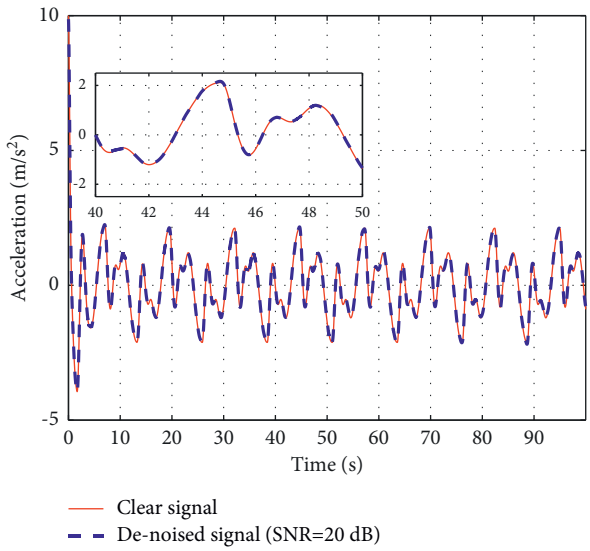

Figure 13: Noise elimination of non-linear signal using proposed method when SNR = 50 dB.

Table 2: De-noised results in SNR and RMSE of non-linear signal corrupted by different noise levels.

Noise level	10 dB		15 dB		20 dB	
Criteria	SNR (dB)	RMSE	SNR (dB)	RMSE	SNR (dB)	RMSE
Wavelet shrinkage method	21.631	0.1016	26.364	0.0589	30.368	0.0372
EMD-SG method	17.832	0.1574	22.832	0.0885	27.832	0.0498
Proposed method	24.752	0.0709	29.272	0.0422	33.667	0.0254

Figure 10, which shows that the discrepancies are more obvious compared with non-stationary example.

For the non-linear signal, applying the proposed method to the signal corrupted by the noises with SNRs of 10 dB, 15 dB, and 20 dB, the comparisons of de-noised and clear signals are plotted in Figures 11–13, which show that the de-noised signals are all consistent with the clear signal.

The quantitative analysis is also carried out in the example, and the results are listed in Table 2. Based on the analysis, one can learn that the proposed method is superior to the other two methods when dealing with the non-linear signal corrupted by the noises with SNRs of 10 dB, 15 dB, and 20 dB. At the same time, the SNRs are raised 14.752 dB, 14.272 dB, and 13.667 dB when using the proposed method to eliminate the above corresponding noises, and the RMSEs are reduced 30.22%, 28.35%, and 31.72% compared with the better traditional method (wavelet shrinkage).

5. Conclusion

In this paper, a moving-average method based on complex exponential decomposition is proposed aiming at non-stationary and/or non-linear signal de-noising. The method applies a moving window separating the signal into the small segments and dealing with the segments as stable signals. The time-domain method avoids the shortage of linear methods, and overcomes the limitation of Fourier transform when using Fourier filters. To investigate the performance of the proposed method, numerical study is implemented. The white Gaussian noise is added to clear signal to simulate the noise during signal collection. Two signals, a non-stationary and a non-linear signal, are researched in this paper, which are added noises with SNRs of 10 dB, 15 dB, and 20 dB. Wavelet shrinkage and EMD-SG methods are used to eliminate the noise contained in signal, which shows that the EMD-SG method has better de-noising effect when dealing with non-stationary signal, while the wavelet shrinkage method is better than EMD-SG method when dealing with non-linear signal. Compared with the two methods, the proposed method obtains better results no matter for disposing non-stationary or non-linear signal. The proposed method improves the SNRs by 14.724 dB, 14.428 dB, and 14.688 dB, and reduces RMSEs by 53.56%, 51.99%, and 53.54% compared with EMD-SG method when the non-stationary signal is corrupted by 2%, 5%, and 10% noise. While dealing with the non-linear signal corrupted by 2%, 5%, and 10% noise applying the proposed method, the SNRs are raised 14.752 dB, 14.272 dB, and 13.667 dB, and the RMSEs are reduced 30.22%, 28.35%, and 31.72% compared with wavelet shrinkage method.

Data Availability

The data used to support the findings of this study are available from the corresponding author upon request.

Conflicts of Interest

The authors declare that they have no conflicts of interest.

Acknowledgments

The authors wish to acknowledge the financial support of the National Natural Science Foundation of Zhejiang Province (No. LQ21E090010), the National Natural Science Foundation of China (No. 52001126), the Open Fund of Key Laboratory of Far-shore Wind Power Technology of Zhejiang Province (No. ZOE2021003), the Guangdong Basic and Applied Basic Research Foundation (No. 2022A1515010453), and the State Key Laboratory of Coastal and Offshore Engineering at Dalian University of Technology (No. LP2102).

References

[1] O. E. Esu, Y. Wang, and M. K. Chryssanthopoulos, "Local vibration mode pairs for damage identification in axisymmetric tubular structures," *Journal of Sound and Vibration*, vol. 494, Article ID 115845, 2021.

[2] S. Wu, W. Xing, Y. Liu, and Y. Shao, "Research on dynamic characteristics and identification method of local defect on the roll surface," *Engineering Failure Analysis*, vol. 121, Article ID 105063, 2021.

[3] R. Hou and Y. Xia, "Review on the new development of vibration-based damage identification for civil engineering structures: 2010-2019," *Journal of Sound and Vibration*, vol. 491, Article ID 115741, 2021.

[4] H. Chen, N. Hu, Z. Cheng, L. Zhang, and Y. Zhang, "A deep convolutional neural network based fusion method of two-direction vibration signal data for health state identification of planetary gearboxes," *Measurement*, vol. 146, pp. 268–278, 2019.

[5] X. Dong, J. Lian, H. Wang, T. Yu, and Y. Zhao, "Structural vibration monitoring and operational modal analysis of offshore wind turbine structure," *Ocean Engineering*, vol. 150, pp. 280–297, 2018.

[6] Z. Wu and N. E. Huang, "A study of the characteristics of white noise using the empirical mode decomposition method," *Proceedings of the Royal Society of London. Series A: Mathematical, Physical and Engineering Sciences*, vol. 460, no. 2046, pp. 1597–1611, 2004.

[7] V. Ondra, I. A. Sever, and C. W. Schwingshackl, "Identification of complex non-linear modes of mechanical systems using the Hilbert-Huang transform from free decay

responses," *Journal of Sound and Vibration*, vol. 495, Article ID 115912, 2021.

[8] Y. D. Zhang, X. L. Yang, F. L. Zhu et al., "Characteristics of non–linear dynamics and energy transfer in a vibration gas–solid fluidized bed by using Hilbert–Huang transform," *Powder Technology*, vol. 344, pp. 970–980, 2019.

[9] T.-L. Huang, M.-L. Lou, H.-P. Chen, and N.-B. Wang, "An orthogonal Hilbert-Huang transform and its application in the spectral representation of earthquake accelerograms," *Soil Dynamics and Earthquake Engineering*, vol. 104, pp. 378–389, 2018.

[10] N. E. Huang, Z. Shen, and S. R. Long, "A new view of nonlinear water waves: the Hilbert spectrum," *Annual Review of Fluid Mechanics*, vol. 31, no. 1, pp. 417–457, 1999.

[11] A. González and H. Aied, "Characterization of non-linear bearings using the Hilbert-Huang transform," *Advances in Mechanical Engineering*, vol. 7, no. 4, Article ID 168781401558212, 2015.

[12] A. O. Boudraa, J. C. Cexus, and Z. Saidi, "EMD-based signal noise reduction," *World Acad Sci Eng Tec*, vol. 1, no. 2, pp. 589–592, 2007.

[13] A. V. Oppenheim, W. S. Ronald, and J. R. Buck, *Discrete-Time Signal Processing*, Prentice-Hall, Upper Saddle River, NJ, USA, 1999.

[14] J. G. Proakis and D. G. Manolakis, *Digital Signal Processing: Principles, Algorithms, and Applications*, Prentice-Hall, Saddle River, NJ, USA, 3rd edition, 1996.

[15] D. L. Donoho and I. M. Johnstone, "Ideal spatial adaptation by wavelet shrinkage," *Biometrika*, vol. 81, no. 3, pp. 425–455, 1994.

[16] D. L. Donoho, "De-noising by soft-thresholding," *IEEE Transactions on Information Theory*, vol. 41, no. 3, pp. 613–627, 1995.

[17] N. E. Huang, Z. Shen, S. R. Long et al., "The empirical mode decomposition and the Hilbert spectrum for nonlinear and non-stationary time series analysis," *Proceedings of the Royal Society of London. Series A: Mathematical, Physical and Engineering Sciences*, vol. 454, no. 1971, pp. 903–995, 1998.

[18] P. Flandrin, G. Rilling, and P. Goncalves, "Empirical mode decomposition as a filter bank," *IEEE Signal Processing Letters*, vol. 11, no. 2, pp. 112–114, 2004.

[19] Z. Wu and N. E. Huang, "Ensemble empirical mode decomposition: a noise-assisted data analysis method," *Advances in Adaptive Data Analysis*, vol. 01, no. 01, pp. 1–41, 2009.

[20] N. Rehman and D. P. Mandic, "Filter bank property of multivariate empirical mode decomposition," *IEEE Transactions on Signal Processing*, vol. 59, no. 5, pp. 2421–2426, 2011.

[21] Y.-x. Li and L. Wang, "A novel noise reduction technique for underwater acoustic signals based on complete ensemble empirical mode decomposition with adaptive noise, minimum mean square variance criterion and least mean square adaptive filter," *Defence Technology*, vol. 16, no. 3, pp. 543–554, 2020.

[22] H. Li, Z. Li, and W. Mo, "A time varying filter approach for empirical mode decomposition," *Signal Processing*, vol. 138, pp. 146–158, 2017.

[23] N. Iqbal, A. Zerguine, S. Kaka, and A. Al-Shuhail, "Automated SVD filtering of time-frequency distribution for enhancing the SNR of microseismic/microquake events," *Journal of Geophysics and Engineering*, vol. 13, no. 6, pp. 964–973, 2016.

[24] N. Iqbal, E. Liu, J. H. McClellan, A. Al-Shuhail, S. I. Kaka, and A. Zerguine, "Detection and denoising of microseismic events using time-frequency representation and tensor decomposition," *IEEE Access*, vol. 6, Article ID 22993, 2018.

[25] S. L. James Hu, W.-L. Yang, and H.-J. Li, "Signal decomposition and reconstruction using complex exponential models," *Mechanical Systems and Signal Processing*, vol. 40, no. 2, pp. 421–438, 2013.

[26] F. Liu, H. Li, W. Wang, W. Li, and B. Wang, "Frequency variation and sensor contribution assessment: application to an offshore platform in the South China Sea," *Journal of Sound and Vibration*, vol. 337, pp. 218–232, 2015.

[27] G. H. Golub and C. F. V. Loan, *Matrix Computations*, Johns Hopkins University Press, Baltimore, MD, USA, 3rd edition, 1996.

Hindawi
Shock and Vibration
Volume 2022, Article ID 2539870, 11 pages
https://doi.org/10.1155/2022/2539870

Research Article

Modal Investigation on a Large-Scale Containership Model for Hydroelastic Analysis

Ye Lu,[1] **Juan Liu**,[2] **Bei Teng**,[3] **Chao Tian**,[1] **Hailong Si**,[1] **Qingyun Zhou**,[1] **and Xinyun Ni**[1]

[1]*China Ship Scientific Research Center, Wuxi 214082, China*
[2]*Jiangsu University of Science and Technology, Zhenjiang 212003, China*
[3]*Wuxi Institute of Communications Technology, Wuxi 214151, China*

Correspondence should be addressed to Ye Lu; luye@cssrc.com.cn

Received 4 January 2022; Revised 3 February 2022; Accepted 29 March 2022; Published 30 April 2022

Academic Editor: Jialong Jiao

Copyright © 2022 Ye Lu et al. This is an open access article distributed under the Creative Commons Attribution License, which permits unrestricted use, distribution, and reproduction in any medium, provided the original work is properly cited.

A 20,000 TEU containership with an overall length of about 400 m is designed as a target ship to investigate ship hydroelastic characteristics in the joint industry project (JIP) of CSSRC-20,000 TEU. A set of systematic model tests are carried out in the seakeeping wave basin of CSSRC. The large-scale ship model data for hydroelastic experiments are presented with the determination of modal features. The modal test of the containership model is the premise of the hydroelastic analysis. The test of the natural frequency and modal shape of the ship model can be used to corroborate the accuracy of the finite element modelling. A three-dimensional finite element model (FEM) of the ship is employed to carry out modal analysis in a vacuum and provide modal parameters to decide the large-scale ship model data for hydroelastic experiments. Through the analysis of hydroelasticity, the wet frequency corresponding to the motion of each elastic mode is obtained. Good agreement is achieved between the numerical results and the measurement data, particularly for the lower-order modes. Only when the numerical calculations of the dry and wet modes are consistent with the experimental results, the containership model's calculated motion responses and structural loads are comparable to the experimental results. Therefore, examining the modal tests is extremely important for hydroelastic analysis. As the input data, the FEM will be shared with JIP members for further comparative studies of linear and nonlinear hydroelastic analyses. The experiments help provide reliable and accurate benchmark model test data for comparative studies using numerical software and methods.

1. Introduction

With the development of the social economy and transportation demand, containerships have gradually grown larger and faster, and some superstandard ships have increasingly been designed and built. The total length of a containership of 20,000 TEU has reached 400 meters. The bow of the containership is relatively noticeable, and the speed is generally high. The slamming phenomenon of the ship is very obvious when sailing in the waves. The longitudinal strength of the containership hull is vital. As the size of the ship increases, the vertical rigidity and torsional rigidity of the containership hull are significantly reduced. At the same time, wave-induced vibration may occur in lower sea conditions, resulting in serious hull structural fatigue problems. Strong nonlinear characteristics are often observed in the ship wave load. Determining the nonlinear wave load of containerships is of great significance to the ship's safety and structural design.

The most famous containership S175 is the first containership standard model (1978) and is still the sole standard model used for teaching and research both at home and abroad, making it the most cited model [1–4]. Kim and Kim [5] calculated the elastic vibration and whipping of a 6,500 TEU containership and a fictitious 10,000 TEU containership based on the combination of a three-dimensional (3D) Rankine source and a 3D structural model. A combination of beam elements is used to consider the slamming of the two-dimensional (2D) generalised Wagner model Load. Senjanović et al. [6] proposed that hydroelastic analysis is the most suitable method for the rational design of containerships, and free vibration analysis is one of the most important

steps. It can be done using a one-dimensional (1D) or 3D finite element model (FEM) of ship structures. The beam model is usually used in the preliminary design stage, and the completed 3D FEM is more suitable for the final strength examination. Malenica and Derbanne [7] claimed that as the length of the ship increases, the hydroelastic structure response of ultralarge containerships is more important. The large size, nearly 400 meters between the vertical lines, results in a lower natural frequency of the structure. They also claimed that the correct modelling of the hydroelastic ship structure response and its inclusion in the overall design program is much more complicated than the assessment of the static structure response. Hirdaris et al. [8] reviewed several different fluid-structure coupling methods for the ship motions and loads. The weak nonlinear wave load is applied to the 10,000 TEU containership. The load is not only reasonable for at amidships, but also applicable at fore and aft. The prediction of wave excitation force of radiation potential and diffraction potential is more accurate when the instantaneous wet surface is considered. Ye et al. [9] used the 3D potential flow theory and the thin-walled beam theory to calculate the hydroelasticity problem of a large opening containership. The high-order isoparametric boundary element method is adopted to solve the boundary integral equation of the hydrodynamic boundary value problem, and the structure is simplified to consider the warpage. The FEM of thin-walled beams is investigated with the effects of shear and section rotation, as well as the large opening of the cargo hold and the torsion box. The numerical results are compared with the test data and both good calculation accuracy and calculation efficiency are obtained. Based on the ABS classification society regulations of the whipping and wave-induced vibration response, Lin et al. [10] took a 16,000 TEU ultra-large containership as an example and interpreted the specifications of various classification societies regarding the hydroelastic effect. The research found that the hydroelastic effect of ultralarge containerships cannot be ignored, and it has different effects on the longitudinal bending and fatigue damage of the ship. The whipping has increased the amidships' bending moment and shear force by 20%~25%. Wave-induced vibration also affects the ship. The cumulative fatigue damage increases by nearly 20%. Chen [11] studied the two effects of the insurmountable wave-induced vibration and whipping phenomenon on the hull strength caused by the longitudinal strength and fatigue strength in the design of superlarge ships. He tried to propose a method for the previously mentioned two kinds of ship mechanics in the initial stage of ship design. Regarding the method of forecasting frontier problems to solve the designer's difficulties, he pointed out the influence of various uncertain factors on the calculation. He pointed out that in the design of modern ultralarge civil ships, it is extremely important to strengthen model tests and full-scale ship experiments when the current theory cannot fully explain the coupling of wave-induced vibration and whipping and accurately separate their respective effects. It is the only way to ensure the safety of ships. Han et al. [12] introduced that the 18,000 TEU ultralarge containership has a high speed and significant bow, and the first-order natural frequency is lower than conventional ship types, which is likely to cause springing and whipping. The hydroelastic analysis is applied to discuss the impact of whipping and springing on the ultimate strength and fatigue strength of the ultralarge containership structure. Taking the 18,000 TEU ultralarge containership as the research object, Zhang et al. [13] considered the effects of symmetric and antisymmetric modes and used the FE method for dry modal analysis. Based on the 3D linear hydroelasticity theory in the frequency domain and spectral analysis method, the hot spot stress responses are solved. Combined with the linear cumulative damage method, the fatigue life and the influence of wave-induced vibration on the fatigue of hatch corners are obtained. It is found that wave-induced vibration will cause a high-frequency response of loads and stresses. The fatigue cumulative damage of the hatch corners has increased significantly, and the fatigue life has been reduced by up to 50%.

In addition to the previously mentioned scholars' detailed analysis and research on the hydroelasticity of containerships, many authors reviewed the research in recent years [14–16]. They carried out a detailed analysis of the external loads such as wave-induced springing on the hydroelasticity of the ship, especially the containership, and also gave the motion response and structural load evaluation caused by slamming.

From 2005 to 2009, the KCS initiated by MOERI (Maritime & Ocean Research Institute) compared the test results of tankers, containerships, and surface ships to standardize the capabilities of different ship manipulation simulation methods (based on CFD methods) test.

The international joint industrial project WILS (Wave Induced Loads on Ships) I (2006~2008), II (2008~2011), and III (2012~2014) were initiated and led by MOERI. Taking 6750 TEU and 10,000 TEU containerships, a series of studies were performed, including wave loads, modal tests, hydroelastic response, linearity and nonlinearity, full-scale ship tests, and so on.

From 2009 to 2012, Bureau Veritas (BV) initiated the TULCS (Tools for Ultra Larger Container Ship) international joint industrial project to conduct numerical calculations and experimental comparative studies on wave-induced vibration and slamming-induced whipping for 14,000 TEU containerships.

To investigate the influence of springing and whipping on the bending and torsion moments of the ship structures, a Joint Industry Project (JIP) named Comparative Study on Springing Responses of Containership 20,000 TEU (CSSRC-20,000 TEU) was initiated by Prof. Yousheng Wu from China Ship Scientific Research Center (CSSRC), which will last for about four years from 2018 to 2022. Other initiators or members of this JIP include China Classification Society (CCS), Lloyd's Register of Shipping (LR), Bureau Veritas (BV), American Bureau of Shipping (ABS), Class NK (NK), Korean Register of Shipping (KR), Indian Register of Shipping (IRS), Shanghai Waigaoqiao Shipbuilding Co. Ltd (SWS), Shanghai Merchant Ship Design & Research Institute (SDARI), University of Southampton (UoS), Chalmers University of Technology (CUT), Shanghai Jiaotong University (SJTU), Harbin Engineering University (HEU), Dalian University of Technology (DUT), Huazhong

University of Science and Technology (HUST), Wuhan University of Technology (WUT), and Jiangsu University of Technology (JUST). The initiators and members of CSSRC-20,000 TEU JIP are shown in Figure 1. The introduction to this JIP can be found on the website: jip.cssrc.com.

The objectives of this JIP contain four aspects are shown as follows:

(1) to make a global review by synthetic analysis of existing methods/software for hydroelastic analysis,

(2) to provide reliable and accurate benchmark model tests data, which can be considered as a standard database for verification and validation,

(3) to perform a comparative study of the most recent numerical methods/software by comparing with measurements of large-scaled hydroelastic model tests,

(4) to provide critical information for establishing standard procedures/guidelines for the numerical prediction of the hydroelastic response including springing and whipping.

Aiming at the main objectives of this JIP, reliable and accurate large-scale benchmark model test data [17] for comparative studies using the most recent numerical methods and software will be provided. A 20,000 TEU containership with an overall length of about 400 m has been designed as the target ship for the JIP studies, and systematic model tests have been carried out in the seakeeping wave basin of CSSRC.

In this JIP, the 3D hydroelastic method will be applied in ultralarge containerships, including linear and nonlinear methods. Based on the results of the benchmark of model test and numerical comparison, the methods adopted by the participants of this JIP will be analysed in detail. Then, the proper methods and the criterion will be advised to obtain more reasonable and accurate results.

In this paper, the modal characteristic of containership is investigated for hydroelastic analysis. As well known, based on the modal superposition, the hydroelasticity could solve the fluid-structure interaction problem easily. So, the ship modal information is demonstrated in detail including construction and the modal test. The mass distribution and stiffness distribution of the containership model settle the natural frequency of vibration in a vacuum. The manufacturing accuracy and installation method of the model can affect the frequency. During modal testing, the location of the hoisting rope and lifting point is critical, which can change the natural frequencies and modal shapes. 3D finite element numerical modelling is also very important in the connection of the ship model. A slight change in mechanical parameters such as material and elastic modulus will greatly change the natural frequency.

2. 3D Hydroelastic Method

In 1984, Yousheng Wu pioneered combining the 3D potential flow theory with the 3D structural dynamics theory to establish the 3D hydroelasticity theory. Assuming that the ship moves and deforms slightly in waves, according to the principle of modal superposition, the motion and deformation of the hull structure relative to its equilibrium position can be expressed as

Figure 1: Initiators and members of CSSRC-20,000 TEU JIP.

$$\vec{u} = \sum_{r=1}^{m} \vec{u}_r p_r = \sum_{r=1}^{m} (u_r, v_r, w_r) p_r, \quad (1)$$

where $p_r\,(r = 1, 2, \ldots, m)$ represents the r th principal coordinate component of the displacement $\vec{u}_r$ relative to the dry hull mode.

We assumed that the fluid around the floating body is an ideal fluid that is uniform and incompressible and nonviscous, the flow field had no rotation, and the free surface wave is a small amplitude wave. Combining structural dynamics, a generalised 3D linear frequency domain hydroelastic equation of motion for a floating body (1) could be obtained as follows:

$$[a + A]\{\ddot{p}\} + [b + B]\{\dot{p}\} + [c + C]\{p\} = \{Z\} + \{\Delta\} + \{Q\}. \quad (2)$$

In the formula, $[a]$, $[b]$, and $[c]$ are the generalised mass matrix, the generalised damping matrix, and the generalised stiffness matrix of the structure, respectively. Corresponding to the previously mentioned matrix, generalised fluid additional mass matrix, generalised fluid additional damping matrix, and generalised fluid restoring force matrix are $[A]$, $[B]$, and $[C]$. Moreover, $\{Z\}$, $\{\Delta\}$, and$\{Q\}$ are generalised surface force, generalised concentrated force, and generalised volume force arrays, respectively; $\{p\}$ is generalised principal coordinate arrays.

3. Ship Model

3.1. Scale and Main Particulars. The experimental model of the containership is made of steel with a two-cylinder backbone. It is divided into 14 segments connected by the flexible backbone (Figure 2). The ship model is segmented at St 2, St 4, St 5 + 50 mm, St 6, St 7, St 8.5, St 10 + 70 mm, St 11, St 12, St 13 + 50 mm, St 14, St 16, and St 18. The gaps between adjacent segments are designed as 20 mm to prevent the possible contact of the two segments during the test. To avoid flooding, the thin rubber strips are fitted to seal the gaps with some spare room to eliminate the possible load transfer.

Figure 2: The containership model with 14 segments.

Considering the capabilities of wave generation of the wave basin, a scaling ratio of $1:49$ ($\mu = 49$) is chosen, which makes the ship model have available travelling speed, space, and weight margins for fitting in the necessary instrumentation and adjusting the weight distribution. Figure 3 shows the hull offset lines. Table 1 gives the main particulars with two loading conditions of the ship model.

3.2. Mass Distribution of the Ship Model. Table 2 gives the estimation of the mass of each segment of the ship model, which is calculated from the ship mass statistics. The weight distribution of the ship model is also shown in Figure 4. The blue bars demonstrate the mass in the full load condition, and the red bars present the mass in the design draft condition.

3.3. Stiffness Similitude Using Backbone. The similarity of section stiffness is an important step in scaling the full-scale ship to the model. Once the stiffness satisfies a similar criterion, the natural frequency will meet a similar relationship, and its modal shape will be consistent with the full-scale ship. According to the similitude principle, a blue backbone (Figure 5) is designed to simulate the bending of the containership in waves. To satisfy the stiffness similitude of the ship on vertical bending, a kind of steel is chosen to construct the backbone. Young's modulus of steel is 206 Gpa. The Poisson ratio is 0.3. However, the stiffness along the ship length is not uniform. Generally, the inertia moment of the vertical bending at amidships is larger than the values at fore and aft. Therefore, the flexible backbone has been designed to the six variable cross-sections joined end to end. Table 2 gives the design properties of the backbone such as the inertia moment of vertical bending from stern to station 19.

3.4. Construction and Installation of the Backbone. Figure 6 gives the schematic drawing of the installation of the backbone built-in ship model, which is carefully designed. All the hydrodynamic loads transfer to the backbone, which act on the segments. However, the stiffness of the segment did not affect the flexibility of the backbone noticeably. It can be seen that the backbone beam is connected to the ship hull through the transverse supports, which are green, shown in Figure 5.

4. Determination of Modal Property

4.1. Measurement Methods and Instrumentation. It is essential to obtain the modal parameters, including natural frequencies, modal shapes, and damping ratio of the ship model since they are the indispensable input data for hydroelastic analyses. Therefore, both the dry and wet modes, including the vertical bending of the ship model, are measured and analysed in the vibration lab of CSSRC. Before carrying out the modal test, the centre of gravity and inertia of the ship model shall be adjusted to account for full load and design draft loading conditions, respectively.

The modal parameters are determined by a hammering test, hitting the ship model with a soft hammer and recording the vertical vibrations and their decay curves. The roving hammer setup used a PCB-086C04 instrumented hammer for the excitation measurement. The PCB 352C33 accelerometers are employed to measure the dynamic responses of the backbone of the ship model. Figure 7 gives the installation layout of accelerometers, including 30 points for vertical acceleration measurement. The measurement data are obtained and processed by using B&K 3660D, a dynamic data acquisition and processing system. The relevant frequency response function and modal parameters could be derived in the measurement.

To measure the vertical modal shapes, the ship model is suspended in the air by elastic ropes. Figure 8 shows the different suspending patterns on the ropes to measure the vertical modal shapes. In the vertical bending modal measurement, the ropes are going around the side of the hull of the model.

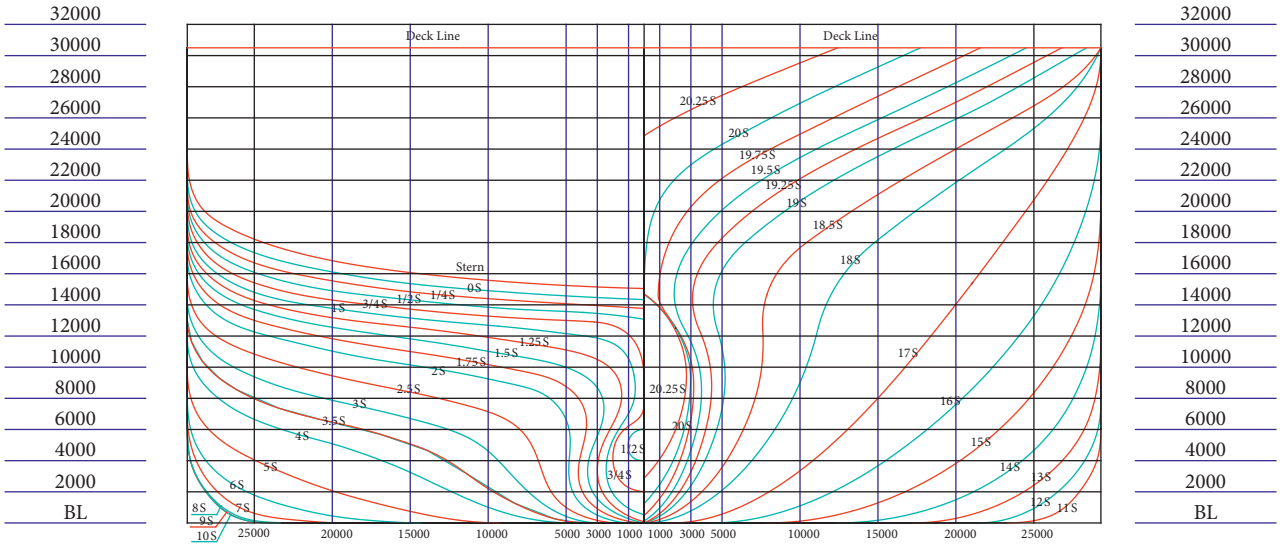

Figure 3: Offset lines of the containership.

Table 1: Main particulars.

Item	Symbol	Ship		Model	
		Full load	Design draft	Full load	Design draft
Scale ration	μ	1	1	49	49
Density of water	ρ (t/m^3)	1.025	1.025	1.000	1.000
Length overall	L_{OA} (m)	399.67	399.67	8.157	8.157
Length between perpendiculars	L_{BP} (m)	383	383	7.816	7.816
Beam	B (m)	58.6	58.6	1.196	1.196
Depth	D (m)	30.5	30.5	0.622	0.622
Draft forward	T_f (m)	15.2	13.37	0.31	0.273
Draft aft	T_a (m)	16.7	15.3	0.341	0.312
Displacement	Δ (t)	260602.9	228482.8	2.161	1.895
Height of CG above baseline	Z_g (m)	27.574	26.106	0.563	0.533
LCG from AP	X_g (m)	182.714	183.485	3.729	3.745
Moment of inertia about y-axis	I_{yy} (kg $\cdot$ m^2)	2.307×10^{12}	1.913×10^{12}	7967.86	6605.7

Table 2: Design properties of the backbone along the ship length.

No.	Length (m)	Outer diameter (m)	Thickness (m)	Inertia moment of vertical bending for one cylinder (m^4)	Inertia moment of vertical bending for two cylinders (m^4)
MI-1	1.1724	0.089	0.005	1.1679$E-06$	2.3358$E-06$
MI-2	0.7816	0.102	0.0055	1.9472$E-06$	3.8944$E-06$
MI-3	3.1264	0.114	0.005	2.5481$E-06$	5.0963$E-06$
MI-4	0.7816	0.102	0.006	2.0928$E-06$	4.1855$E-06$
MI-5	0.7816	0.095	0.005	1.4358$E-06$	2.8716$E-06$
MI-6	0.7816	0.083	0.005	9.3561$E-07$	1.8712$E-06$

It should be noted that the natural frequencies of the mass-spring system in rigid body motion should be well below the elastic deformation resonance modes of the ship model. In addition, the elastic rope shall be hung at the location of vibration modal nodes to minimize the influence of support on the modal results. Before the modal measurement, two kinds of spring rigidity have been employed for comparison, 25537 N/m and 17448 N/m. It is found that the impact of rope rigidity is negligible on the measured results of natural frequency if the model is suspended at modal nodes.

During the vertical modal measurement in the air, the suspension locations are adjusted iteratively until they

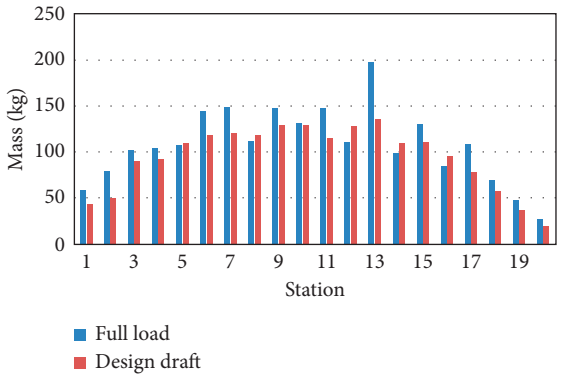

Figure 4: Weight distribution of the ship model.

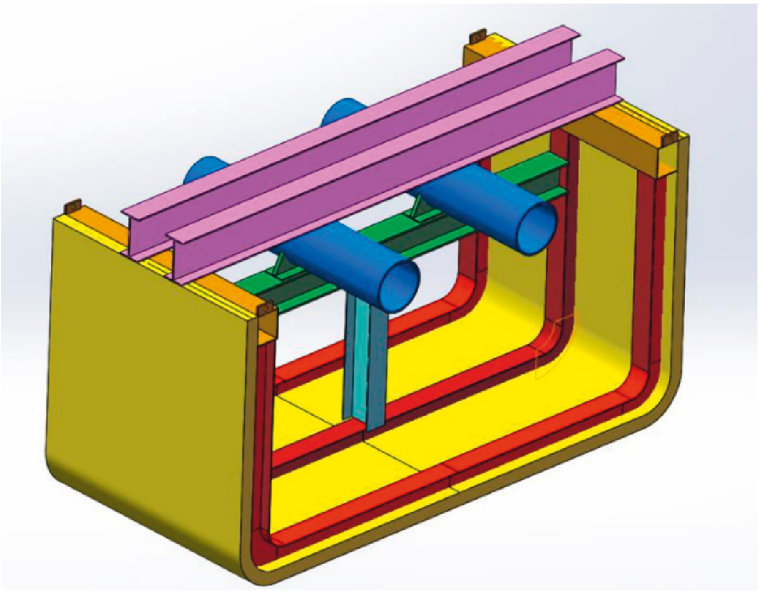

Figure 5: Backbone of the model in blue.

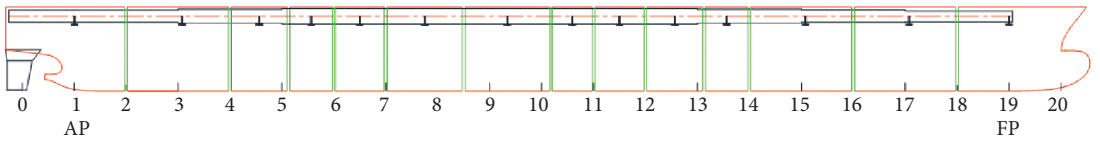

Figure 6: Schematic drawing of the installation of backbone in ship model.

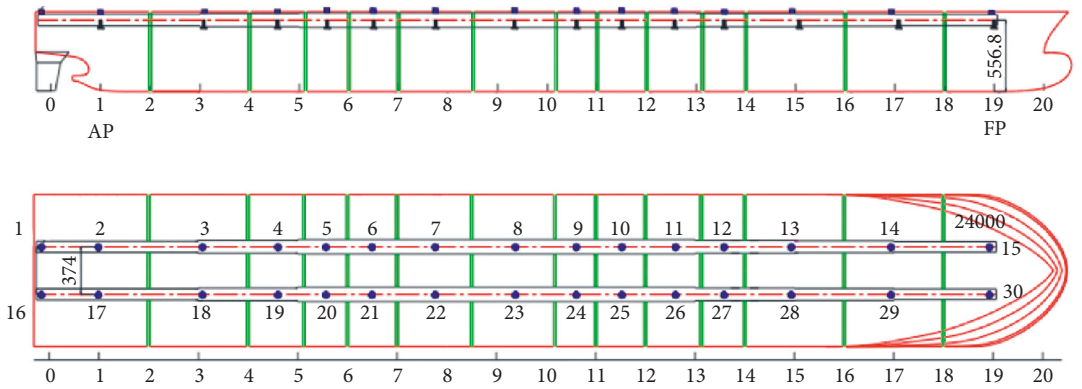

Figure 7: Layout of the accelerometers for modal shape measurement.

Figure 8: Different suspending patterns in the measurement of the modal shapes.

correlated well with the vibration modal nodes derived from the previous measurement analysis.

4.2. Modal Results. The natural frequencies, damping ratio, and modal shape of the model have been analysed from the measurement results. To obtain the resonance frequencies, we plotted the RAOs of accelerations at each measurement point. The RAOs are defined as the ratio of the response amplitude to the amplitude of exciting force. The peaks in these curves indicated the modal resonances of the model.

Figure 9 shows the dry and wet vertical acceleration RAOs at different measured locations under vertical bending (VB) excitation of the ship model for both the full load condition and design draught condition.

Figures 9(a) and 9(b) show the natural frequencies of full load and design draft loading conditions in air respectively. Figures 9(c) and 9(d) show the resonant frequencies of full load and design draft loading conditions in the water.

In Figure 9, we can see that the natural frequencies of the ship model can be investigated clearly. Although the acceleration signals are thirty, the two-node VB and three-node peaks nearly occur at the same frequencies, respectively. It is worth pointing out that there are small peaks before the frequency according to the two-node VB. This is the natural frequency due to the elastic cord in the suspension system. Therefore, the rigidity of the hanging rope selected should avoid the natural frequencies of the ship model. In contrast, the resonant frequency test results in the water show that the peaks are not as sharp as the natural frequency peaks in the air, showing a wider distribution of peaks. The two-node VB and three-node VB peaks are discernible.

Table 3 gives the natural frequencies and damping ratio of the vertical bending mode of the ship from measurement analyses.

From Table 3 we can find that the wet frequencies are lower than the dry frequencies in the same modal shape. It is because of the effect of the added mass in the water. The greater the masses, the lower the frequencies. Similarly, the 2-node frequency in full load is lower than that in design draft loading, the same as the 3-node frequency. In addition, the damping coefficient corresponding to each order frequency is obtained according to the half-power method. As well known, the damping coefficient plays a key role in the peak value of the subsequent hydroelastic wet mode.

In addition, natural frequencies are the inherent properties of ship models in air and water. The uncertainty of the modal test mainly comes from the accuracy of the measuring instrument, the detail of the ship model, and the change in environmental factors. Since a total of 30 acceleration sensors are arranged on the measured backbone, through three repeatability tests, these data are analysed to obtain the standard deviation and measurement uncertainty.

5. Dry Mode and Wet Frequency Prediction

5.1. FEM for Dry Modal Calculation

5.1.1. General Introduction. Due to the lack of the inertia moment of each section, the simplified beam model is not as accurate as a 3D FEM for simulating the moment of inertia of a ship. The 3D numerical model for simulation is modelled by FE analysis software MSC.Patran. Due to the accuracy of the modal calculation, the two backbones are modelled by solid elements. To obtain the inertia moment, the mass and the instruments box are created by solid elements. The girders, ribs, and supports are built in steel by plate elements with different thicknesses. The ship hull is also constructed of plate elements, which are made of fibreglass. The FEM of the containership of full load condition is seen in Figure 10. Some groups of mass cubic are located on the side of the ship model. The whole FEM has 495387 nodes and 315117 elements in the

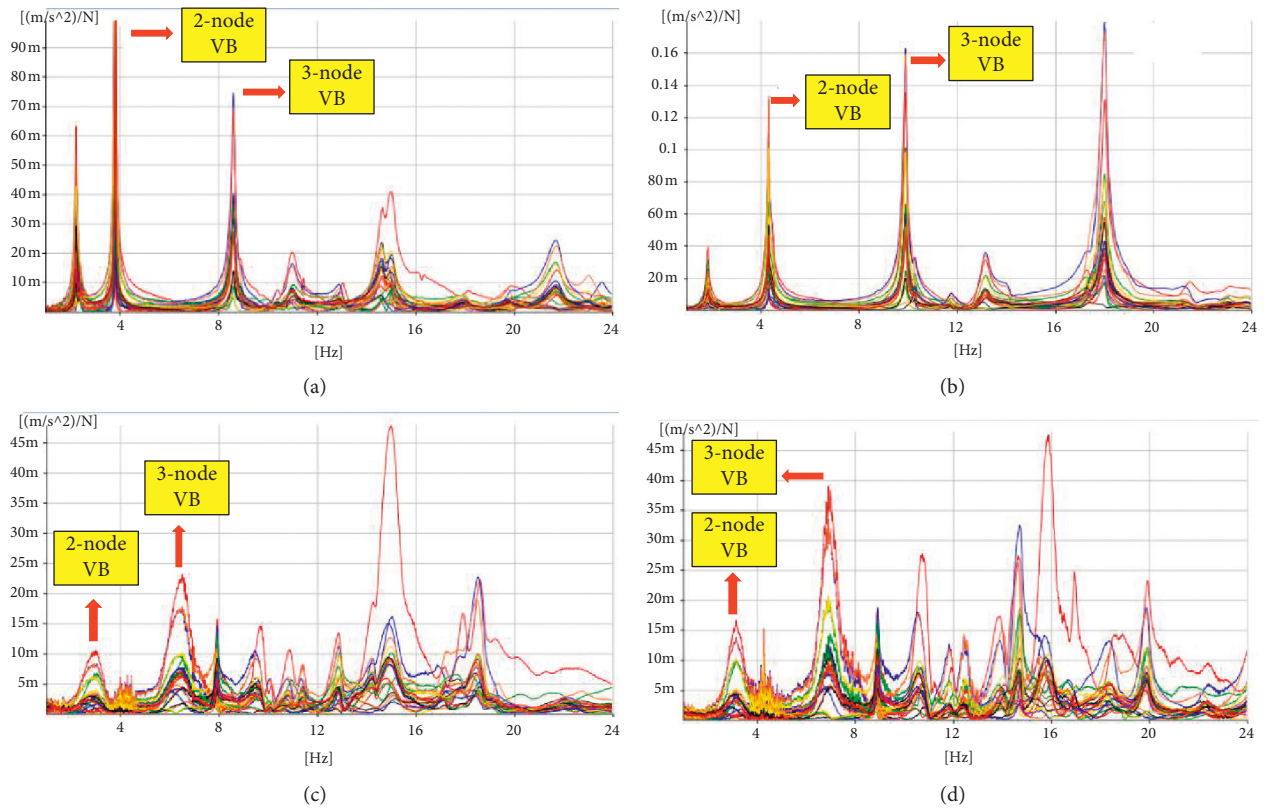

Figure 9: Vertical acceleration RAOs for vertical bending (VB) excitation. (a) Full load condition in air. (b) Design draft loading condition in air. (c) Full load condition in water. (d) Design draft loading condition in water.

Table 3: Vertical bending modal results from measurement.

Loading condition	Modal shape	Dry mode		Wet mode	
		Natural frequency (Hz)	Damping ratio (%)	Natural frequency (Hz)	Damping ratio (%)
Full load	2-Node	3.823	0.23	2.825	6.3
	3-Node	8.575	0.8	6.455	4.0
Design draft	2-Node	4.337	0.93	3.104	5.6
	3-Node	9.923	0.48	6.955	2.5

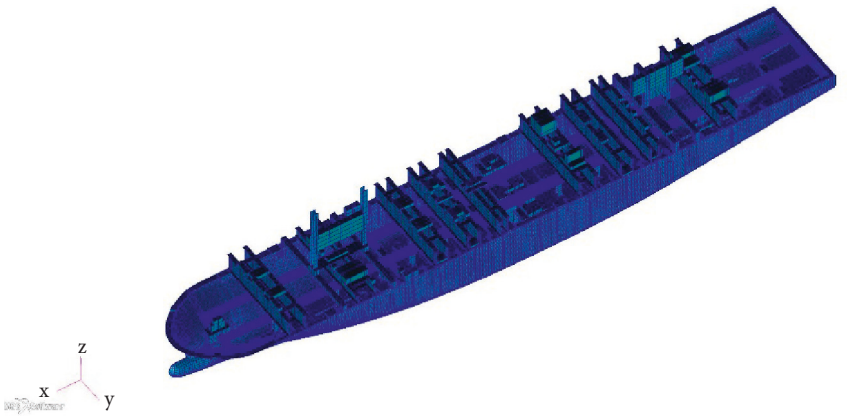

Figure 10: FEM of the containership of full load condition.

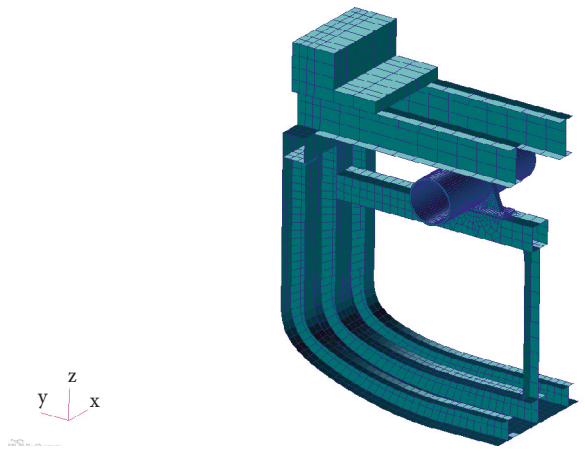

Figure 11: Connection simulation of the backbone to the hull.

Table 4: Comparison of predicted dry and wet natural frequencies in the full load condition.

Mode		Dry mode			Wet mode		
Direction	Modal shape	Test	Cal	Error (%)	Test	Cal	Error (%)
VB	2-Node	3.823	3.766	1.5	2.825	2.785	1.4
VB	3-Node	8.575	8.361	2.5	6.486	6.366	0.5

Table 5: Comparison of predicted dry and wet natural frequencies in design draft condition.

Mode		Dry mode			Wet mode		
Direction	Modal shape	Test	Cal	Error (%)	Test	Cal	Error (%)
VB	2-Node	4.337	4.28	1.4	3.104	2.992	3.6
VB	3-Node	9.923	9.46	4.7	6.955	7.098	2.1

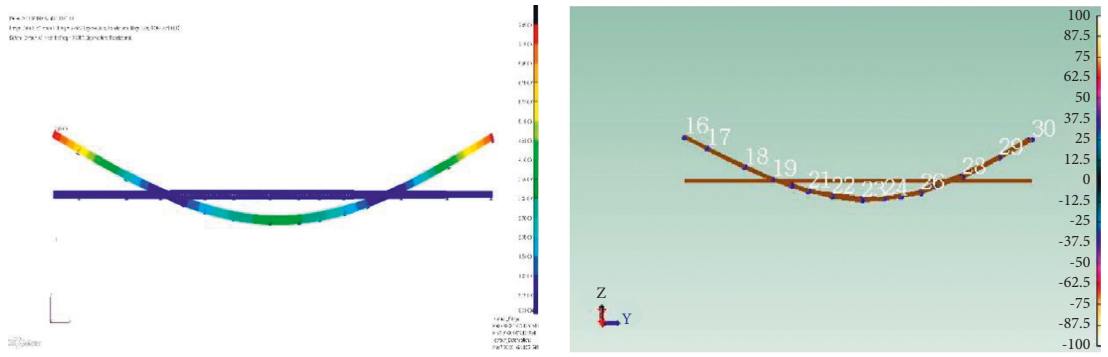

(a) (b)

Figure 12: Vertical bending modal shape (2 nodes), full loading condition. (a) Numerical prediction. (b) Measurement results.

full load condition and 494318 nodes and 314447 elements in the design draft condition.

5.2. Connection Simulation. The elements of the backbone are fixed by transversal supporting, which is connecting to the hull shell from the port side to the starboard as shown in Figure 11.

5.3. Natural Frequency Prediction. Based on the potential theory, the 3D hydroelastic method is employed. The key to the theory of hydroelasticity is the fluid-structure coupling; that is, the force is transmitted through the dry-wet matching relationship between the dry meshes and the wet surface elements. A set of 3742 hydrodynamic panels is modelled to calculate hydrodynamic coefficients, such as added mass, damping coefficient, and exited force. Using the dry–wet element matching, the fluid pressure is loaded on the structural meshes, while the elastic deformation is imposed on the wet panels. The dry and wet natural frequencies of the ship model are predicted for the previously mentioned FEM. The comparisons of the numerical results with the

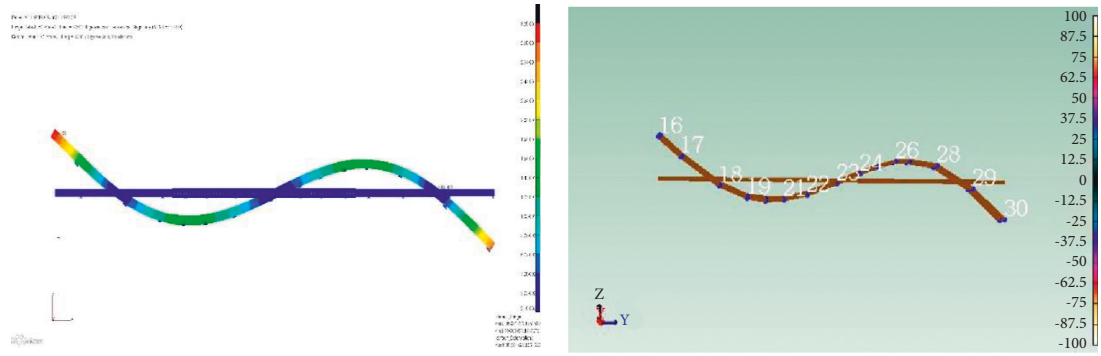

(a) (b)

Figure 13: Vertical bending modal shape (3 nodes), full loading condition. (a) Numerical prediction. (b) Measurement results.

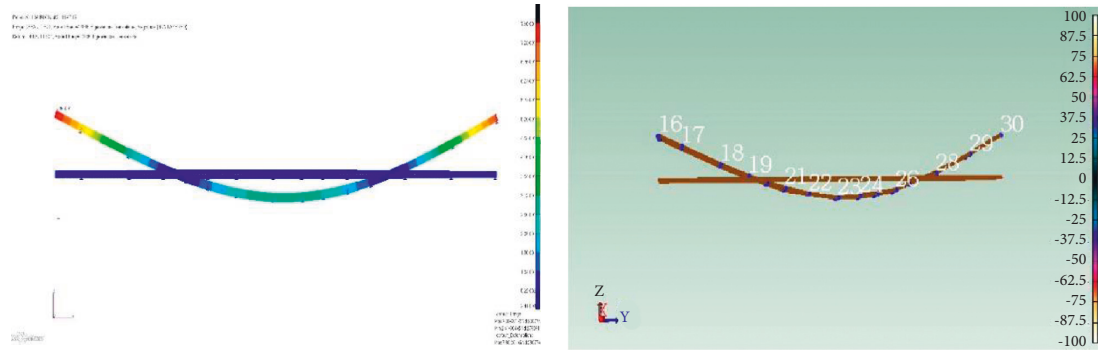

(a) (b)

Figure 14: Vertical bending modal shape (2 nodes), design draft loading condition. (a) Numerical prediction. (b) Measurement results.

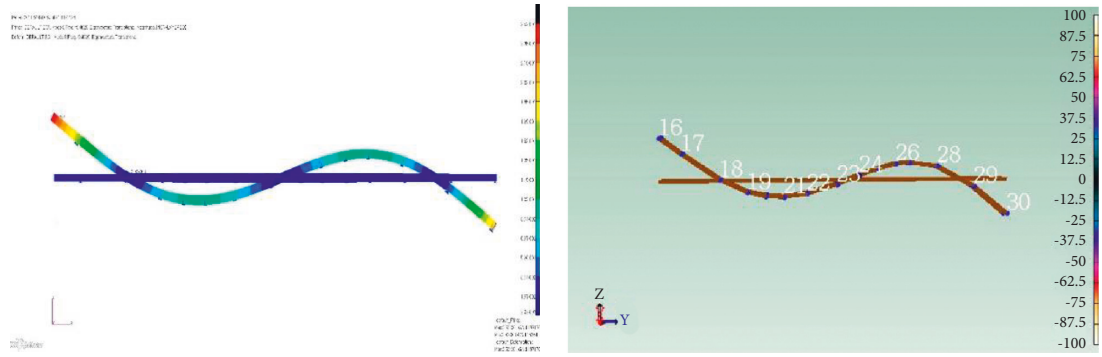

(a) (b)

Figure 15: Vertical bending modal shape (3 nodes), design draft loading condition. (a) Numerical prediction. (b) Measurement results.

measurement results are shown in Tables 4 and 5 for full load and design draft loading conditions. It can be seen that for all the modes very good agreements are achieved both for dry and wet frequencies.

5.4. Modal Shape Prediction. The vertical bending modal shape prediction results are shown in the following figures. The modal shapes derived from modal measurement are also given for comparison. Figures 12-13 show the comparison results of 2-node and 3-node vertical bending shapes in full loading condition, while Figures 14-15 give the comparison of the results of 2-node and 3-node vertical bending shapes in design draft loading condition. Generally speaking, a fairly good agreement has been achieved.

6. Conclusion

In the CSSRC-20,000 TEU JIP, a 20,000 TEU containership with an overall length of about 400 m is designed as the target ship, which will be utilized to carry out a model test in the new seakeeping wave basin of CSSRC and generate

benchmark model test data for comparative studies using most recent numerical methods and software. In this paper, the 1 : 49 scale ship model is briefly introduced, in conjunction with the determination of modal parameters, including natural frequencies, modal shapes, and damping ratio of the ship model, since they are the indispensable input data for hydroelastic analyses.

Through the comparative analysis of modal calculation and test results, the mass distribution and stiffness distribution of the containership model are the basis for obtaining the natural frequency and modal shape. In the finite element numerical modelling, only by simulating the segmental mass of the actual ship model and measuring the stiffness of the backbone, the accurate result of the natural frequency would be obtained. In addition, the simulation of all connections of the ship model will also change the results. However, there are some uncertain factors in the manufacture and installation of the ship model. Furthermore, the stiffness of the suspension rope and the position of the suspension point in the modal test are also factors that affect the results. By checking and eliminating all uncertain factors, the dry and wet modalities of the numerical modal calculation can be consistent with the results of the modal test. Natural frequency and modal observations of the containership model are required to ensure the accuracy of the hydroelastic analysis.

A 3D FEM of the ship is built to carry out modal analysis in a vacuum. From the comparison of the numerical predictions and the hammering test results, it can be concluded that a generally good agreement has been achieved, particularly for the lower-order deflection modes. The FEM corresponding to full load and design draft loading conditions will be distributed to JIP members for further comparative studies of linear and nonlinear hydroelastic analyses.

This article is devoted to the full exposition of the modal tests necessary for the hydroelastic analysis of large containerships. Therefore, hydroelastic effects can be seen in the elastic vibration frequencies and modes of the containership model. The wet mode of the containership model is obtained through hydrodynamic analysis. By comparing with the test results, the position and shape of the resonance frequency that causes the ship's hydroelasticity can be observed more clearly.

Data Availability

The data used to support the findings of this study are included in the article. The basic data can be found at jip.cssrc.com.

Conflicts of Interest

The authors declare that they have no conflicts of interest.

Acknowledgments

This research work was supported by the National Natural Science Foundation of China, PR China (51809241), CSSRC-20, 000TEU JIP, and the High-Tech Ship Research Projects Sponsored by MIIT.

References

[1] A. D. Papanikolaou and T. E. Schellin, "A three-dimensional panel method for motions and loads of ships with forward speed," *Journal for Research in Shipbuilding and Related Subject*, vol. 39, no. 4, pp. 145–156, 1992.

[2] Y. Welaya, T. M. Ahmed, and H. S. Wahab, "A linear three-dimensional frequency-domain numerical model for the prediction of ship motions in regular/irregular seaways," *Towards Green Marine Technology and Transport*Taylor & Francis Group, Milton Park, Oxfordshire, UK, pp. 167–174, 2015.

[3] J. Jiao, S. Huang, S. Wang, and C. Guedes Soares, "A CFD–FEA two-way coupling method for predicting ship wave loads and hydroelastic responses," *Applied Ocean Research*, vol. 117, Article ID 102919, 2021.

[4] P. A. K. Lakshmynarayanana and S. Hirdaris, "Comparison of nonlinear one- and two-way FFSI methods for the prediction of the symmetric response of a containership in waves," *Ocean Engineering*, vol. 203, pp. 1–17, Article ID 107179, 2020.

[5] J.-H. Kim and Y. Kim, "Numerical analysis on springing and whipping using fully-coupled FSI models," *Ocean Engineering*, vol. 91, pp. 28–50, 2014.

[6] I. Senjanović, N. Vladimir, N. Hadžić, and M. Tomić, "Beam structural modelling in hydroelastic analysis of ultra large container ships," *Recent Advances in Vibration Analysis*, University of Ottawa, Ottawa, Canada, pp. 193–222, 2011.

[7] S. Malenica and Q. Derbanne, "Hydro-structural issues in the design of ultra large container ships," *International Journal of Naval Architecture and Ocean Engineering*, vol. 6, no. 4, pp. 983–999, 2014.

[8] S. E. Hirdaris, Y. Lee, and G. Mortola, "The influence of nonlinearities on the symmetric hydrodynamic response of a 10,000 TEU Containership," *Ocean Engineering*, vol. 111, pp. 166–178, 2016.

[9] W. Ye, G. Yu, and X. Lu, "Hydroelastic analysis of container ships," *Vibration and Shock*, vol. 2, pp. 69–71, 1995.

[10] Y. Lin, H. Guo, and G. Yang, "Research on the hydroelastic effect of ultra large container ships," *Ship Engineering*, vol. 37, no. s2, pp. 15–19, 2015.

[11] Y. Chen, "Practical calculation methods of wave-induced vibration and whipping effects in ship design. In memory of Academician Binghan Xu," in *Proceedings of the Conference on Ship and Ocean Structure Mechanics*, Wuxi, China, 2011.

[12] Y. Han, L. Chen, and W. Wang, "Structure design of ultra-large container ship," *Ship and Ocean Engineering*, vol. 31, no. 04, pp. 10–17, 2015.

[13] Z. Zhang, L. Dandan, and L. Yan, "Research on the influence of wave-induced vibration on the fatigue strength of ultra-large container ships," *China Shipbuilding*, vol. 60, no. 1, pp. 1–10, 2019.

[14] I. Senjanović, S. Malenica, and S. Tomas, "Investigation of ship hydroelasticity," *Ocean Engineering*, vol. 35, no. 5-6, pp. 523–535, 2008.

[15] I. Senjanović, S. Malenica, and S. Tomašević, "Hydroelasticity of large container ships," *Marine Structures*, vol. 22, no. 2, pp. 287–314, 2009.

[16] W. Wang and C. Guedes Soares, "Review of ship slamming loads and responses," *Journal of Marine Science and Application*, vol. 16, no. 4, pp. 427–445, 2017.

[17] Y. Wu, R. Z. Chen, and J. Lin, "Experimental technique of hydroelastic ship model," in *Proceedings of the 3rd International Conference on Hydroelasticity in Marine Technology*, pp. 131–142, Oxford, UK, September 2003.

Hindawi
Shock and Vibration
Volume 2022, Article ID 4330043, 8 pages
https://doi.org/10.1155/2022/4330043

Research Article

Numerical Study on the Water Entry Impact Forces of an Air-Launched Underwater Glider under Wave Conditions

Xiangcheng Wu,[1] Xin Chang,[1] Shewen Liu,[1] Pengyao Yu,[1] Lilei Zhou,[2] and Wei Tian[3]

[1]*Naval Architecture and Ocean Engineering College, Dalian Maritime University, Dalian, China*
[2]*Dalian Shipbuilding Industry Offshore Co., LTD, Dalian, China*
[3]*No. 719 Research Institute of China State Shipbuilding Company Limiteo, Wuhan, China*

Correspondence should be addressed to Xin Chang; changxin_heu@outlook.com

Received 30 December 2021; Revised 10 March 2022; Accepted 24 March 2022; Published 12 April 2022

Academic Editor: Desmond Adair

Copyright © 2022 Xiangcheng Wu et al. This is an open access article distributed under the Creative Commons Attribution License, which permits unrestricted use, distribution, and reproduction in any medium, provided the original work is properly cited.

In this study, the water entry of an air-launched underwater glider under wave conditions is numerically simulated by the computational fluid dynamics method. The numerical model is validated by the comparison of nondimensional water entry impact force with published experimental and numerical results. And the influence of water entry points, water entry angles, and water entry attack angles on impact force is studied, which provides guidance for the design of air-launched underwater gliders. The results show that the water entry point has a great influence on the peak value of vertical impact force. In the present study, the peak value of the maximum vertical impact force at different water entry points is almost twice the minimum peak value with the same water entry velocity. The water entry angle at the same water entry point has great influence on the peak value of horizontal impact force, which is mainly related to the horizontal component of the impact velocity. The greater the horizontal component of impact velocity, the greater the peak value of impact force. In addition, the attack angle hardly affects the water entry impact force of the glider with hemispherical head.

1. Introduction

The underwater glider is a kind of autonomous underwater vehicle which has been broadly applied in physical and biological oceanography [1]. At present, underwater gliders are mainly deployed by ships. Limited by the navigation capacity of the mother ship, long-distance deployment takes a long time. In contrast, air launched from the aircraft can greatly shorten the time required for long-distance deployment [2]. However, the water entry of the air-launched underwater glider is a complex process. During water entry, the air-launched underwater glider will suffer a huge impact force that can damage the structure and inner components [3]. Therefore, it is necessary to study the water entry impact force of the air-launched underwater glider.

The theoretical research on water entry can be traced back to Karman [4]. Based on the theory of potential flow, von Karman calculated the impact loads of a structure into water. Wagner [5] refined the theory of von Karman by taking the piled-up water surface and spray thickness into consideration. Miloh [6] used the semi-Wagner approach to compute the wetting factor and slamming coefficient of a rigid sphere in vertical water entry. Korobkin [7] constructed an exact solution for the problem of an elliptical paraboloid entering an ideal, incompressible liquid at variable velocity within framework of the Wagner approximation and examined the effect of the shape on peak impact accelerations. Tassin et al. [8] analyzed the accuracy of several models for prediction of the hydrodynamic loads by comparing with the experimental observation data.

With the development of computer simulation technology, many computational fluid dynamics (CFD) techniques have been used to study the impact problems of water entry. Aquelet et al. [9] presented the prediction of the local high-pressure load on a rigid wedge impacting a free surface, where the fluid was represented by solving the Navier–

Stokes equations with an arbitrary Lagrange Euler (ALE) formulation. Panciroli et al. [10] studied the hydroelastic phenomena during the water entry of elastic wedges by the numerical model which is based on the coupled finite element method (FEM) and smoothed particle hydrodynamics (SPH) formulation. The results show that the numerical solutions agree reasonably well with the experimental data. Facci et al. [11] used the finite volume method (FVM) to discretize incompressible Navier–Stokes equations in both air and water and describe the free-surface multiphase flow by the method of volume of fluid (VOF). This method is proved to be reasonable and feasible in simulating the three-dimensional water entry of a solid body. Large eddy simulation (LES) can well calculate the problem of multiphase flow [12–14]. Li et al. used LES to study the problem of a stone impacting on the water. And the numerical model is verified to be reasonable by comparing the numerical results with experimental results [15].

Subsequently, scholars applied CFD techniques to the water entry study of air-launched autonomous underwater vehicles (AUVs). Shi et al. [16] and Chaudhry et al. [17] investigated the water entry process of air-launched AUV by the software LS-DYNA based on the ALE method. The simulation results such as cavity shape and impact loads show good agreement with experimental data. Yan et al. [18] studied the small-angle water entry problem of the AUV numerically by the FEM-SPH coupling algorithm. This method absorbs the advantages of SPH algorithm in dealing with large deformation and meshes distortion. CFD technology can also accurately simulate the problem of AUV entering water. Qi et al. [19] simulated the water entry process of air-launched AUVs. A series of accurate load data were obtained and the accompanied phenomena such as cavitation were observed. Wang et al. [20] simulated the high-speed water entry of AUVs with asymmetric nose shapes. The trajectory and cavity development were accurately simulated.

As reviewed above, the CFD technology has been proved to be a reasonable and feasible method to study the water entry problem. To our knowledge, previous studies mainly focused on the impact forces of AUV onto the static water and the effect of waves on the water entry impact forces of AUV has not been fully investigated. In this study, the water entry impact forces of an air-launched underwater glider under wave conditions are studied by the CFD method. The water entry impact forces at different water entry points and different water entry angles are studied. The results can provide a reference for the design of air-launched underwater gliders.

The study is organised as follows. Section 2 introduces the numerical model. Section 3 verifies the accuracy of the present numerical model. Section 4 analyses the water entry impact forces of an air-launched underwater glider in different water entry points, water entry angles, and attack angles. Section 5 summarises the main conclusions.

2. Numerical Model

2.1. Governing Equations. The commercial CFD software STAR-CCM+ is employed to solve the water entry impact forces in this paper. The unsteady Reynolds Averaged Navier–Stokes (RANS) equations are discretized by using FVM. It is assumed that the fluid is incompressible and the temperature is constant. Then, the continuity equation and the NS equations can be written as

$$\nabla \cdot \mathbf{u} = 0,$$
$$\frac{\partial \mathbf{u}}{\partial t} + (\mathbf{u} \cdot \nabla)\mathbf{u} = -\frac{1}{\rho}\nabla p + \nu \nabla^2 \mathbf{u} + \mathbf{F}, \tag{1}$$

where $\mathbf{u}$ is the velocity vector, ρ is the fluid density, p is the fluid pressure, ν is the fluid kinematic viscosity, and $\mathbf{F}$ is the volume force.

The method of VOF is used to capture the free-surface multiphase flow. In each grid, the sum of the volume fraction of air phase and water phase is 1.0. Suppose the volume fraction of air is γ and the volume fraction of water is $1 - \gamma$. Then, the free surface can be tracked by solving the volume fraction of air phase, and the governing equation can be expressed as [21]

$$\frac{\partial \gamma}{\partial t} + \nabla \cdot (\gamma \mathbf{v_r}) = 0, \tag{2}$$

where $\mathbf{v_r}$ is the transfer velocity.

There are three possible conditions in every grid as follows:

$$\gamma = \begin{cases} 0, & \text{if grid is full of water,} \\ 1, & \text{if grid is full of air,} \\ 0 < \gamma < 1, & \text{if grid contains both water and air.} \end{cases} \tag{3}$$

Then, the air and water in every grid can be regarded as an equivalent fluid with the density ρ_e and the viscosity ν_e calculated by

$$\rho_e = \gamma \rho_a + (1 - \gamma)\rho_w,$$
$$\nu_e = \gamma \nu_a + (1 - \gamma)\nu_w, \tag{4}$$

where ρ_a and ρ_w are the density of air and water, respectively, and ν_a and ν_w are the dynamic viscosity of air and water, respectively.

In addition, the motion of the structure is computed by Newton's second law. The motion of the grid around the structure is realized by overset mesh method. The transfer of physical quantities between the overset zone and the background zone is employed by the linear interpolation method.

2.2. Air-Launched Underwater Glider Model. In this study, an air-launched underwater glider model is proposed to study the water entry problem, which is shown in Figure 1. The traditional underwater glider has a large wingspan to improve the lift force during gliding. And the wing bears a large impact force in the process of water entry. So, a new design scheme, equipping a foldable wing module on the top of the underwater glider, is proposed to reduce the water entry impact force in this paper. During the impact into water, the wing is folded, as shown in Figure 1(a). After entering the water, the velocity of the glider decreases and

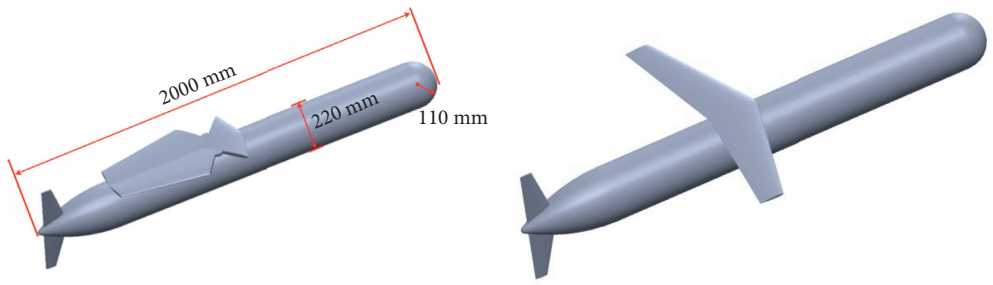

Figure 1: Schematic of the air-launched underwater glider. (a) Wing folded. (b) Wing unfolded.

the load it bears becomes smaller. Then, the wing spreads out, as shown in Figure 1(b). The length of the glider is 2000 mm, the diameter is 220 mm, and the mass is 70.69 kg. The head of the glider is a hemisphere with the radius of 110 mm. When the wing is folded, the gravity centre is on the central axis of the main body, 952 mm away from the head. And in the present study, the glider is regarded as a rigid body.

2.3. Reference Frames. In this study, the inertial frame $O-\mathrm{XYZ}$, the body frame $O_0-X_0Y_0Z_0$, and the velocity frame $V-V_1V_2V_3$ are adopted to describe the motion of the glider and are shown in Figure 2.

The inertial frame $O-\mathrm{XYZ}$ is fixed in the inertial space and an appropriate location on the water surface is selected for the origin O. The $O-X$ axis is horizontal and points to the motion direction of the glider, and the $O-Z$ axis is perpendicular to the water surface and points upwards. The origin of body frame $O_0-X_0Y_0Z_0$ is fixed at the gravity center of the glider, and the O_0-X_0 axis coincides with the longitudinal axis of the glider. The origin of velocity frame $V-V_1V_2V_3$ is also fixed at the gravity centre of the glider, and the $V-V_1$ axis coincides with the velocity vector of the glider. The angle between the $V-V_1$ axis and water surface is defined as the water entry angle θ. And the angle between O_0-X_0 axis and $V-V_1$ axis is defined as the attack angle α, which is positive when the angle $X_0O_0V_1$ is clockwise.

2.4. Computational Domain. As shown in Figure 3, only half of the domain is meshed as the body is axisymmetric. In the present study, the first order Stokes wave model is used. And the wave length and wave height are set as $\lambda = 10$m and $H = 1$m, respectively.

The surface abb′a′ is set to velocity inlet and 1.5λ away from the glider. The surface cdd′c′ is set to pressure out and 2.5λ away from the glider. A damping zone is set at the pressure outlet boundary to eliminate reflections from boundary. And the damping length is set to 10 m, which is equal to the wave length. The top, bottom, and side boundaries are assigned velocity inlet condition. The water depth is set to 4.5 m, and the height of the air domain is also set to 4.5 m. The SST (Menter) $k-\omega$ turbulence model is selected to simulate the surrounding flow with a grid point

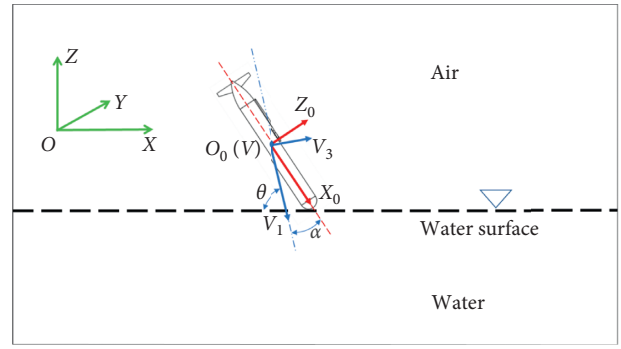

Figure 2: Reference frames.

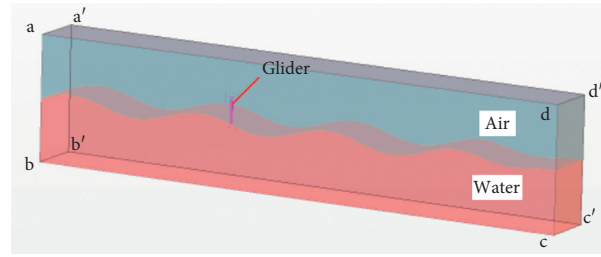

Figure 3: Computational domain.

for the first cell at $y^+ < 1$. The nondimensional wall distance y^+ is then given by

$$y^+ = \frac{y\rho u_*}{\mu}, \tag{5}$$

where y is the height of the wall adjacent cell centroid from the wall, u_* is the friction velocity, and μ is the dynamic viscosity.

In this study, the hexahedral mesh generated by the cutting mesh generator is used. To clearly simulate the variable process of water entry, fine mesh is assigned to the air-water interface and the region where the glider may pass. Figure 4 shows the partial mesh on the symmetry surface abcd.

3. Discussion on the Numerical Model

3.1. Numerical Method Validation. In this study, the example of the constant-velocity water entry of a sphere is used to verify the numerical method. And the accuracy of the

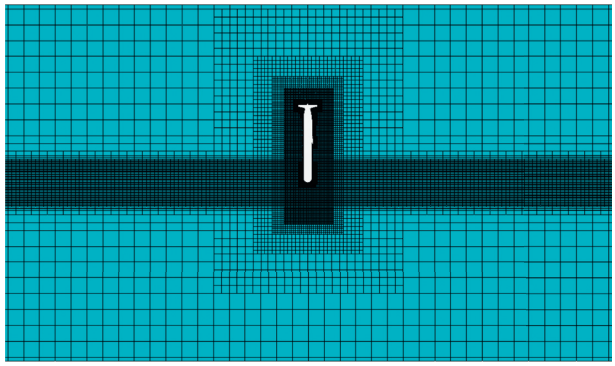

Figure 4: Partial mesh on the symmetry surface.

CFD results was validated by the comparison of nondimensional impact force with the published experimental and numerical results. The nondimensional impact force Cs is defined as

$$\mathbf{Cs} = \frac{2\mathbf{F}}{\rho\pi R^2 \mathbf{V}^2}, \tag{6}$$

where **F** is the total impact force of the sphere, R is the radius of the sphere, And **V** is the water entry velocity of the sphere.

The nondimensional penetration depth of the water entry of the sphere is defined as

$$D^* = \frac{D}{R}, \tag{7}$$

where D is the instantaneous penetration of the sphere.

In this section, the density of water is set to 1000 kg/m^3. The radius of the sphere is set to 110 mm, which is the same size as the glider head. And the water entry velocity is set to 10 m/s.

As shown in Figure 5, the comparison indicates that the vertical impact force obtained from the present model are in good agreement with the experimental data of Nisewanger [22] and Baldwin and Steves [23] and the numerical result by Xiao and Zhang [24]. Finally, the numerical model in this study is proved to be capable of simulating impact force acting on the structure during water entry.

3.2. Convergence Study. The setting of the mesh density and time step will directly affect the accuracy of the numerical results. A case of vertical water entry at the wave peak is used to verify the rationality of the mesh density and time step, as shown in Figure 6. And the impact velocity is set to 10 m/s.

Figure 7 shows the vertical impact force in the direction of $O-Z$ axis with three different mesh densities (coarse: 6.67×10^6; medium: 8.78×10^6; fine: 1.08×10^7). And the time step is set to 1×10^{-5} s for different mesh densities. The vertical impact force with different mesh densities show high consistency. And the mesh configuration with medium density is adopted to predict the impact force during water entry of the glider under wave condition. Then, three time steps are discussed in the time-step

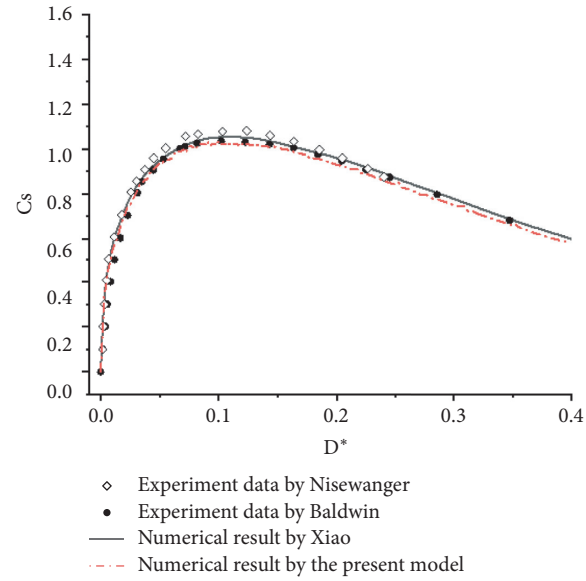

Figure 5: The comparison of nondimensional impact force.

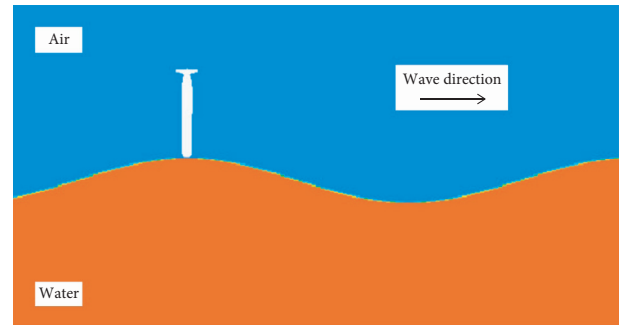

Figure 6: Schematic of convergence study case.

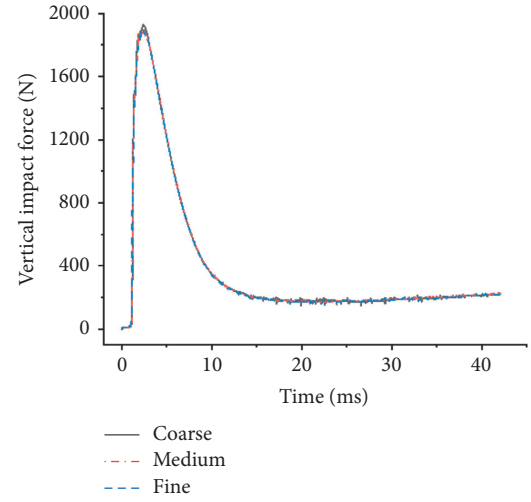

Figure 7: The vertical impact force with different mesh densities.

convergence study. As shown in Figure 8, the results of different time steps are in good convergence. Finally, the time step is set to 1×10^{-5} s in the study of water entry impact force.

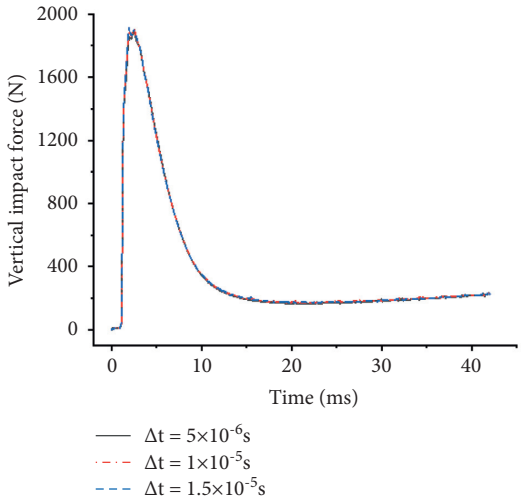

Figure 8: The vertical impact force with different time steps.

4. Results and Discussion

4.1. Influence of Water Entry Point on Impact Force. In this section, four typical water entry points are used to study the influence of water entry point on the impact force, which are the wave peak, the wave trough, and the cross points with the still water level. As shown in Figure 9, the cases that glider vertical water entry at different selected points are marked are Case 1, Case 2, Case 3, and Case 4, respectively.

The impact velocity is set as 10 m/s, and the water entry angle is set as 90 deg. The results of impact forces are shown in Figure 10. The vertical impact forces in the direction of $O-Z$ axis of the glider in Case 1 and Case 3 are almost equal. However, the horizontal forces in the direction of $O-X$ axis of the glider in Case 1 and Case 3 increase gradually in the opposite direction. This is related to the movement of water quality points. According to the first-order Stokes wave model, the horizontal velocity V_x and the vertical velocity V_z of the water quality points is defined as

$$V_x = a\omega\cos(\mathbf{K}\cdot x - \omega t)e^{Kz},$$
$$V_z = a\omega\sin(\mathbf{K}\cdot x - \omega t)e^{Kz}, \quad (8)$$

where a is the wave amplitude, ω is the wave frequency, $\mathbf{K}$ is the wave vector, K is the magnitude of the wave vector, and z is the vertical distance from the mean water level.

The wave surface has different inclination angles in different positions. Therefore, the glider entering the water vertically is subjected to horizontal impact force due to the inclination of the wave surface. At the wave peak and wave trough, the wave surface is horizontal. So, there is no horizontal impact force in the initial of water entry. With the increase of penetration depth, the movement of water quality point makes the glider in Case 1 and Case 3 subject to the opposite force.

In Case 2, the water quality point at the water entry point has the maximum positive vertical velocity. This maximizes the relative impact velocity of the glider. So, the glider in Case 2 has the maximal peak value of vertical impact force. Similarly, due to the minimum relative impact velocity, the glider in Case 4 has the minimal peak value of vertical impact force. In the present wave station and impact velocity, the peak value of the vertical impact force in Case 2 is almost twice the peak value in Case 4. In Case 2 and Case 4, the horizontal impact force is caused by the wave slope. Theoretically, the horizontal impact force of the glider in Case 2 and Case 4 should be symmetrical. However, in the present study, the water entry point is not strictly at the cross point. The water entry point in Case 2 is closer to the cross point, so the peak impact force is greater.

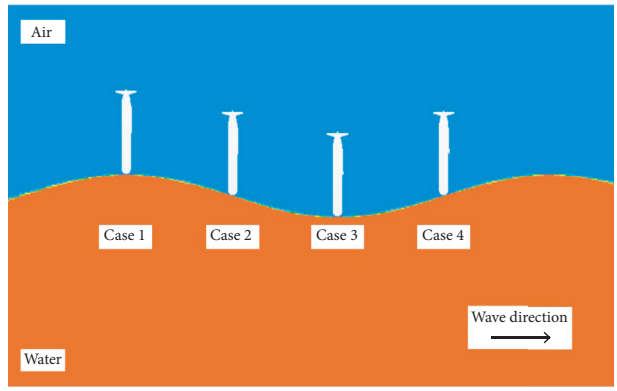

Figure 9: Schematic of vertical water entry at different points.

4.2. Influence of Water Entry Angle on Impact Force. In this section, five water entry angles are used to study the influence of water entry angles on the impact force, which are 80 deg, 90 deg, 100 deg, 110 deg, and 120 deg. According to the results of Section 4.1, the peak values of vertical and horizontal impact force of the glider in Case 2 are both largest. So, the same water entry point as Case 2 is selected. And the water entry velocity is also set to 10 m/s. The results of impact forces are shown in Figure 11. With the increase of water entry angle, the peak value of horizontal impact force increases gradually. This may be because the relative impact velocity in the horizontal direction increases with the increase of water entry angle. With the increase of water entry angle, the peak value of vertical impact force first increases and then decreases. This may be related to the inclination of the wave surface at the water entry point. On the one hand, with the increase of water entry angle, the water entry angle relative to the wave surface at the water entry point is also increasing. This increases the water entry impact force of the glider, and the vertical component of the impact force is also increasing. On the other hand, with the increase of water entry angle, the vertical component of velocity decreases and the vertical component of impact force also decreases. When the water entry angle is less than 100deg, the influence of relative water entry angle is greater, so the peak value of vertical impact force increases. When the water entry angle is 100deg to 110deg, the effects of the opposite effects are basically the same, so the peak value of vertical impact force is basically the same. With the further increase of water entry angle, the influence of vertical component of velocity is greater, so the peak value of vertical impact force decreases. In addition, both the peak values of vertical and horizontal

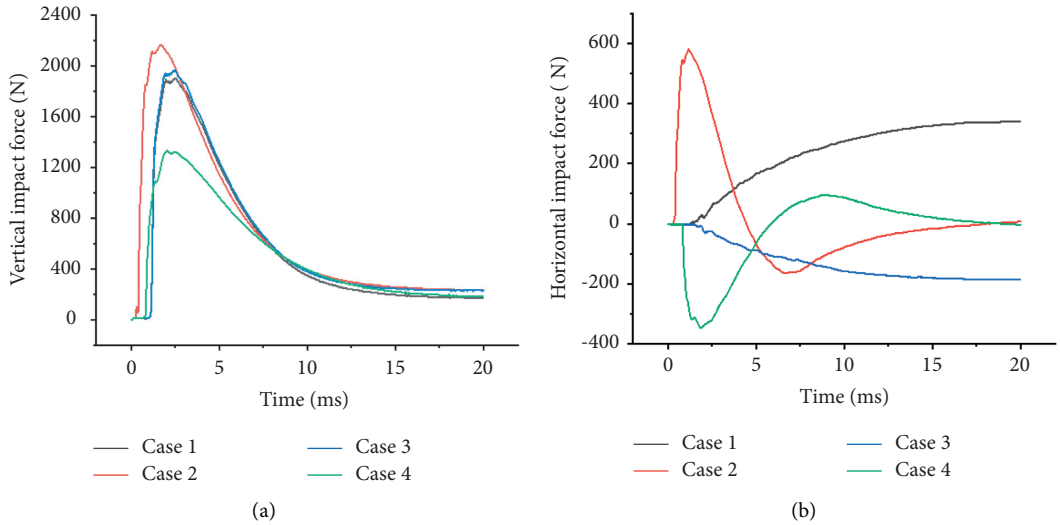

Figure 10: The impact forces with different water entry point. (a) Vertical impact forces. (b) Horizontal impact forces.

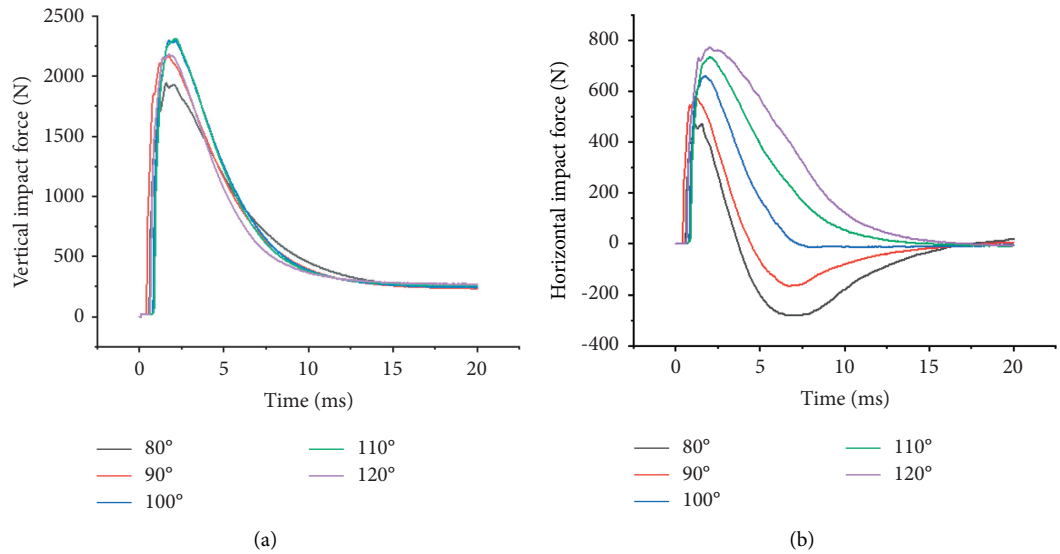

Figure 11: The impact forces with different water entry angles. (a) Vertical impact forces. (b) Horizontal impact forces.

impact force are bigger when the water entry angle is greater than 90 deg. Therefore, a water entry angle less than 90deg is a better choice.

4.3. Influence of the Attack Angle on Impact Force. In this section, five water entry attack angles are used to study the influence of attack angle on the impact force, which are −10 deg, −5 deg, 0 deg, 5 deg, and 10 deg. According to the results of Section 4.2, the peak values of vertical and horizontal impact force of the glider when the water entry angle is 110 deg are both largest. So, the same water entry point as Case 2 is selected, the water entry angle is set to 110 deg, and the water entry velocity is also set to 10 m/s. The results of impact forces are shown in Figure 12. The attack angle has little effect on the peak impact force. This may be because the glider's head is hemispherical. Then, the horizontal and vertical forces on the glider tend to be stable under different attack angles. In general, the attack angle has little effect on the peak impact force of the glider at the set entry attitude.

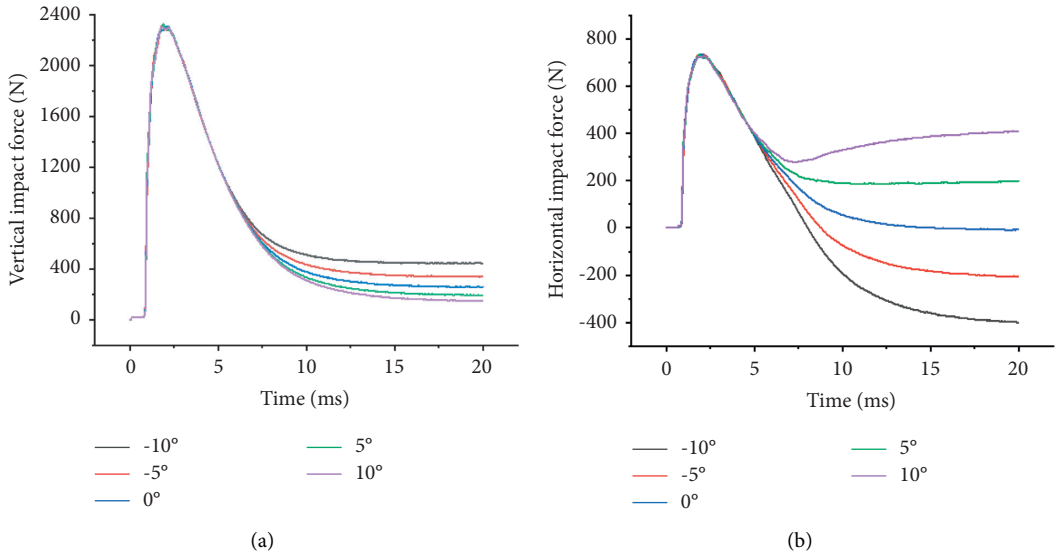

Figure 12: The impact forces with different attack angle. (a) Vertical impact forces. (b) Horizontal impact forces.

5. Conclusions

In this study, the water entry impact forces of an air-launched underwater glider under wave conditions are analyzed by numerical simulation. These results could be helpful to the design of air-launched underwater gliders. By studying the influence of water entry points, water entry angles, and attack angles on the impact force, we arrive at the following conclusions:

(1) The water entry points have a great influence on the peak value of vertical impact force. When the impact velocity is 10 m/s, the peak value of vertical impact force when water entry point is on the right side of wave peak and intersects with the still water level is almost twice the peak value when water entry at the intersection point on the left side of wave peak.

(2) The water entry angle has a great influence on the peak value of horizontal impact force when the water entry point intersects with the still water level. This is mainly related to the horizontal component of impact velocity. The greater the horizontal component of impact velocity, the greater the peak value of impact force.

(3) It should be avoided that the water entry direction is opposite to the wave direction, which makes the glider suffer greater impact force than along the wave direction.

(4) For the air-launched underwater glider with hemispherical head, the attack angle has little effect on the peak impact force.

Data Availability

The data used to support the findings of this study are included within the article.

Conflicts of Interest

The authors declare that they have no conflicts of interest.

Acknowledgments

This work was supported by the National Science Foundation of China (Grant no. 51709030); the State Key Laboratory of Ocean Engineering, Shanghai Jiao Tong University (Grant no. 1904), Natural Science Foundation of Liaoning Province in 2020 (Grant no. 2020-MS-125), the Fundamental Research Funds for the Central Universities (Grant nos. 3132021120 and 3132022123), and the Dalian High Level Talents Innovation Support Plan (2019RQ068).

References

[1] J-C Yu, A-Q Zhang, W-m Jin, Q. Chen, Y. Tian, and C-j Liu, "Development and experiments of the Sea-Wing underwater glider," *China Ocean Engineering*, vol. 25, no. 4, pp. 721–736, 2011.

[2] G. X. Yan, G. Pan, Y. Shi, L-M Chao, and D. Zhang, "Experimental and numerical investigation of water impact on air-launched AUVs," *Ocean Engineering*, vol. 167, pp. 156–168, 2018.

[3] A. Z. Chaudhry, Y. Shi, and G. Pan, "Study on the oblique water entry impact performance of AUV under different launch conditions based on coupled FEM-ALE method," *AIP Advances*, vol. 10, no. 11, Article ID 115020, 2020.

[4] T. V. Karman, *The Impact of Seaplane Floats during landing*, Technical Report Archive & Image Library, 1929.

[5] H. Wagner, "Phenomena associated with impacts and sliding on liquid surfaces," *Journal of Applied Mathematics and Mechanics*, vol. 12, no. 4, 1932.

[6] T. Miloh, "On the initial-stage slamming of a rigid sphere in a vertical water entry," *Applied Ocean Research*, vol. 13, no. 1, 1991.

[7] A. A. Korobkin, "The entry of an elliptical paraboloid into a liquid at variable velocity," *Pmm Journal of Applied Mathematics and Mechanics*, vol. 66, no. 1, 2002.
[8] A. Tassin, N. Jacques, A. E. M. Alaoui, A. Nême, and B. Leblé, "Assessment and comparison of several analytical models of water impact," *The International Journal of Multiphysics*, vol. 4, no. 2, pp. 125–140, 2010.
[9] N. Aquelet, M. Souli, and L. Olovsson, "Euler-Lagrange coupling with damping effects: application to slamming problems," *Computer Methods in Applied Mechanics and Engineering*, vol. 195, pp. 1–3, 2006.
[10] R. Panciroli, S. Abrate, G. Minak, and A. Zucchelli, "Hydroelasticity in water-entry problems: comparison between experimental and SPH results," *Composite Structures*, vol. 94, no. 2, pp. 532–539, 2012.
[11] A. L. Facci, M. Porfiri, and S. Ubertini, "Three-dimensional water entry of a solid body: a computational study," *Journal of Fluids and Structures*, vol. 66, 2016.
[12] M. Liu, L. Tan, and S. Cao, "Cavitation-Vortex-turbulence interaction and one-dimensional model prediction of pressure for hydrofoil ALE15 by large eddy simulation," *Journal of Fluids Engineering-Transactions of the Asme*, vol. 141, no. 2, 2019.
[13] M. Liu, L. Tan, Y. Liu, Y. Xu, and S. Cao, "Large eddy simulation of cavitation vortex interaction and pressure fluctuation around hydrofoil ALE 15," *Ocean Engineering*, vol. 163, pp. 264–274, 2018.
[14] M. Liu, L. Tan, and S. Cao, "Dynamic mode decomposition of cavitating flow around ALE 15 hydrofoil," *Renewable Energy*, vol. 139, 2019.
[15] C. Li, C. Wang, Y. Wei, and W. Xia, "Three-dimensional numerical simulation of cavity dynamics of a stone with different spinning velocities," *International Journal of Multiphase Flow*, vol. 129, Article ID 103339, 2020.
[16] Y. Shi, G. Pan, G. X. Yan, S. C. Yim, and J. Jiang, "Numerical study on the cavity characteristics and impact loads of AUV water entry," *Applied Ocean Research*, vol. 89, pp. 44–58, 2019.
[17] A. Z. Chaudhry, G. Pan, and Y. Shi, "Numerical evaluation of the hydrodynamic impact characteristics of the air launched AUV upon water entry," *Modern Physics Letters B*, vol. 34, no. 14, 2020.
[18] G. X. Yan, G. Pan, and Y. Shi, "Ricochet characteristics of AUVs during small-angle water entry process," *Mathematical Problems in Engineering*, vol. 2019, Article ID 9518437, 12 pages, 2019.
[19] D. Qi, J. Feng, B. Xu, J. Zhang, and Y. Li, "Investigation of water entry impact forces on airborne-launched AUVs," *Engineering Applications of Computational Fluid Mechanics*, vol. 10, no. 1, pp. 473–484, 2016.
[20] X. H. Wang, Y. Shi, G. Pan, X. Chen, and H. Zhao, "Numerical research on the high-speed water entry trajectories of AUVs with asymmetric nose shapes," *Ocean Engineering*, vol. 234, Article ID 109274, 2021.
[21] P. Yu, C. Shen, C. Zhen, H. Tang, and T. Wang, "Parametric study on the free-fall water entry of a sphere by using the RANS method," *Journal of Marine Science and Engineering*, vol. 7, no. 5, p. 122, 2019.
[22] C. Nisewanger, *Experimental Determination of Pressure Distribution on a Sphere during Water Entry*, Naval Ordnance Test Station China Lake CA, Ridgecrest, CA, USA, 1961.
[23] J. L. Baldwin and H. K. Steves, "Vertical water entry of spheres," *NASA STI/Recon Technical Report N*, vol. 76, 1975.
[24] H. Xiao and X. Zhang, "Numerical investigation of the fall rate of a sea-monitoring probe," *Ocean Engineering*, vol. 56, 2012.

Hindawi
Shock and Vibration
Volume 2022, Article ID 4564769, 18 pages
https://doi.org/10.1155/2022/4564769

Research Article

A Fully Coupled Time-Domain BEM-FEM Method for the Prediction of Symmetric Hydroelastic Responses of Ships with Forward Speed

Tushar Kanti Show,[1] **Spyros Hirdaris**,[1,2] **and Ranadev Datta**[1]

[1]*Indian Institute of Technology Kharagpur, Kharagpur 721302, West Bengal, India*
[2]*Aalto University, School of Engineering, Marine Technology Group, Espoo 02150, Finland*

Correspondence should be addressed to Spyros Hirdaris; spyros.hirdaris@aalto.fi and Ranadev Datta; ranadev@naval.iitkgp.ac.in

Received 24 December 2021; Revised 24 January 2022; Accepted 28 January 2022; Published 8 March 2022

Academic Editor: Shan Gao

Copyright © 2022 Tushar Kanti Show et al. This is an open access article distributed under the Creative Commons Attribution License, which permits unrestricted use, distribution, and reproduction in any medium, provided the original work is properly cited.

This paper presents a direct time-domain method for the prediction of symmetric hydroelastic responses of ships progressing with forward speed in small amplitude waves. A transient time-domain free surface Green function is used for the idealisation of the seakeeping problem using an Earth fixed coordinate system. Free surface ship hydrodynamics are idealised in the time domain by a Green function, and forward speed effects are idealised by a space-state model. Modal actions are accounted for by Timoshenko beam structural dynamics. Flexible fluid structure interaction (FFSI) coupling is enabled by a body boundary condition, and a direct integration Newmark-β scheme is used to obtain symmetric dynamic responses. The method is validated against available published numerical and experimental results. A parametric study for different container ship hull forms confirms that (i) forward speed effects should be taken under consideration as far as practically possible and (ii) hull flexibility effects accounting for hull shear deformation and rotary inertia are more notable for slender hull forms.

1. Introduction

In recent years, the economies of scale lead to increase in the numbers and sizes of large ocean-going vessels. For example, Ultra Large Container Ships (ULCSs) with capacity of more than 20,000 TEU and length and beam exceeding 400 m and 60 m, respectively, is today the norm that challenges the wave load margins introduced by classification rules [1]. Because of the slenderness and open deck configuration, these vessels are prone to springing and whipping-induced loads in stochastic seaways [2]. *Springing* is a phenomenon in which wave frequency or its harmonics are able to resonate at the structural natural frequency and may lead to fatigue failure. *Whipping* results from slamming of ships which causes transient dynamic loading along the hull girder. It is important for structural design as it imparts impact loads leading to fatigue failures [3, 4].

Hydroelastic idealisations used for the prediction of springing and whipping loads can be carried out in the frequency or time domains. "*Frequency-domain*" methods gained popularity since late 70s when the basic hydroelasticity theory combining strip theory and Timoshenko beam dynamics was introduced by Bishop and Price [5]. The three-dimensional version of this method was introduced by Bishop et al. [6]. Their approach combined FEA (for dry analysis) and frequency-domain Green function methods (for the wet analysis). To date, these methods have been applied successfully to a variety of merchant and naval ships, and their capability to simulate symmetric, antisymmetric, and asymmetric dynamic behaviour of ships in waves and for use in design has been widely demonstrated in the literature (e.g., [7–14]).

The concept of frequency-domain modal analysis has been successfully applied not only to describe steady-

state responses but also to describe the behaviour of symmetric transient responses due to slamming in irregular seaways [15–17]. Yet, comparisons between 2D time and frequency-domain techniques demonstrated that the effects of nonlinearities become particularly important at higher speeds and for ships with large flare [18]. Since the application of Reynolds-averaged Navier–Stokes computational fluid dynamics (RANS CFD) hydroelastic methods remains computationally time consuming (e.g., [19, 20], potential flow time-domain hydroelastic methods remain preferable for the prediction of the influence of whipping and springing loads for ship design and assessment.

"*Time-domain*" potential flow hydroelastic methods can be divided in two categories, namely, (a) the expanded Cummins' equation method and (b) direct simulation methods. In direct simulation methods, structural dynamics are idealised by finite elements and flexible fluid structure interaction (FFSI) is enabled by a boundary element method (BEM) on the interfacing boundaries (e.g., [21–32]). Although the direct coupling can be beneficial for strongly nonlinear problems, its applications are computationally expensive. On the other hand, the expansion of Cummins' equation method makes use of "*impulse response functions (IRFs)*," Fourier transformation, and structural dynamics and is therefore considered simpler in terms of computational modelling and efficiency (e.g., [33–39]).

Recently, Pal et al. [40, 41] used the 3D time-domain panel method based on time-domain free surface Green's function. The ship structure was modelled as an Euler beam. This work demonstrated that direct coupling hydroelastic methods can be more beneficial for strongly nonlinear problems as they allow for implicit implementation of wet modes and the easier inclusion of hydrodynamic nonlinearities. Weakly nonlinear hydroelasticity methods have also been presented by Kim et al. [26–28] and Jiao et al. [39]. The former used a Rankine panel method to idealise nonlinear hydrodynamics and a simplified finite element for Vlasov beam dynamics. The latter accounted for the influence of Froude–Krylov forces while radiation-diffraction forces were considered linear. Along these lines, it is now understood that Rankine panel or free surface time-domain panel methods are more suitable for inclusion of nonlinear radiation-diffraction forces. Segmented model tests are widely adopted for the measurement of ship hydroelastic motions and loads (e.g., [33, 42–46]). Notwithstanding this, results from model tests remain uncertain and generally unambiguous [47].

Building up from the work by Pal et al. [40], the originality and focus of this work is on exploring the adequacy of time-domain physical assumptions to model forward speed effects and exploring the influence of Timoshenko beam dynamics (rotary inertia and shear deformation effects) on predicting symmetric flexible dynamic response in waves. As explained in Section 2 of the paper, the formulation of the hydrodynamic problem is based on the model of Datta and Sen [48]; forward ship speed effects are idealised by a space-state function and modal actions are accounted for by Timoshenko beam structural dynamics. Flexible fluid structure interaction (FFSI) coupling is enabled by a body boundary condition, and a direct integration Newmark-β scheme is used to obtain symmetric dynamic responses. Results from a time-domain hydroelastic method that are compared for three different modern container ship hull forms and the experiments of Rajendran and Guedes Soares [33] are presented in Section 3. The influence of structural flexibility on ship responses is discussed in Section 4 and conclusions are drawn in Section 5.

2. Theory

Figure 1 presents the case of a flexible ship progressing with uniform forward speed U. The origin $Oxyz$ of the vessel lies in the Earth fixed coordinate system in way of the centre of gravity $G(X_s, Y_s, Z_s)$. The mathematical idealisation presented in the following sections comprises two parts, namely, "*structural dynamic*" and "*hydrodynamic*" idealisations. In the former, FEA-based Timoshenko beam structural dynamics are used to idealise the structural part of the FFSI problem. The boundary integral equation is then formulated using time-domain free surface Green's function, and FFSI coupling is enabled by a direct integration Newmark-β scheme [49].

2.1. Structural Dynamic Idealisation. The structure is assumed to behave as a slender nonuniform Timoshenko beam accounting for shear deformation and rotary inertia effects (see Figure 2) [50]. Transverse shear is assumed to be constant over the cross section. The rotation about the y axis is denoted by an independent function, namely, ψ. The dynamical behaviour of the ship hull due to hydrodynamic external force can be described by governing differential equations. In pure bending, the cross section maintains orthogonality, but in this work, the net slope of the natural axis is presented in terms of both flexure and the shear strain. In this formulation, w and ψ represent independent field variables idealising the transverse deflection of natural fibre and the angle of flexure, respectively. Therefore, the shear strains (ε) and stresses (σ) are, respectively, defined as $\varepsilon = -z$ and $\sigma = -Ez$. The vertical bending moment (M) and shear force (v) are defined as $M = EI$ and $v = GA_c k_s(\psi + dw/dx)$. In these formulations, G presents the modulus of rigidity (shear modulus) and A_s is the effective shear area. As the shear stress is not uniformly distributed over the cross section of the beam, considering uniform area overestimates the stresses. In an actual flexing scenario, the shear force will be lower and the effective shear area is defined as $A_s = A_c k_s$ where A_c is the cross-sectional area and k_s is the shear correction factor with values generally taken as 1.2 (i.e., approximately 80% of the area if considered effective in shear) for classic ship like beam idealisations [5, 51].

The ordinary differential equations expressing the shear forces and bending moments are defined, respectively, by (1) and (2) as

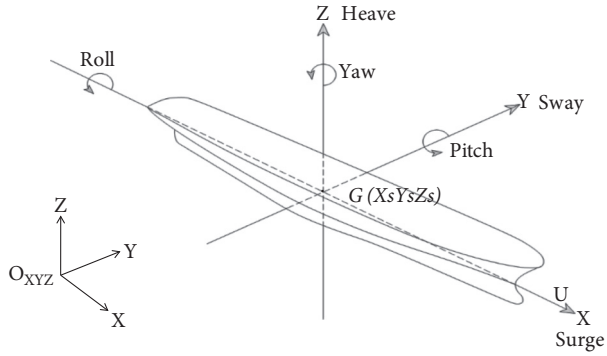

Figure 1: Schematic diagram of coordinate systems.

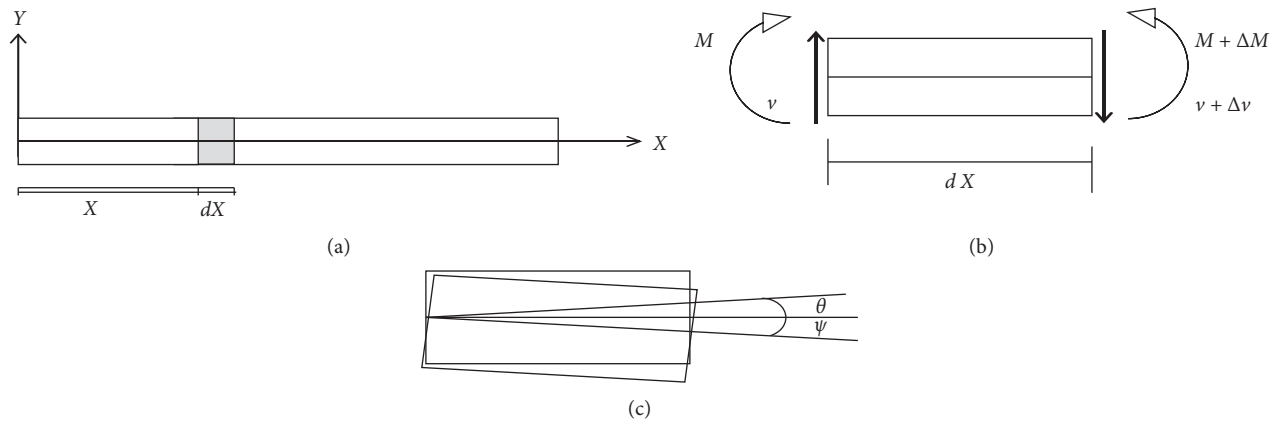

Figure 2: Section of a beam representing shear forces (V) and moments (M) at edges.

$$\frac{d}{dx}\left[GA_c k_s\left(\psi + \frac{dw}{dx}\right)\right] + f = 0, \tag{1}$$

$$\frac{d}{dx}\left(EI\frac{d\psi}{dx}\right) - GA_c k_s\left(\psi + \frac{dw}{dx}\right) = 0. \tag{2}$$

In equation (1), f represents the distributed load over the sectional element of the ship modelled as a beam. The weak form of (1) and (2) can be obtained by introducing two weight functions, namely, transverse deflection w and rotational function ψ, as independent unknowns. A "*Gaussian quadrature method (G-Q)*" can be applied to evaluate the weak form equations as follows:

$$\int_0^{h_e}\left(\frac{dw}{dx}\frac{d\alpha^b}{dx}GA_c k_s\right)dx + \left(\psi\frac{d\alpha^b}{dx}GA_c k_s\right)dx = \int_0^{h_e} f\alpha^b dx + \alpha^b(h_e)Q_1^e + Q_3^e\alpha^b(h_e), \tag{3}$$

$$\int_0^{h_e}\beta^s\frac{dw}{dx}GA_c k_s dx + \int_0^{h_e}\left[\frac{d\beta^s}{dx}\frac{d\psi}{dx}EI + \beta^s\psi GA_c k_s\right]dx = \beta^s(x_A)Q_2^e + Q_4^e\beta^s(h_e). \tag{4}$$

The weak form of the structural dynamic equations (3) and (4) is obtained by introducing two weight function α^b and β^S; h_e is the length of 1D finite element where x_A *an d* x_B are the two consecutive nodes of a beam-like element; Q_1^e and Q_3^e represent elemental shear forces; Q_2^e and Q_4^e denote elemental bending moments. To avoid the shear locking [52], the equations are equally interpolated by a "*reduced integration element (RIE).*" Accordingly, the elemental static equation can be written as

$$\begin{bmatrix} K^{11} & K^{12} \\ K^{21} & K^{22} \end{bmatrix}\begin{Bmatrix} w \\ \psi \end{Bmatrix} = \begin{bmatrix} f_1 \\ f_2 \end{bmatrix}. \tag{5}$$

In (5), the global stiffness (K_{ij}) operators are defined as

$$
\begin{aligned}
K_{ij}^{11} &= \int_{x_A}^{x_B} GA_c k_s \frac{d\psi_i^{(1)}}{dx} \frac{d\psi_j^{(1)}}{dx} dx, \quad (i = 1, 2, 3, \ldots\ldots n)(j = 1, 2, 3, \ldots\ldots n),\\
K_{ij}^{12} &= \int_{x_A}^{x_B} GA_c k_s \frac{d\psi_i^{(1)}}{dx} \psi_j^{(2)} dx, \quad (i = 1, 2, 3, \ldots\ldots n)(j = 1, 2, 3, \ldots\ldots n),\\
K_{ij}^{21} &= \int_{x_A}^{x_B} GA_c k_s \frac{d\psi_i^{(1)}}{dx} \psi_j^{(2)} dx, \quad (i = 1, 2, 3, \ldots\ldots n)(j = 1, 2, 3, \ldots\ldots n),\\
K_{ij}^{22} &= \int_{x_A}^{x_B} GA_c k_s \psi_i^{(2)} \psi_j^{(2)} dx + \int_{x_A}^{x_B} EI \frac{d\psi_i^2}{dx} \frac{d\psi_j^2}{dx} dx, \quad (i = 1, 2, 3, \ldots\ldots n)(j = 1, 2, 3, \ldots\ldots n).
\end{aligned} \tag{6}
$$

The shear stiffness is computed with one Gauss point. The mass matrix is defined as $[m]_{sb} = [m]_s + [m]_b$, where $[m]_s$ and $[m]_b$ represent the mass matrices for shear and bending criteria, respectively. Therefore, to determine the response history of the beam element, the global finite element equation for dry analysis is expressed as

$$[M]\{\ddot{x}\} + [C]\{\dot{x}\} + [K]\{x\} = \{F_{ext}\}. \tag{7}$$

In this equation of motion, the responses of the structure are demonstrated in the form of displacement (x), velocity ($\dot{x}$), and acceleration ($\ddot{x}$); $[M]$ and $[K]$ represent the global mass and stiffness matrices, $[C]$ is the damping matrix, and $\{F_{ext}\}$ is the global external force vector. The formulation presented assumes Rayleigh damping [53] where $[C] = \sigma_d[K] + \varsigma_d[M]$. The value of stiffness proportional coefficient (σ_d) and mass proportional coefficient (ς_d) is taken as presented by Liu et al. [54].

2.2. Hydrodynamic Idealisation. In (7), the external force $\{F_{ext}\}$ vector represents the wave induced loads and moments which may be calculated by solving the hydrodynamic problem. In this study, a 3D time-domain panel method based on transient free surface Green's function has been employed. The theory is formulated based on Earth fixed coordinate system. The complete formulation of the hydrodynamic problem for rigid body case is presented in multiple sources (e.g., [48, 55]). Therefore, the background to the method is only briefly presented here with the aim to explain its relevance for the solution of the hydroelasticity problem. In Figure 3, Ω represents a fluid domain of interest which is surrounded by the free surface S_F, bottom surface S_b, wetted body surface S_0, and the surfaces $S_{-\infty}$, S_∞ at infinity.

The total velocity potential $\phi^T(p,t)$ is defined as

$$\phi^T(p,t) = \phi^I(p,t) + \phi(p,t), \tag{8}$$

where $\phi^I(p,t)$ is the velocity potential of incident waves at any time instant (t) at any arbitrary point p on the fluid domain Ω and $\phi(p,t)$ is the disturbed potential that consists of radiation and diffraction components. Within the context of linear potential theory, solution for $\phi(p,t)$ can be obtained by solving following governing equation:

$$\nabla^2\phi(p,t) = 0, \text{for } p \in \Omega. \tag{9}$$

Using linear free surface boundary condition, body boundary condition, bottom boundary condition, and radiation condition as follows:

$$
\begin{aligned}
&\frac{\partial^2\phi}{\partial t^2} + g\frac{\partial\phi}{\partial z} = 0 \text{ at } z = 0,\\
&\frac{\partial\phi}{\partial n} = v_n(x,t) - \frac{\partial\phi^I}{\partial n} \text{ on } S_0,\\
&\frac{\partial\phi}{\partial z} = 0 \text{ on } S_b\\
&\phi, \frac{\partial\phi}{\partial t} = 0 \text{ at } S_\infty
\end{aligned} \tag{10}
$$

within the context of rigid body ship dynamics, we can assume that the normal velocity of the body is taken as a function of time. However, if we account for the influence of hydroelasticity, the velocity of the body should be idealised by a state-space function. Considering that the formulation is based on Earth fixed coordinate system, consideration of the so called "*m terms*" [26] is not required. To solve the hydrodynamic problem, transient free surface Green's function is used. The expression for $\phi(p,t)$ becomes

$$
\phi(p,t) = -\frac{1}{4\pi}\left\{\begin{aligned}
&\iint_{S_0} \sigma(q,t)G^o(p,q)dS + \int_0^t d\tau\left[\iint_{S_0} \sigma(q,t)G_t^f(p,q;t-\tau)dS\right]\\
&\qquad - \int_0^\tau d\tau\left[\frac{1}{g}\int_\Gamma \sigma(q,t)G_t^f(p,q;t-\tau)v_N v_n dL\right]
\end{aligned}\right\}. \tag{11}
$$

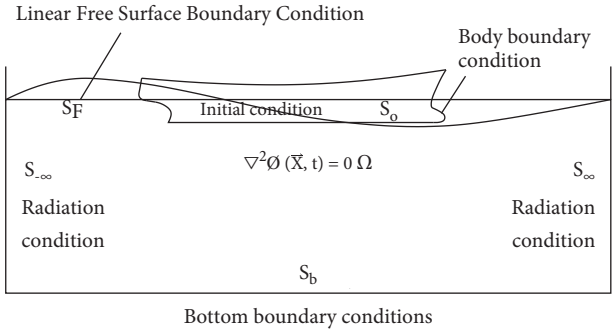

FIGURE 3: Hydrodynamic boundary domain and associated conditions (S denotes surface of relevance to boundary conditions).

The detailed expression for the derivation of (11) is given in Lin and Yue [55]; G^o presents the nonlinear part (Rankine part) of Green's function and G_t^f is the linear part (regular part) of Green's function [56]. This solution produces scattering of velocity potential $\phi(p,t)$ over the surface of the hull; v_N and v_n are normal to the water line Γ and the wetted surface, respectively; $\sigma(p,t)$ represents the strength of the source G; t and τ represent the present and past time increments used in the convolution time integral. The time dependent contribution comes from the second and third integrals that calculate the effect that comes from the disturbance caused in previous time steps. The third integral arises due to the forward speed effects with terms "t" and "τ" denoting the present and past instants in time.

The computation of the velocity potential term $\phi(p,t)$ leads to prediction of dynamic pressure $P(p,t)$ defined as

$$P(p,t) = -\rho_0 \left\{ \phi_t(p,t) - U\phi_x(p,t) + \phi_t^I(p,t) + \frac{1}{2}\left[\nabla\phi(p,t) + \nabla\phi^I(p,t)\right]^2 \right\}. \tag{12}$$

In (12), the density of the fluid is termed as ρ_0. For zero speed, the contribution of quadratic term can be ignored. However, when forward speed effects are accounted for, consideration of quadratic terms is essential. Accordingly, the method is not fully linear and fundamentally different from other time-domain formulations (e.g., [26, 39]). Solving (12) gives the distribution of the pressure at any arbitrary point at any instant of time t. If we assume that $P(\overline{X}, t)$ represents the collection of total dynamic pressure at any point on the sectional curve C_{S_x} for an arbitrary vertical section S_x, the sectional force F_{S_x} is defined as

$$F_{S_x} = \int_{C_{S_x}} P(\overline{X}, t).\hat{n}.dC_{S_x}, \tag{13}$$

where $(\overline{n})$ denotes the generalized normal on a section increment (dS_X).

The restoring force $F_i^{restoring}(t)$ at an i^{th} panel of a surface increment ds_i subject to normal $\overline{n}_i$ may expressed as

$$F_i^{restoring}(t) = -\rho_0 g \overline{Z}_i \delta\overline{n}_i.ds_i - \rho_0 g \delta\overline{Z}_i \overline{n}_i.ds_i, \tag{14}$$

where $\overline{Z}_i$ is the water head and δ denotes the leading order variation. Lower-order panel methods assume that variation over a hydrodynamic panel remains constant. As δ varies over the surface, this leading order variation might not be very effective, and therefore Kim et al. [26] proposed the use of a higher-order Rankine panel method. Notwithstanding this, the stability of the numerical idealisation can also be ensured by reducing the size of panels (i.e., using optimum number of fluid domain discretisation) when using a classic Green function method (e.g., [57]).

2.3. Flexible Fluid Structure Interaction (FFSI). Equation (7) may be solved by Newmark [49] time integration method. Accordingly, the nodal displacement vector $\{x\}$ at any time instant t is obtained from the equation

$$\begin{aligned}\left(\frac{[M]}{\alpha\Delta t^2} + \frac{\delta}{\alpha\Delta t}[C] + [K]\right)\{x\}_t = \{F\}_t + [M]\left[\frac{1}{\alpha\Delta t^2}\{x\}_{t-\Delta t} + \frac{1}{\alpha\Delta t}\{\dot{x}\}_{t-\Delta t} + \left(\frac{1}{2\alpha} - 1\right)\{\ddot{x}\}_{t-\Delta t}\right] \\ + [C]\left[\frac{\delta}{\alpha\Delta t}\{x\}_{t-\Delta t} + \left(\frac{\delta}{\alpha} - 1\right)\{\dot{x}\}_{t-\Delta t} + \frac{\Delta t}{2}\left(\frac{\delta}{\alpha} - 2\right)\{\ddot{x}\}_{t-\Delta t}\right].\end{aligned} \tag{15}$$

The stability and accuracy of the present numerical scheme during a time increment Δt is dependent on the parameters α and δ. These two parameters also describe the variation of the acceleration over a time step. The numerical values of α and δ in the above equation are in general taken as ¼ and ½, respectively (Kim et al., 2013). The time variations of the acceleration and velocity derivatives are defined as

$$\{\ddot{x}\}_t = \frac{1}{\alpha\Delta t^2}\left(\{x\}_t - \{x\}_{t-\Delta t}\right) - \frac{1}{\alpha\Delta t}\{\dot{x}\}_{t-\Delta t} - \left(\frac{1}{2\alpha} - 1\right)\{\ddot{x}\}_{t-\Delta t}, \tag{16}$$

$$\{\dot{x}\}_t = \{\dot{x}\}_{t-\Delta t} + \Delta t\left[(1-\delta)\{\ddot{x}\}_{t-\Delta t} + \delta\{\ddot{x}\}_t\right]. \tag{17}$$

Accordingly, the velocity and displacement at each section may be obtained from equations (15)–(17). By back substitution in equation (14), the boundary condition for the solution of the fluid problem is obtained and FFSI is enabled.

3. Results

Table 1 outlines the principal particulars of three container ship hulls that have been assessed using the method presented in this publication. The hydrodynamic idealisations for each design and the body plans are shown in Figure 4. The weight and flexural rigidity distributions for all containerships are depicted in Figure 5. Ship 1 is the well-known S175 container ship [46]. Ship 2 is a modern large container ship (LC) design studied under previous ISSC-ITTC benchmarks [3, 33, 58]. Ship 3 is a modern ultra-large container ship (ULC) [59].

The results presented in this paper are given in the nondimensional forms presented in Table 2. Numerical results based on the theory presented in Section 2 are named as TDFlex-T. The computations based on Datta and Soares [41] model are denoted as TDFlex-E, and the results from time-domain rigid body approach of Sengupta et al. [60] are referenced as TDRigid.

3.1. Validation Study. Figures 5(a)–5(d) demonstrate the time history of nondimensional vertical bending moments (VBMs) and shear forces (VSFs) of S175 and ULC at the wave matching region (i.e., $\lambda/L = 1$) for forward speed $F_n = 0.25$. The results presented converge to steady state. This confirms the numerical stability of the solution. In Tables 3–5, dry natural frequencies for the different modes of S175, LC, and ULC are compared against the Euler–Bernoulli models of Rajendran et al. [59] and Rajendran and Guedes Soares [33] as well as the superposition method of Wu and Hermundstad [18]. Variations in the natural frequencies can be attributed to the Timoshenko beam idealisation introduced in Section 2.

In Figure 6, the VBM transfer function for S175 hull at $F_n = 0.25$ is plotted and compared with the numerical method proposed by Datta and Guedes Soares [41] that has been based on an Euler beam model. the experimental results published by Iijima et al. [61]. The differences in the magnitude of the VBM value at the wave matching region ($\lambda/L = 1$) could be attributed to limitations of the linear hydrodynamic theory assumptions and structural idealisations. Notwithstanding this, it is thought that the approach presented captures very well the overall trend of the dynamic response.

Comparisons of results for amidships symmetric responses against [33] are depicted in Figure 7. Figure 7(a) presents a comparison of nondimensional displacement against nondimensional frequency. As shown in Figure 7(b), the magnitude of the VBM matches well with the other published results. Comparison of VBM along the hull for LC is demonstrated in Figure 8 at $F_n = 0.12$. Once again, the results compare well with experiments and the coupled BEM-FEM model given by Datta and Guedes Soares [41].

The VBM at amidships the ULC for $F_n = 0.135$ is shown in Figure 9. Results are compared with experiments by Rajendran et al. [59] and TDFlex-E. Both results underestimate the maximum VBM. However, the overall trend agrees very well with experimental values. It may be therefore concluded that the present numerical model is stable and consistent and captures the symmetric responses with reasonable accuracy.

4. Parametric Study

In this section, a parametric study is carried out to observe the effect of design parameters in symmetric hydroelastic responses such as vertical displacement, VSF, and VBM. The parametric study presented utilises S175 and ULC hulls. Special focus is attributed to the influence of structural rigidity, forward speed, ship length, and slenderness on dynamic response.

4.1. The Influence of Structural Rigidity. The vertical displacement RAO at midships and transfer functions of VSF at $+L/4$position from the aft of the ULC were compared between the flexible and rigid structures for $F_n = 0.135$. Figure 10 shows the comparison of the displacement response amplitude operator (RAO) for rigid and flexible structures over the nondimensional frequency $\omega\sqrt{L/g}$. Observed differences demonstrate that rigid body assumptions overestimate the structural responses. As shown in Figure 11, near the resonating frequency, the ship is likely to experience larger shear forces, which can only be captured if structural flexibility is taken into account. While TDFlex-T is capable of capturing this phenomenon, TDRigid fails to capture the same phenomenon. This implies the importance of capturing the influence of structural flexibility for slender vessels.

4.2. The Influence of Forward Speed. Figures 12(a), 12(b), 13(a), and 13(b) represent the VBM and VSF for S175 hull and the ULC hull, respectively, for different Froude numbers ($F_n = 0.135$, 0.2 , and 0.25). The VBM and VSF results are plotted against the nondimensional frequency $\omega\sqrt{L/g}$. It is observed that the peak symmetric loads drop rapidly with respect to the frequency. This implies that the chances of damage of the structure are higher at lower Froude number at lower frequency zone.

Table 1: General particulars of different container ship models.

General particulars		Ship type		
Notation (unit)	Item	S175	LC	ULC
L_{PP} (m)	Length between perpendiculars	175.0	286.6	333.43
B (m)	Beam	25.4	40.0	42.8
D (m)	Depth	11.0	24.2	27.3
T (m)	Draft	9.5	11.98	13.1
M (tonne)	Total mass	24560.0	85562.7	$1.25e+05$
LCG (m)	Longitudinal centre of gravity	2.78	4.9	4.7
k_{xx} (m)		10.16	14.4	16.94
k_{yy} (m)	Radii of gyration along longitudinal (xx); transverse (yy); and vertical (zz) axes	42.8	70.144	83.9
k_{zz} (m)		43.0	11.412	84.1

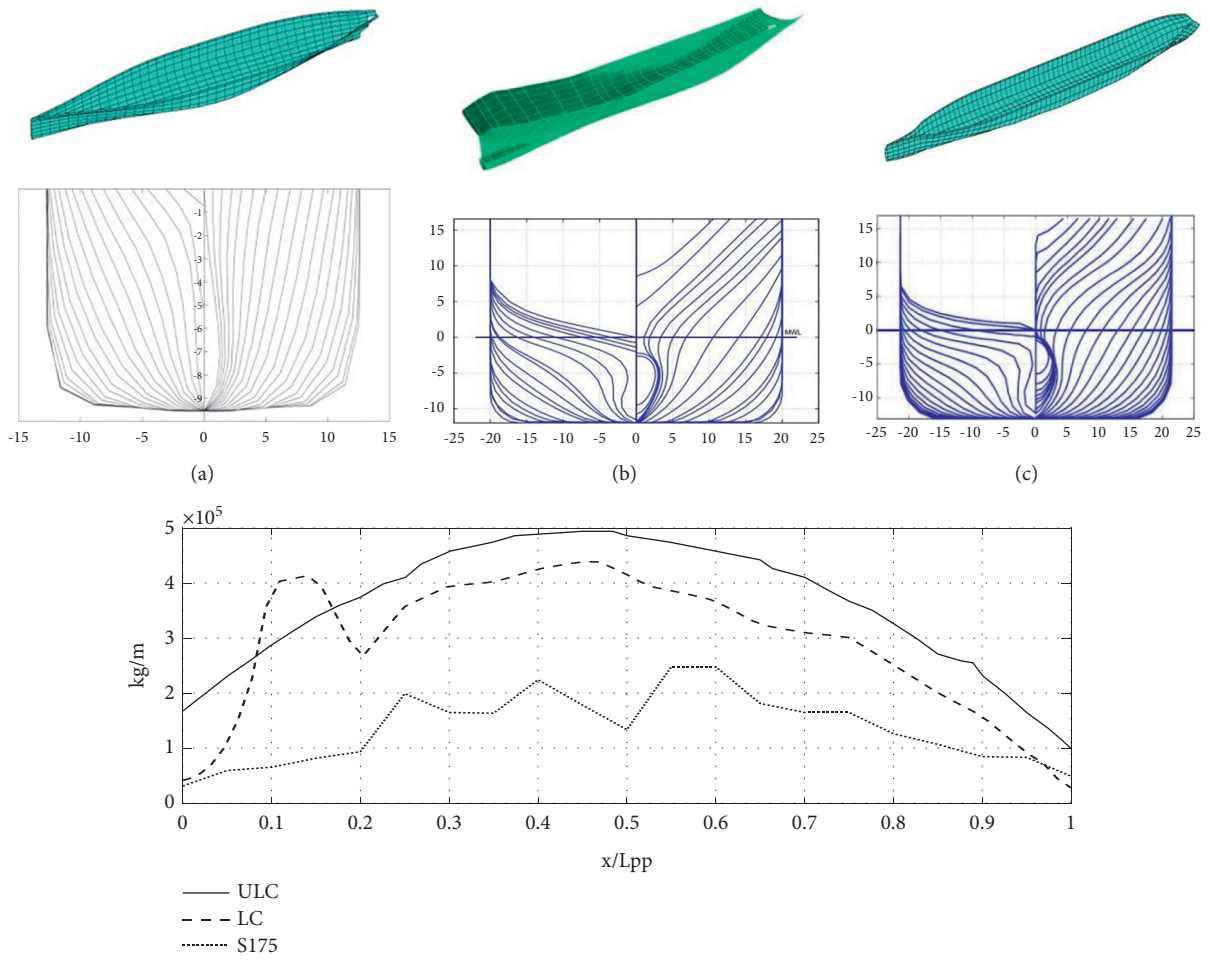

Figure 4: Continued.

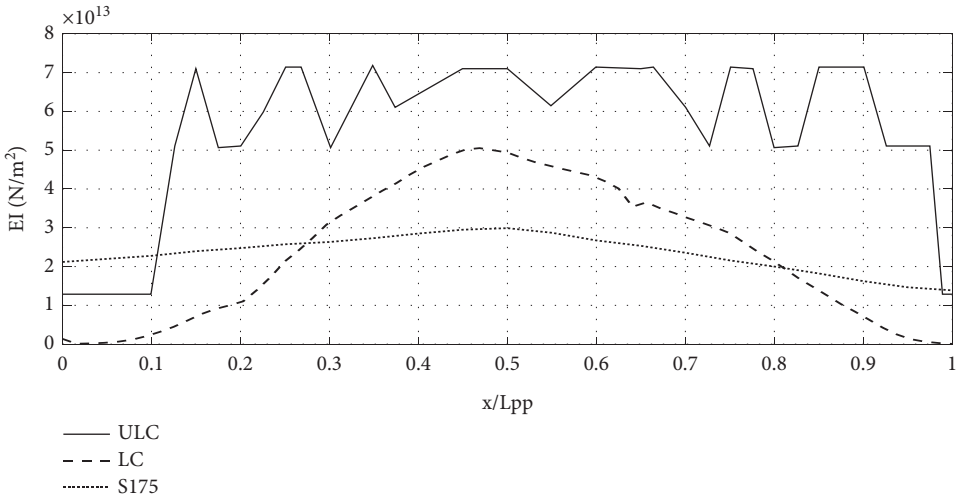

(e)

Figure 4: Body plan and hydrodynamic idealisations for different container ship models. (a) Ship 1: S175. (b) Ship 2: LC. (c) Ship 3: ULC. (d) Mass distributions. (e) Flexural rigidity distributions.

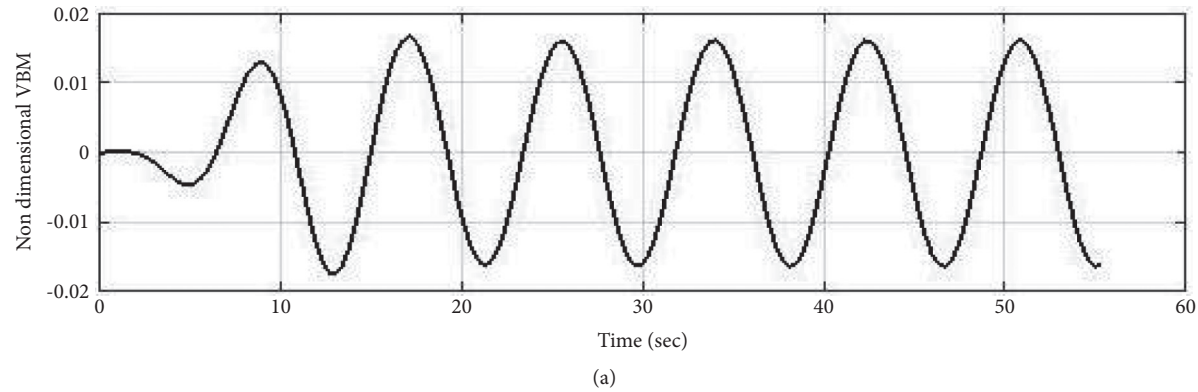

(a)

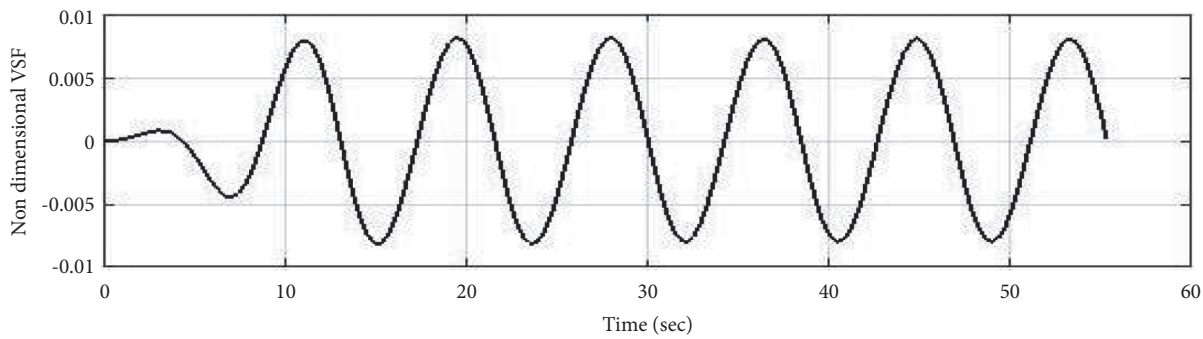

(b)

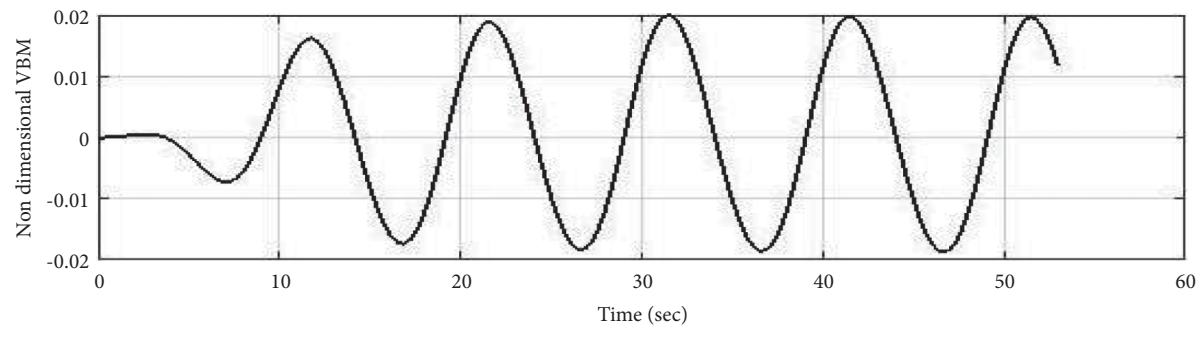

(c)

Figure 5: Continued.

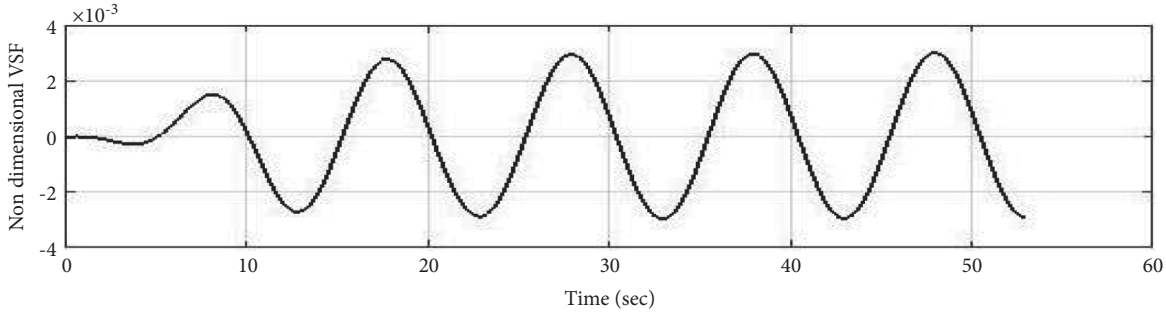

(d)

Figure 5: Symmetric load time histories for ULC and S175 container ships ($F_n = 0.25$, $\lambda/L = 1$). (a) VBM time history, S175. (b) VSF time history, S175. (c) VBM time history, ULC. (d) VSF time history, ULC.

Table 2: Nondimensional dynamic response parameters.

Parameters	Nondimensional format
Frequency (Hz)	$\omega\sqrt{\mathbf{L/g}}$, $\lambda/\mathbf{L}$
Time (sec)	$\mathbf{t/T}$
Vertical response (m)	$\lvert\mathbf{x}_3\rvert/\mathbf{A}$
Length along the horizontal axis	x/L
VSF (N/m^2)	$V/(\rho_0 g A L^2)$
VBM (N-m)	$M/(\rho_0 g A L^3)$

Table 3: Dry natural frequencies of the S175 for vertical flexural vibrations.

Mode no.	TDFlex-T (Hz)	Wu and Hermundstad [18] (Hz)	Difference (%)
1	0.3002	0.3024	−0.737
2	0.7299	0.7669	−0.950
3	1.3981	1.4006	−0.170

Table 4: Dry natural frequencies of the LCS for vertical flexural vibrations.

Mode no.	TDFlex-T (Hz)	Rajendran and Guedes Soares [33] (Hz)	Difference (%)
1	0.625	0.64	−2.343
2	1.603	1.64	−2.256
3	3.086	3.11	−0.772

Table 5: Dry natural frequencies of the ULCS for vertical flexural vibrations.

Mode no.	TDFlex-T (Hz)	Rajendran et al. [59] (Hz)	Difference (%)
3	0.717	0.72	−0.416
4	1.864	1.89	−1.37
5	3.527	3.64	−3.10

4.3. The Influence of Ship Length. VSF values for the ULC decrease rapidly at around $\omega\sqrt{L/g} = 2$ and then increase (see Figure 14). This could be attributed to the influence of resonance phenomena. On the other hand, the VSF values for the S175 hull decrease slowly and do not show any secondary peak in the response (see Figures 14–16). This nature of the transfer function of the VSF values for the S175 hull is similar to the rigid body case. It may therefore be concluded that hydroelasticity effects may be more prominent for more slender vessels.

4.4. The Influence of Structural Flexibility on Hydrodynamic Pressure Distributions. The influence of flexibility on local pressure variation was evaluated at the free surface and the hull bottom in way of the bow, stern, and amidships for $F_n = 0.25$ and $\lambda/L = 1$ (see Figure 17). This is because these conditions were shown to be critical in terms of flexible fluid structure interactions (see Section 4).

The variations of nondimensional hydrodynamic pressures over time are shown in Figures 18–20. Figures 18(a)

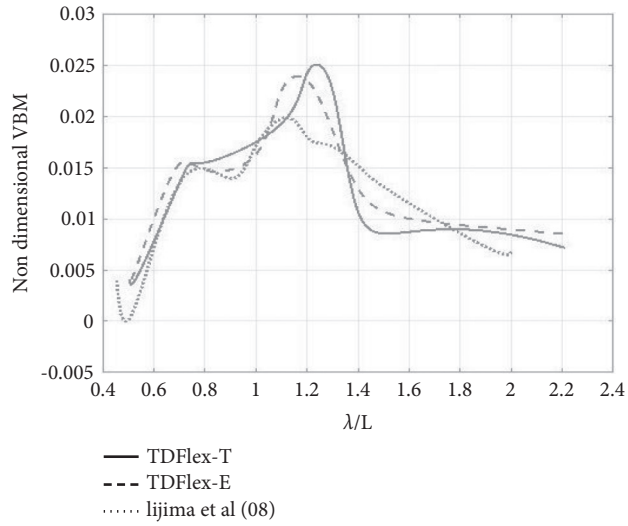

Figure 6: VBM transfer function at midship of S175 (F_n = 0.25).

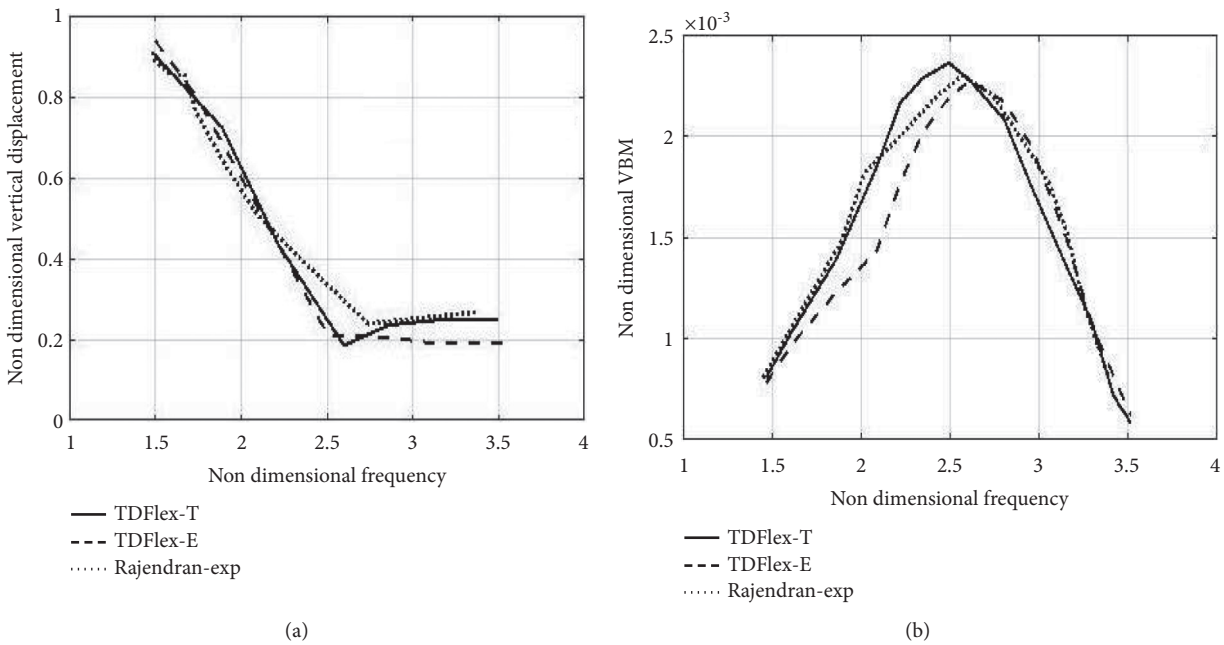

Figure 7: Symmetric responses, LC (at $F_n = 0$). (a) Vertical displacement. (b) VBM.

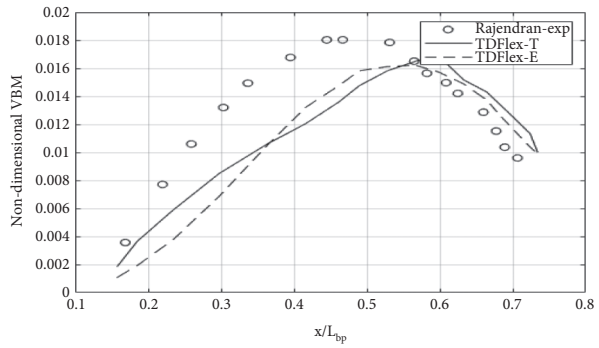

Figure 8: VBMs along the length for LC (F_n = 0.12 and λ/L = 1.06).

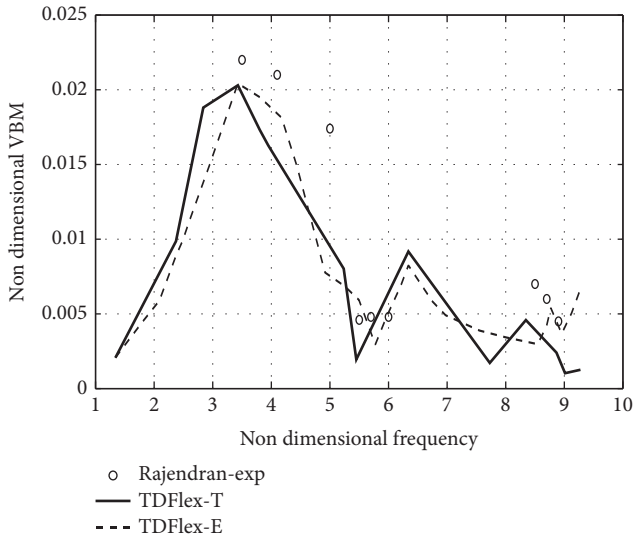

Figure 9: Comparison of rigid body and hydroelastic RAO of vertical deflection for the ULC at L/4.

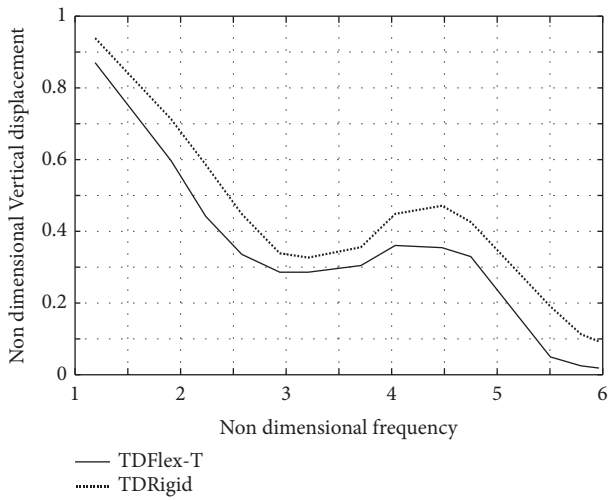

Figure 10: RAOs for vertical displacement for flexible body and rigid body, ULC.

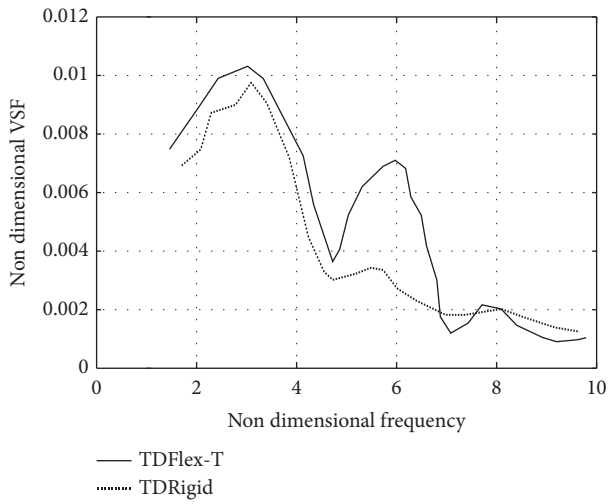

Figure 11: Comparison of rigid body and hydroelastic RAO of VSF for the ULC at L/4.

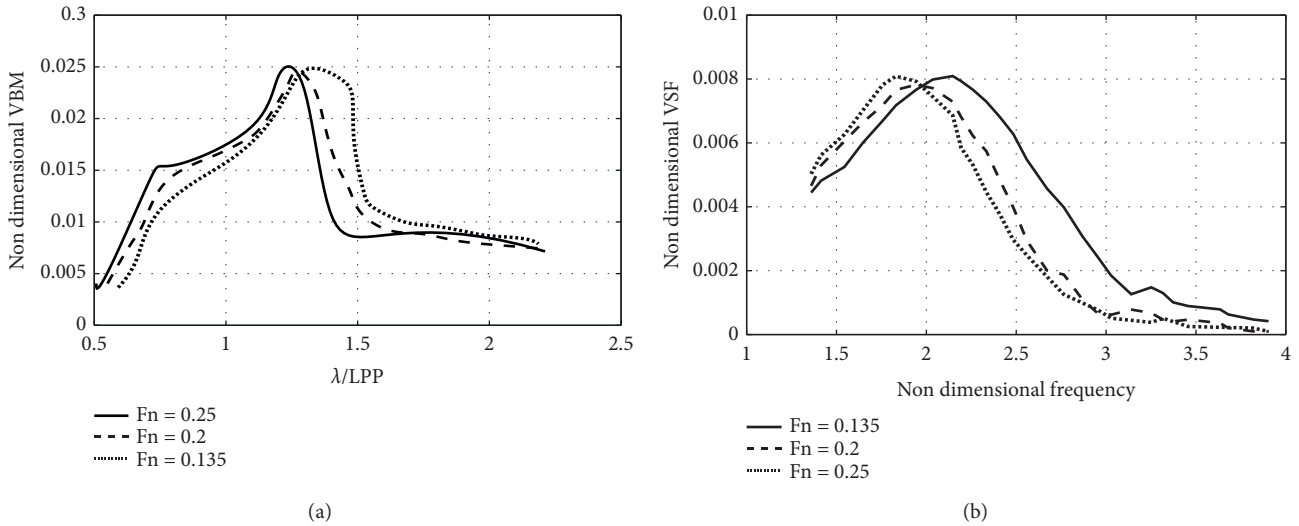

Figure 12: (a) Transfer function for VBM at amidships for different forward speeds of S175. (b) Transfer function for VSF at amidships for different forward speeds of S175.

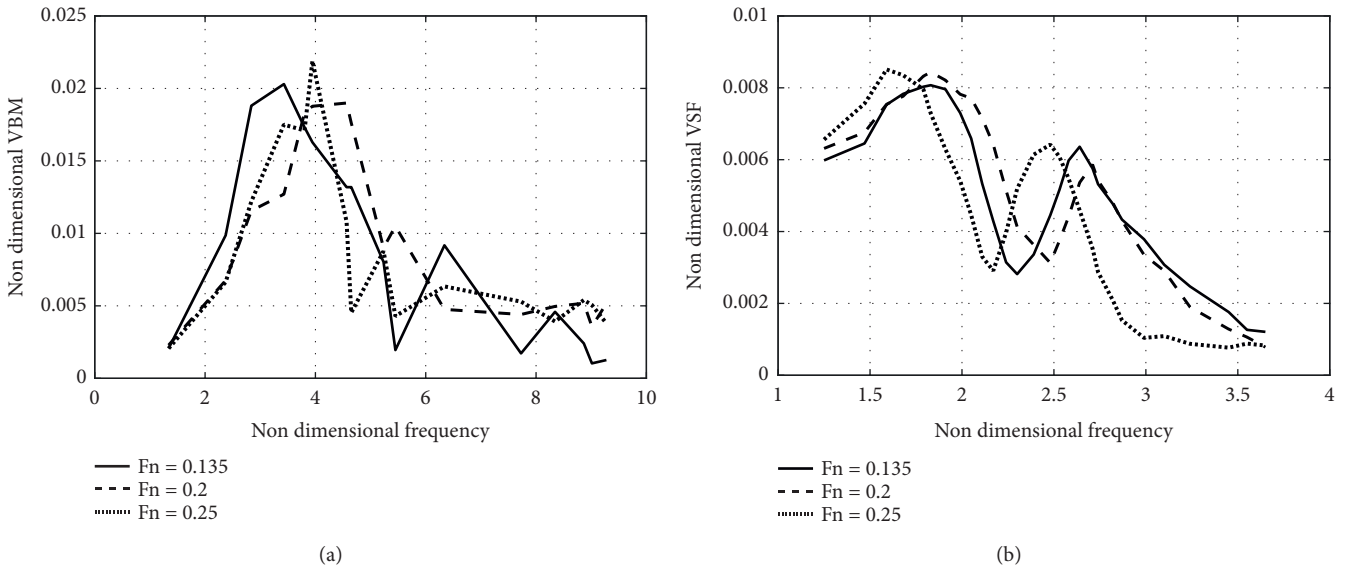

Figure 13: (a) Transfer function for VBM at amidships for different forward speeds of ULC. (b) Transfer function for VSF at amidships for different forward speeds of ULC.

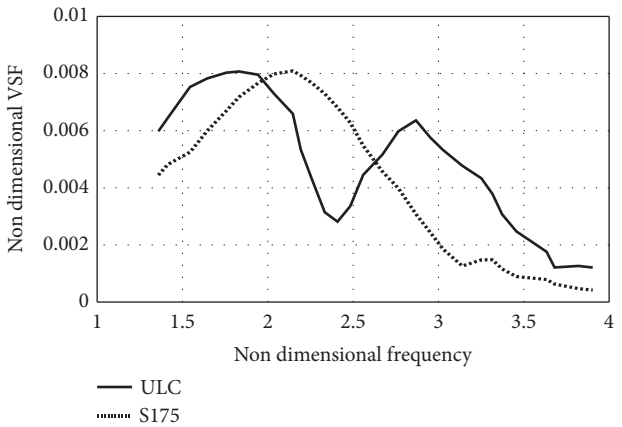

Figure 14: Shear force RAO comparison between S175 and the ULC ($F_n = 0.135$).

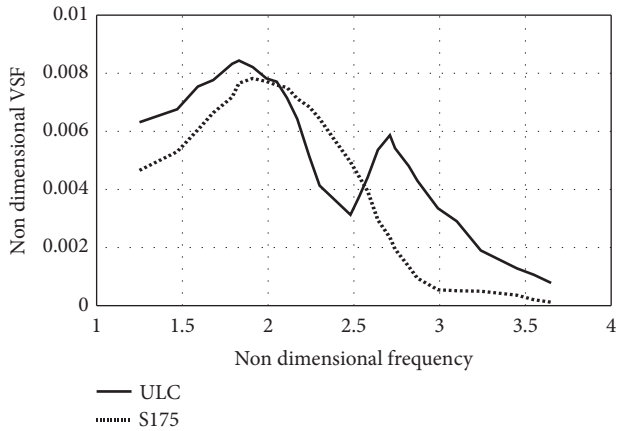

Figure 15: Shear force RAO comparison between S175 and the ULC ($F_n = 0.2$).

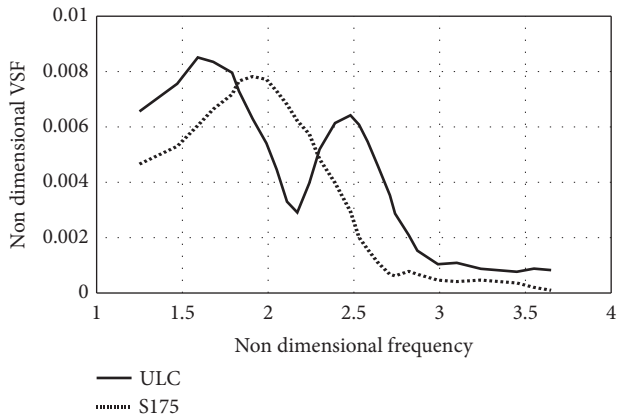

Figure 16: Shear force RAO comparison between S175 and the ULC ($F_n = 0.25$).

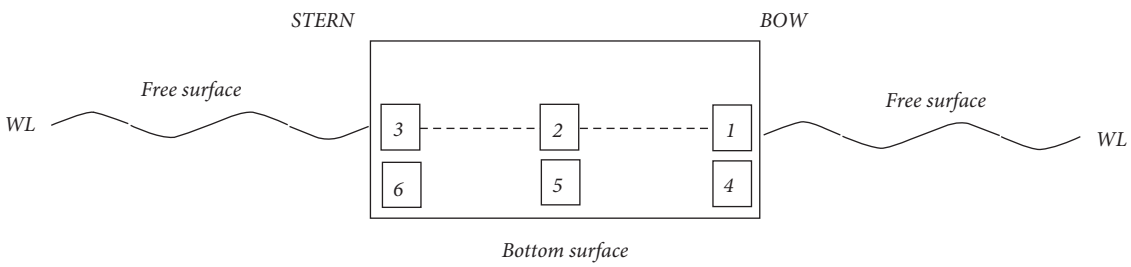

Figure 17: Schematic diagram of selection of panels (squares 1–3 highlight free surface locations; 4–6 highlight ship bottom locations).

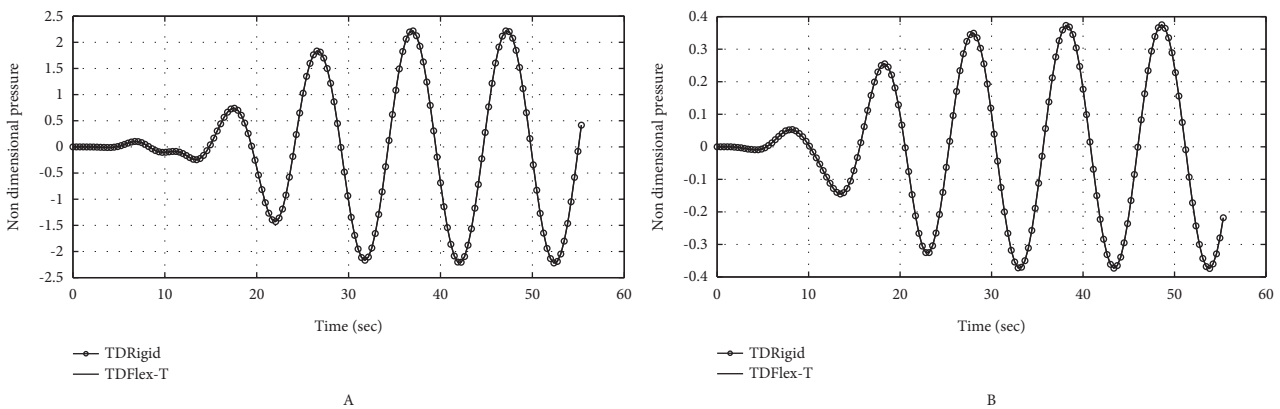

(a)

Figure 18: Continued.

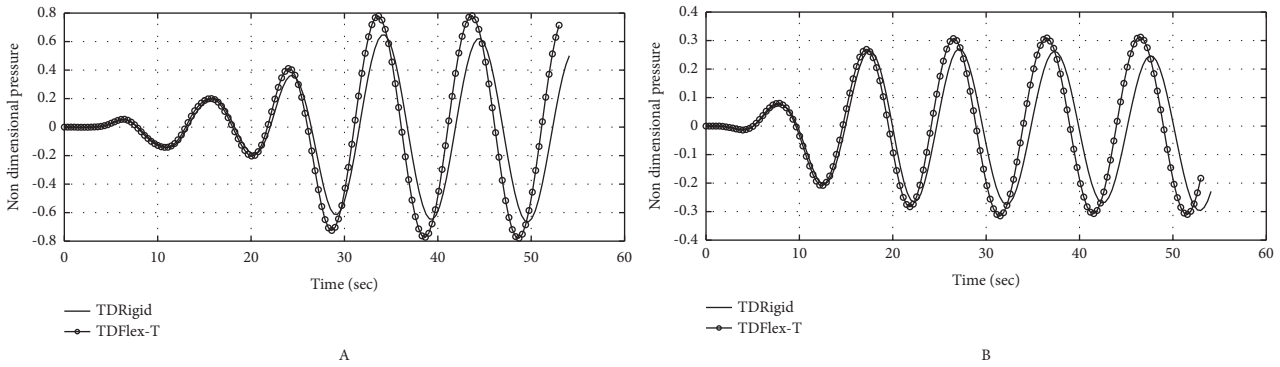

(b)

Figure 18: (a) Pressure time history of S175 hull at bow region, $F_n = 0.25$, $\lambda/L = 1$. (A) Pressure on free surface (see Figure 17; location point 1). (B) Pressure on bottom surface (see Figure 17; location point 4). (b) Pressure time history of ULC at bow region, $F_n = 0.25$, $\lambda/L = 1$. (A) Pressure at free surface (Figure 17; location point 1). (B) Pressure at bottom surface (Figure 17; location point 4).

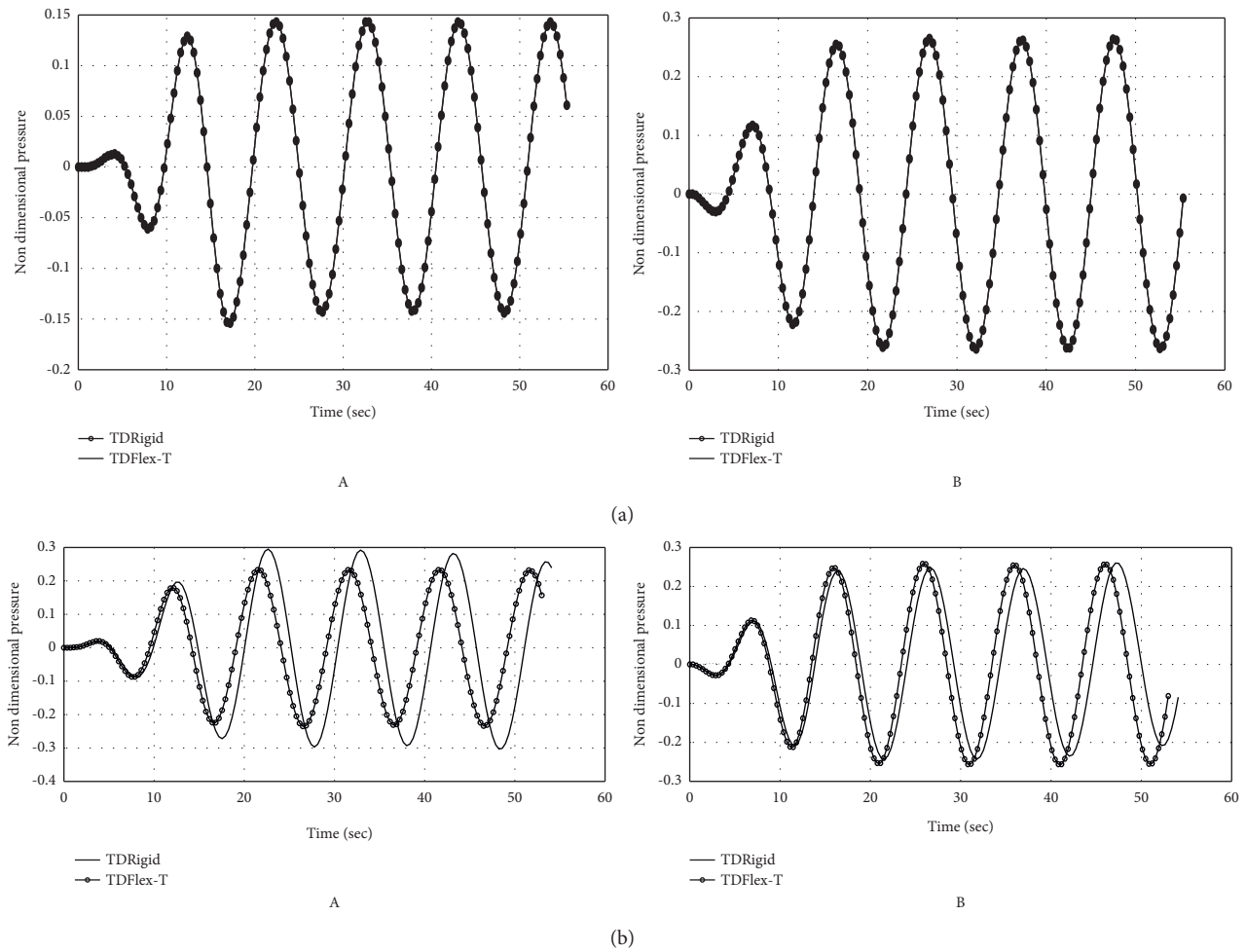

(a)

(b)

Figure 19: (a) Pressure time history of S175 hull at midship region, $F_n = 0.25$, $\lambda/L = 1$. (A) Pressure at free surface (Figure 17; location point 2). (B) Pressure at bottom surface (Figure 17; location point 5). (b) Pressure time history of ULC at midship region, $F_n = 0.25$, $\lambda/L = 1$. (A) Pressure at free surface (Figure 17; location point 2). (B) Pressure at bottom surface (Figure 17; location point 5).

and 18(b) display the pressure time histories in way of the bow region of both ships (Figure 17; location points 1 and 4). It is shown that the influence of flexibility is significant only for the ULC container ship model. This trend is confirmed by the comparisons shown in Figures 19(a), 19(b), 20(a), 20(b), respectively, corresponding to responses in way of

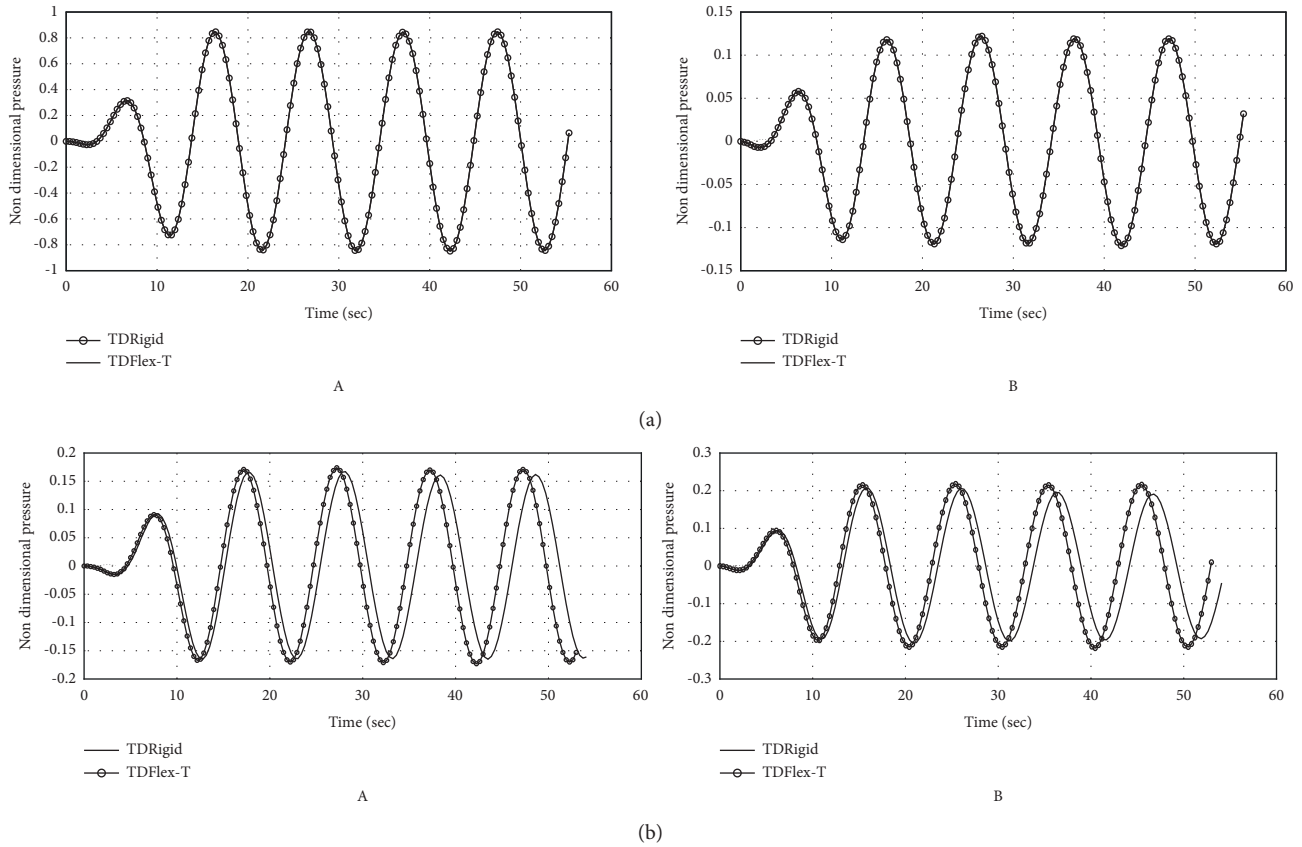

Figure 20: (a) Pressure time history of S175 hull at stern region, $F_n = 0.25$, $\lambda/L = 1$. (A) Pressure at free surface (Figure 17; location point 3). (B) Pressure at bottom surface (Figure 17, location point 6). (b) Pressure time history of S175 hull at stern region, $F_n = 0.25$, $\lambda/L = 1$. (A) Pressure at free surface (Figure 17; location point 3). (B) Pressure at bottom surface (Figure 17; location point 6).

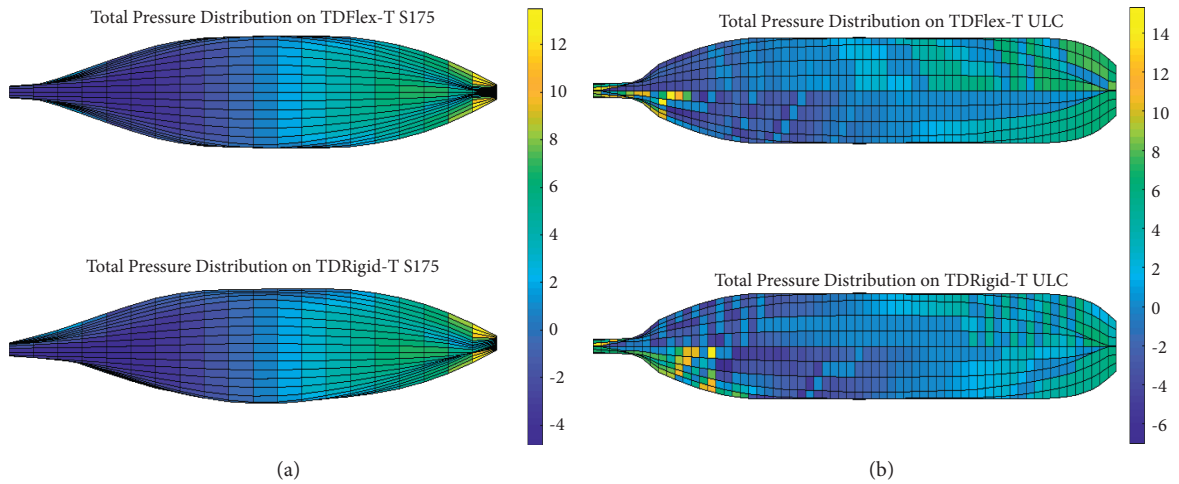

Figure 21: (a) Contour plot of pressure profile for a particular instant of time of S175 ship, $F_n = 0.25$, $\lambda/L = 1$. (b) Contour plot of pressure profile for a particular instant of time of ULC, $F_n = 0.25$, $\lambda/L = 1$.

amidships (see Figure 17; location points 2 and 5) and astern (see Figure 17; location points 3 and 6). The variation of the pressure along the ship hull for a particular time instant is depicted in Figures 21(a) and 21(b). The same plots display that the pressure variation is more visible for the case of ULC. It may be therefore concluded that as the ship length increases, the influence of hull flexibility on hydrodynamic pressures becomes prominent.

5. Conclusions

This paper presented a direct hydroelastic analysis method that combines a time-domain Green function with Timoshenko beam structural dynamics for the prediction of symmetric ship responses in waves. The hydrodynamic model is based on the linear 3D time-domain panel method where the Timoshenko beam model is adopted for the structural solution. Results were validated by comparisons against a range of available experimental data. A parametric study for three different containership hull forms demonstrated that hull slenderness and forward speed may influence symmetric flexible ship responses. Future research will focus on developing a fully nonlinear hydroelastic method for the prediction of extreme sea loads (e.g., slamming, green water on decks, and so on) on hull forms of low rigidity progressing at a medium to high speed in irregular waves.

Nomenclature

English symbols

A: Wave amplitude (m)
E: Young's modulus (N/m^2)
I: Moment of inertia (kg-m^2)
F_n: Froude number
f: Sectional load (N/m)
G: Shear modulus (N/m^2)
$G(x_s y_s z_s)$: Ship centre of gravity
g: Acceleration of gravity (m/sec^2)
K_{ij}: Global stiffness factor
k_s: Shear correction factor
L: Hull length (m)
M: Vertical bending moment (N-m)
$Oxyz$: Vessel Earth fixed coordinate system in way of the centre of gravity
p: Field point
q: Source point
S_0: Mean wetted surface
T: Time period (sec)
t: Time (sec)
U: Forward speed (m/s)
V: Vertical shear force (N)
w: Transverse deflection (m)
x_3: Vertical displacement (m)

Greek symbols

α^b, β^s: Residual weight functions
λ: Wavelength (m)
ρ: Structural density (kg/m^3)
ρ_o: Water density (kg/m^3)
ψ: Bending rotation (rad)
ω: Wave frequency (Hz).

Data Availability

The data supporting this study are original results from computer codes developed by the authors. The comparisons against these data can be found in the open scientific literature, and these comparisons are well justified.

Conflicts of Interest

The authors declare that they have no conflicts of interest.

References

[1] K. H. Shin, J. W. Jo, S. E. Hirdaris et al., "Two- and three-dimensional springing analysis of a 16,000 TEU container ship in regular waves," *Ships and Offshore Structures*, vol. 10, no. 5, pp. 498–509, 2015.

[2] S. E. Hirdaris, N. J. White, N. Angoshtari, M. C. Johnson, Y. Lee, and N. Bakkers, "Wave loads and flexible fluid-structure interactions: current developments and future directions," *Ships and Offshore Structures*, vol. 5, no. 4, pp. 307–325, 2010.

[3] S. E. Hirdaris, W. Bai, D. Dessi et al., "Loads for use in the design of ships and offshore structures," *Ocean Engineering*, vol. 78, pp. 131–174, 2014.

[4] Y. Lee, Z. Wang, WhiteN, and S. Hirdaris, *Time Domain Analysis of Springing and Whipping Response Acting on a Large Container Ship, ASME 2011 30th International Conference on Ocean, Offshore and Arctic Engineering OMAE2011-49218*, Rotterdam, The Netherlands, 2011.

[5] R. E. D. Bishop and W. G. Price, *Hydroelasticity of Ships*, Cambridge University Press, Cambridge, United Kingdom, 1979.

[6] R. E. D. Bishop, W. G. Price, and Y. Wu, "A general linear hydroelasticity theory of floating structures moving in a seaway, Philosophical Transactions of the Royal Society of London. Series A," *Mathematical and Physical Sciences*, vol. 316, pp. 375–426, 1986.

[7] S. E. Hirdaris, W. G. Price, and P. Temarel, "Two-and three-dimensional hydroelastic modelling of a bulker in regular waves," *Marine Structures*, vol. 16, no. 8, pp. 627–658, 2003.

[8] S. Malenica, B. Molin, and I. Senjanociv, "Hydroelastic response of a barge to impulsive and non-impulsive wave loads," in *Proceedings of the 3rd International Conference on Hydroelasticity in Marine Technology*, Oxford, United Kingdom, 15th - 17th September 2003.

[9] S. Malenica, I. Senjanovic, and S. Tomasevic, *An Efficient Hydroelastic Model for Wave Induced Coupled Torsional and Horizontal Ship Vibrations*, IWWWFB, Loughborough, UK, 2006.

[10] S. E. Hirdaris, *Hydroelastic Modelling: Prediction of Wave Loads on Bulk Carriers*, VDM Verlag Dr. Müller, Saarbrucken, Germany, 2009.

[11] R. D. Harding, S. E. Hirdaris, S. H. Miao, M. Pittilo, and P. Temarel, "Use of hydroelasticity analysis in design," in *Proceedings of the 4th International Conference on Hydroelasticity in Marine Technology*, pp. 1–12, National Defense Industry Press, Wuxi, China, 10 – 14 September 2006.

[12] P. Temarel and S. E. Hirdaris, Eds., *Hydroelasticity 2009: Hydroelasticity in Marine Technology*, p. 405pp, University of Southampton, Southampton, UK, 2009.

[13] S. E. Hirdaris and P. Temarel, "Hydroelasticity of ships: recent advances and future trends," *Proceedings of the Institution of Mechanical Engineers - Part M: Journal of Engineering for the Maritime Environment*, vol. 223, no. 3, pp. 305–330, 2009.

[14] I. Senjanović, N. Vladimir, M. Tomić, N. Hadzic, and Š Malenica, "Global hydroelastic analysis of ultra large container ships by improved beam structural model," *International J on Nav. Archit. Ocean Engineering*, vol. 6, pp. 1041–1063, 2014.

[15] O. Belik, R. Bishop, and W. Price, "A simulation of ship responses due to slamming in irregular head waves," *Trans. of RINA*, vol. 125, pp. 237–253, 1983.

[16] R. Bishop, J. D. Clarke, and W. G. Price, "Comparison of full scale and predicted responses of two frigates in severe weather trial," *Trans. RINA*, vol. 126, pp. 123–166, 1984.

[17] C. Guedes Soares, "Transient response of ship hulls to wave impact," *International Shipbuilding Progress*, vol. 36, pp. 137–156, 1989.

[18] M. K. Wu and O. A. Hermundstad, "Time domain simulation of wave-induced nonlinear motions and loads and its applications in ship design," *Marine Structures*, vol. 15, pp. 561–597, 2002.

[19] P. A. K. Lakshmynarayanana and S. Hirdaris, "Comparison of nonlinear one- and two-way FFSI methods for the prediction of the symmetric response of a containership in waves," *Ocean Engineering*, vol. 203, Article ID 107179, 2020.

[20] J. Jiao, S. Huang, and C. G. Soares, "Viscous fluid–flexible structure interaction analysis on ship springing and whipping responses in regular waves," *Journal of Fluids and Structures*, vol. 106, Article ID 103354, 2021.

[21] T. Hamamoto, A. Suzuki, N. Tsujioka, and K.-i. Fujita, "3D BEM-FEM hybrid hydroelastic analysis of module linked large floating structures subjected to regular waves," in *The Eighth International Offshore and Polar Engineering Conference*International Society of Offshore and Polar Engineers, Montreal, Quebec, Canada, 1998.

[22] X. D. Liu and S. Sakai, "Time domain analysis on the dynamic response of a flexible floating structure to waves," *J. Eng. Mechanics-Asce*, vol. 128, no. 1, pp. 48–56, 2002.

[23] J. H. Kyoung, S. Y. Hong, and B. W. Kim, "FEM for time domain analysis of hydroelastic response of VLFS with fully nonlinear free-surface conditions," *International Journal of Offshore and Polar Engineering*, vol. 16, no. 3, pp. 168–174, 2006.

[24] Q. C. Liuchao and L. Hua, "Three-dimensional time-domain analysis of very large floating structures subjected to unsteady external loading," *J. Offshore Mech. Arct. Eng. Trans. Asme*, vol. 129, no. 1, pp. 21–28, 2007.

[25] J. H. Kim and Y. Kim, "Numerical analysis on springing and whipping using fully-coupled FSI models," *Ocean Engineering*, vol. 91, pp. 28–50, 2014.

[26] Y. Kim, K. H. Kim, and Y. Kim, "Analysis of hydroelasticity of floating ship like structure in time domain using a fully coupled hybrid BEM-FEM," *Journal of Ship Research*, vol. 53, no. 1, pp. 31–47, 2009a.

[27] Y. Kim, K. H. Kim, and Y. Kim, "Springing analysis of a seagoing vessel using fully coupled BEM-FEM in the time domain," *Ocean Engineering*, vol. 36, no. 11, pp. 785–796, 2009b.

[28] Y. Kim, K. H. Kim, and Y. Kim, "Time domain springing analysis on a floating barge under oblique wave," *Journal of Marine Science and Technology*, vol. 14, no. 4, pp. 451–468, 2009c.

[29] J. H. Kim, Y. Kim, R. H. Yuck, and D. Y. Lee, "Comparison of slamming and whipping loads by fully coupled hydroelastic analysis and experimental measurement," *Journal of Fluids and Structures*, vol. 52, pp. 145–165, 2015.

[30] K. H. Kim and Y. Kim, "Springing analysis of a seagoing vessel using fully coupled BEM–FEM in the time domain," *Ocean Engineering*, vol. 36, pp. 785–796, 2009.

[31] F. Kara, "Time domain prediction of hydroelasticity of floating bodies," *Applied Ocean Research*, vol. 51, pp. 1–3, 2015.

[32] H. Y. Kang and M. H. Kim, "Time-domain hydroelastic analysis with efficient load estimation for random waves," *International Journal of Naval Architecture and Ocean Engineering*, vol. 9, no. 3, pp. 266–281, 2017.

[33] S. Rajendran and C. Guedes Soares, "Numerical investigation of the vertical response of a containership in large amplitude waves," *Ocean Engineering*, vol. 123, pp. 440–451, 2016.

[34] D. H. Lee and H. S. Choi, "Transient hydroelastic response of very large floating structures by FE-BE hybrid method," in *Proceedings of the The Thirteenth International Offshore and Polar Engineering Conference*, Honolulu, Hawaii, USA, 2003.

[35] M. Kashiwagi, "A B-spline Galerkin scheme for calculating the hydroelastic response of a very large floating structure in waves," *Journal of Marine Science and Technology*, vol. 3, no. 1, p. 37e49, 1998a.

[36] M. Kashiwagi, "A direct method versus a mode-expansion method for calculating hydroelastic response of a VLFS in waves," in *Proceedings of the The Eighth International Offshore and Polar Engineering Conference*, Montreal, Quebec, Canada, 1998b.

[37] R. Taghipour, T. Perez, and T. Moan, "Time-domain hydroelastic analysis of a flexible marine structure using state-space models," *Journal of Offshore Mechanics and Arctic Engineering*, vol. 131, no. 1, 2009.

[38] J. Jiao, H. Yu, C. Chen, and H. Ren, "Time domain numerical and segmented model experimental study on ship hydroelastic responses and whipping loads in harsh irregular seaways," *Ocean Engineering*, vol. 185, pp. 59–81, 2019.

[39] J. Jiao, Z. Chen, C. Chen, and H. Ren, "Time domain hydroelastic analysis of nonlinear motions and loads on a large bow-flare ship advancing in high irregular seas," *Journal of Marine Science and Technology*, vol. 25, pp. 426–454, 2020.

[40] S. Pal, R. Datta, and M. R. Sunny, "Fully coupled time domain solution for hydroelastic analysis of floating boy," *Ocean Engineering*, vol. 153, pp. 173–184, 2018.

[41] R. Datta and C. Guedes Soares, "Analysis of the hydroelastic effect on a container vessel using coupled BEM–FEM method in the time domain," *Ships and Offshore Structures*, vol. 15, no. 4, pp. 393–402, 2020.

[42] Y. Lee, N. White, Z. Wang, S. Zhang, and S. Hirdaris, "Comparison of springing and whipping responses of model tests with predicted nonlinear hydroelastic analyses," *International Journal of Offshore and Polar Engineering*, vol. 22, no. 3, p. 209, 2012.

[43] J. H. Kim, Y. Kim, and A. Korobkin, "Comparison of fully coupled hydroelastic computation and segmented model test results for slamming and whipping loads," *Int. J. Naval Architect. Ocean Eng.*vol. 6, pp. 1064–1081, 2014.

[44] K. H. Kim, B. W. Kim, and S. Y. Hong, "Experimental investigations on extreme bow-flare slamming loads of 10,000-TEU containership," *Ocean Engineering*, vol. 171, pp. 225–240, 2018.

[45] J. L. Jiao, H. L. Ren, and C. H. Chen, "Model testing for ship hydroelasticity: a review and future trends," *Journal of Shanghai Jiao Tong University*, vol. 22, pp. 641–650, 2017.

[46] S. E. Hirdaris, Y. Lee, G. Mortola et al., "The influence of nonlinearities on the symmetric hydrodynamic response of a 10,000 TEU container ship," *Ocean Engineering*, vol. 111, pp. 166–178, 2016.

[47] P. Yang, W. Zhang, X. Wang et al., "Uncertainty analysis of hydroelastic responses and wave loads for different structural modeling and potential methods," *Ocean Engineering*, vol. 222, Article ID 108529, 2021.

[48] R. Datta and D. Sen, "The simulation of ship motion using a B-spline based panel method in time domain," *Journal of Ship Research*, vol. 51, no. 3, pp. 267–284, 2007.

[49] N. M. Newmark, "A method of computation for structural dynamics," *Journal of Engineering Mechanics Division, Proceedings of the American Society of Civil Engineers*, vol. 85, no. 3, pp. 67–94, 1959.

[50] N. Datta and M. A. Siddiqui, "Hydroelastic analysis of axially loaded Timoshenko beams with intermediate end fixities under hydrodynamic slamming loads," *Ocean Engineering*, vol. 127, pp. 124–134, 2016.

[51] S. E. Hirdaris and A. W. Lees, "A conforming unified finite element formulation for the vibration of thick beams and frames," *International Journal for Numerical Methods in Engineering*, vol. 62, pp. 579–599, 2005.

[52] J. Rakowski, "The interpretation of the shear locking in beam elements," *Computers & Structures*, vol. 37, no. 5, pp. 769–776, 1990.

[53] M. Liu and D. G. Gorman, "Formulation of Rayleigh damping and its extensions," *Computers & Structures*, vol. 57, pp. 277–285, 1995.

[54] Y. Liu, Z. Liu, Q. Song, and B. Wang, "Development of constrained layer damping toolholder to improve chatter stability in end milling," *International Journal of Mechanical Sciences*, vol. 117, pp. 299–308, 2016.

[55] W. M. Lin and D. Yue, "Numerical Solution for large amplitude motions in the time domain," in *Proceedings of the 18th ONR Symposium on Naval Hydrodynamics*, pp. 41–66, National Academy Press, Washington DC, 1990.

[56] A. Cabada, L. López-Somoza, and M. Yousfi, "Green's function related to a n^{th} order linear differential equation coupled to arbitrary linear non-local boundary conditions," *Mathematics*, vol. 9, no. 16, p. 1948, 2021.

[57] J. P. Boin, M. Guilbaud, and M. Ba, *Seakeeping Computations Using the Ship Motion Green Function*, pp. 398–405, ISOPE, Seattle, 2000.

[58] I. Drummen and M. Holtmann, "Benchmark study of slamming and whipping," *Ocean Engineering*, vol. 86, pp. 3–10, 2014.

[59] S. Rajendran, N. Fonseca, and C. Guedes Soares, "A numerical investigation of the flexible vertical response of an ultra large containership in high seas compared with experiments," *Ocean Engineering*, vol. 122, pp. 293–310, 2016.

[60] D. Sengupta, S. K. Pal, and R. Datta, "Hydroelasticity of a 3D floating body using a semi analytic approach in time domain," *Journal of Fluids and Structures*, vol. 71, pp. 96–115, 2017.

[61] K. Iijima, T. Yao, and T. Moan, "Structural response of a ship in severe seas considering global hydroelastic vibrations," *Marine Structures*, vol. 21, no. 4, pp. 420–445, 2008.

Hindawi
Shock and Vibration
Volume 2022, Article ID 9764478, 19 pages
https://doi.org/10.1155/2022/9764478

Research Article

Estimation of Directional Wave Spectrum Using Measurement Array Pressure Data on Bottom-Mounted Offshore Structure in Incident and Diffracted Wave Field

Xiaodong Song,[1,2] Zilong Ti ,[1] and Yuanzhou Zhou[1]

[1]*Department of Bridge Engineering, Southwest Jiaotong University, Chengdu 610031, China*
[2]*China Railway Eryuan Engineering Group Co. Ltd, Chengdu, China*

Correspondence should be addressed to Zilong Ti; swjtutzl@126.com

Received 24 November 2021; Revised 16 December 2021; Accepted 5 January 2022; Published 27 February 2022

Academic Editor: Jialong Jiao

Copyright © 2022 Xiaodong Song et al. This is an open access article distributed under the Creative Commons Attribution License, which permits unrestricted use, distribution, and reproduction in any medium, provided the original work is properly cited.

Determination of the directional wave spectrum which offshore structures actually encounter is essential for multiple applications including wave-induced load and vibration evaluation, and hence becomes a fundamental task in ocean engineering. Due to the wave diffraction effect, wave field around an offshore structure is the mixture of incident wave components and diffracted wave components. Estimating directional wave spectrum in diffracted wave field significantly differs from the occasion in undisturbed waves since the amplitude and phase relationship between the incident and diffracted waves are coupled, and therefore making the conventional approach not applicable. In this study, the diffraction wave theory is introduced into the estimation of directional wave spectrum to consider the effect of diffracted waves using array pressure data from existing pressure gauges on structures. Considering the performance of the presented approach under scenarios with various gauge arrays, different directions, and spreading coefficients, multiple levels of background noise are evaluated and discussed, respectively. The presented approach is also deployed into an in-situ measurement application on a marine structure and compared with wave observation data to test its feasibility in engineering practice. In general, the presented approach can reasonably estimate the directional wave spectrum and show advantages over the conventional approach in which the diffraction effect is excluded.

1. Introduction

The three-dimensional wave spectrum, i.e., directional wave spectrum, providing the basic information including energy and direction distributions for stochastic waves, is one of the most fundamental properties in offshore engineering. Measurement and determination of the directional wave spectrum for the offshore structures is an engineering premise of multiple applications, including the evaluation of hydrodynamic loads [1], wave-induced vibration [2], etc., and hence becomes a primary task in the health monitoring and maintenance of offshore structures. Conventionally, estimation of directional wave spectrum is usually performed using measurement data collected by spatial array or pitch-and-roll buoys. However, after the structure is built in place, the local wave field is disturbed by the presence of structure due to the wave diffraction effect [3]. Wave diffraction refers to a particular phenomenon when propagating waves encounter obstacles, and the obstacle surface may, depending on the obstacle size, induce diffracted waves. Conventional methods using measurement data such as array wave elevations [4] or array wave pressures [5] to estimate the directional wave spectrum are based on the assumption that the wave field is an undisturbed condition, and therefore all wave components are independent and random. However, the disturbed wave field, containing the incident and diffracted wave components, brings challenges to the estimation of directional wave spectrum because the relationship between diffracted and incident waves is synchronized and coupled. Some previous studies [6–8] that investigated the disturbed wave field due to wave reflection effect in the laboratory shows that the disturbed wave components may impose significant deviations in the spectral density and direction results and hence the

conventional methods for undisturbed wave field are not applicable. Accurate estimation of the actually encountering directional wave spectrum for offshore structures in the incident and diffracted wave field could benefit the scientific and engineering practice including real-time load evaluation [9], structural monitoring [10], motion control, etc., and therefore, is essential to study. However, limited literature focuses on this issue and still lacks in-depth investigation.

Wave spectra are usually present in either two-dimension or three-dimension forms. A two-dimension wave spectrum only contains energy distribution in the frequency domain and is easily estimated by using measurement data from single-point gauges. Stochastic waves have an inherent nature of multidirections. A three-dimension wave spectrum could provide energy and directional distributions while it is usually more difficult to obtain. In order to capture the directional information in stochastic waves, researchers spend efforts on improving both measurement techniques [11, 12] and estimation methods [5, 13]. In general, two mainstream approaches exist to obtain the directional wave spectrum. One way is to deploy single-point devices such as multifunctional buoys, which can collect velocity, pressure, motion data, and use various algorithms to analyze the cross-spectral relationship between them to approximate the directional wave spectrum [14]. This approach is direct and convenient, but the withdraws are also obvious that the costs on the devices and installation are usually considerable. Furthermore, these single-point devices still lack the ability to separate the incident wave components from the disturbed wave field due to insufficient information on multiple locations. Another way is to use multiple array gauges, e.g., array wave gauges and array pressure gauges, to synchronously record data and estimate the directional wave pressure by analyzing the cross-spectral information between them [5, 6]. While less convenient compared with the first approach, this way is easier to implement and widely used by researchers. Studies [6, 15] show that by utilizing appropriate modifications, this technique also has the ability to separate reflected wave components in disturbed wave fields and gives appreciable estimated results. Another advantage of using array gauge measurement is that in present time, the array gauges are usually a part of structural health monitoring (SHM) system, such as pressure gauges embedded on structures to observe the hydrodynamic load and hence there is no need to spend additional efforts and expense on devices and their installation. In light of this statement, this study focuses on utilizing array pressure data from existing pressure gauges embedded on structures to estimate the directional wave spectra.

Various methods are proposed to estimate the directional spectrum from array measurement data. A pioneering attempt was presented in the literature [13] by using Direct Fourier Transform method to analyze the spectral information and give a direct approximation of the incident wave spectrum. Howell and Gary [5] invented a measurement equipment by embedding six pressure gauges on a hexagonal frame to simultaneously measure wave pressure and make estimations from array pressure data. To make the estimation more robust, MLM (Maximum Likelihood Method) [16] and parametric method [17] were proposed and aimed to improve the overall accuracy in the final guess of the spectra from cross-spectral results. Literature [18] investigated the directional spectra using a eight-wave-probe array and presented the computational routine and preliminary validation. To sum up, the studies above only consider the estimation in the undisturbed wave field. Literature [6, 7] pointed out that influenced by reflected or refracted waves, the wave field may contain different wave components and the standard method cannot separate these phase-related components and therefore causes errors in spectrum estimation. Isobe [15] proposed a modified MLM method to consider the reflected waves from vertical walls by adding a phase-related term in the governing equations for spectrum estimation. Later, based on this study, some researchers [7, 19] further isolated the reflected components and used the approach to determinate the reflection coefficients. Study [20] proposed a new method to isolate incident and reflected spectra using a gauge array in a multidirectional wave basin. This series of studies indicate that separating the wave components in disturbed wave field is essential in spectrum estimation and provide a basic methodology for a relative problem. Another practical mainstream for spectra estimation is to build the relationship between the incident wave and global structural responses [21–23]. However, regarding estimating the direction wave spectrum of wave field with the incident and diffracted waves around offshore structures, until now, there is very limited literature addressing this issue and lacks useful solutions.

In the present study, the diffraction wave theory is introduced into the estimation of directional wave spectrum to consider the effect of diffracted waves using array pressure data from existing pressure gauges on structures. Two numerical experiments are conducted as proof-of-concept studies to test and evaluate the feasibility of the presented approach under various structures and wave scenarios. The performance of presented approach using various gauge arrays, different wave directions and spreading coefficients and multiple levels of background noise are evaluated and discussed, respectively. The presented approach is also deployed into an in-situ measurement application and compared with wave observation data to test its validity in engineering practice. In the end, some main conclusions associated with limitations and further works regarding the presented approach are drawn.

2. Methodology

2.1. Fundamentals. Stochastic waves are usually presented as a sum of infinite cosine waves and the stochastic wave surface elevation η at location coordinate $\boldsymbol{x}$ can be written in the form of spectral presentation:

$$\eta(x,t) = \int_{\sigma}\int_{\overrightarrow{k}} e^{i(\overrightarrow{k}x-\omega t)} Z(d\overrightarrow{k}, d\omega), \tag{1}$$

where k is the wave number vector and ω is the wave frequency. $Z(d\overrightarrow{k}, d\sigma)$ denotes the wave energy within the wave

number range of $[\vec{k}, \vec{k} + d\vec{k}]$ and wave frequency range of $[\omega, \omega + d\omega]$ and is a complex number of which absolute value is the wave amplitude and argument is the wave phase. The cross-energy wave spectrum Φ_{mn} at location coordinate $\vec{x}_m$ $\vec{x}_n$ can be expressed as the Fourier transform of the product between wave components as follows:

$$\Phi_{mn} = \int_0^{2\pi} e^{-i\vec{k}(\vec{x}_m - \vec{x}_n)} E(\omega, \theta) d\theta, \tag{2}$$

where $E(\omega, \theta)$ denotes the directional wave spectrum. In order to separate the direction and energy information, the directional wave spectrum $E(\omega, \theta)$ is usually expressed as the product of spreading function $D(\omega, \theta)$ and spectral density $S(\omega)$ as follows:

$$\Phi_{mn} = S(\omega) \int_0^{2\pi} e^{-i\vec{k}(\vec{x}_m - \vec{x}_n)} D(\omega, \theta) d\theta. \tag{3}$$

The equation above describes the basic mathematical relationship between wave cross-spectrum, wave spectral density, and spreading function, which is the foundational formulation for spectrum estimation. Furthermore, if the given data is wave pressure instead of wave surface elevation, by inserting the relationship between wave pressure and surface elevation of Airy wave theory, the cross-energy wave pressure spectrum $\Phi_{mn,p}$ becomes as follows:

$$\Phi_{mn,p} = S(\omega) \int_0^{2\pi} \left\{ \rho g \frac{ch[\vec{k}(d+z)]}{ch(\vec{k}d)} \right\}^2 e^{-i\vec{k}(\vec{x}_m - \vec{x}_n)} D(\omega, \theta) d\theta. \tag{4}$$

Howell [5] uses (4) as the basic formulation to estimate the undisturbed incident wave field using array pressure gauges fixed on a hexagonal frame. The theories above have a tacit assumption that all the wave components are independent and random. However, when the wave field consists of both incident and diffracted waves, the relationship between the incident and diffracted components is determined and therefore, (4) is invalid and needs modification.

The incident wave pressure $p_i(x,t)$ of the stochastic wave series described in (1) reads as follows:

$$p_i(x,t) = \int_\omega \int_{\vec{k}} \rho g \frac{ch[\vec{k}(d+z)]}{ch(\vec{k}d)} e^{i(\vec{k}x - \omega t)} Z(d\vec{k}, d\omega). \tag{5}$$

Wave diffraction theory of the first order is introduced to mathematically describe the diffraction effect. According to wave diffraction theory [3], as demonstrated in Figure 1, the actual wave field around the structure (Figure 1(c)) is the superposition of the incident wave field (Figure 1(a)) and the diffracted wave field (Figure 1(b)). Therefore, the actual disturbed wave pressure on the structure is the combination of incident wave pressure and diffracted wave pressure which reads as follows:

$$p_i(x,t) + p_d(x,t) = \int_\omega \int_{\vec{k}} \rho g \frac{ch[\vec{k}(d+z)]}{ch(\vec{k}d)} e^{i(\vec{k}x - \omega t)} Z(d\vec{k}, d\omega) + \int_\sigma \int_{\vec{k}_d} \rho g \frac{ch\left[\vec{k}_d(d+z)\right]}{ch\left(\vec{k}_d d\right)} e^{i\left(\vec{k}_d x - \omega t\right)} Z\left(d\vec{k}_d, d\omega\right), \tag{6}$$

where the subscript i and d denote the incident and diffracted components. In principle, any signals related to waves, i.e., elevation, pressure, response, etc., may be utilized as the product of the incident component and a complex-valued transfer function. Therefore, by substituting (6) into (4), the cross-energy spectrum of wave pressure on the structure becomes as follows:

$$\Phi_{mn,p} = E(\omega) \int_0^{2\pi} H_m H_n^* e^{-i\vec{k}(\vec{x}_m - \vec{x}_n)} D(\omega, \theta) d\theta, \tag{7}$$

H is the complex-valued transfer function which reads as follows:

$$H(\vec{k}, \omega) = 1 + \frac{ch\left[\vec{k}_d(d+z)\right]}{ch\left(\vec{k}_d d\right)} e^{i\left(\vec{k}_d x - \omega t\right)} \frac{Z\left(d\vec{k}_d, d\omega\right)}{\left\{ch[\vec{k}(d+z)]/ch(\vec{k}d) e^{i(\vec{k}x - \omega t)} Z(d\vec{k}, d\omega)\right\}}. \tag{8}$$

A prior task in the calculation of (7) is the determination of the transfer function H. This transfer function, of which physical definition is the mapping from incident wave elevation to wave pressure on the structure, can be directly investigated by either analytical solutions for structures with regular geometry such as circular cylinders [3], or numerical approaches such as the boundary element method (BEM) [24]. The details in the determination of transfer function for specific structures will be described in the following sections.

By using (7) as the governing formulation and appropriate numerical method, the directional spectrum can be approximated by using a finite number of pressure data on the offshore structure.

2.2. Numerical Solution. Theoretically speaking, the calculation of directional spectrum using (7) requires pressure data at infinite locations around the structures, which is very

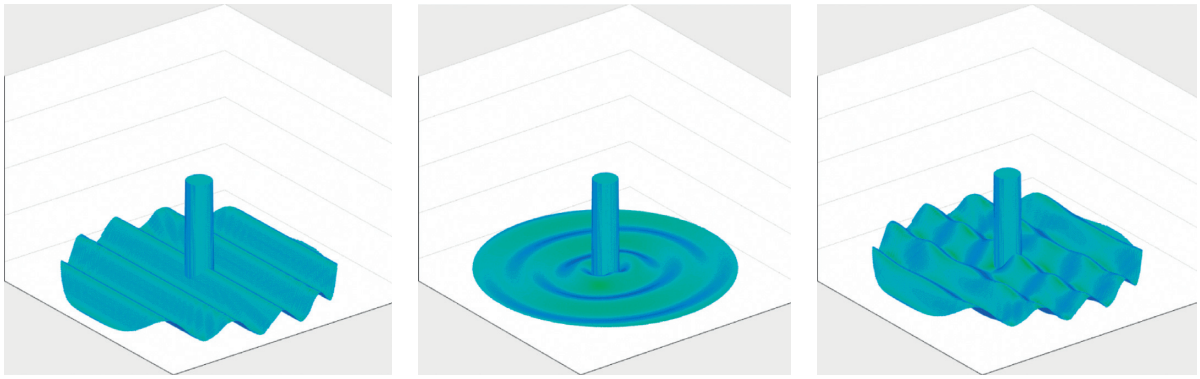

(a) (b) (c)

Figure 1: Wave field around a cylinder: (a) incident wave field; (b) diffracted wave field due to the presence of cylinder; (c) actual wave field around a cylinder as the superposition of (a) and (b).

difficult in practice. Researchers developed various numerical solutions to approximate the accurate spectra using data from an only a finite number of locations, such as Maximum Likelihood Method (MLM), Maximum Entropy Method (MEM) [25], and Bayesian approach (BDM) [4]. These methods may deviate in accuracy and have their specific requirements on array pattern, gauge quantity, etc. According to previous studies [4, 20], by employing a Bayesian approach to approximate the sample data by a most reasonable model, BDM can give the direction spectrum results with appreciable accuracy and has an inherent good ability to resist signal noise. Therefore, the Bayesian approach BDM is employed in this study. A brief description of using the Bayesian procedure to approximate the direction spectrum is introduced. In BDM, the basic formulation of the cross-energy spectrum is rewritten as follows:

$$\varphi_i = \int_0^{2\pi} H_i(\omega,\theta) G(\theta|\omega) d\theta, \quad (i = 1, 2, \ldots, N),$$
$$H_i(\omega,\theta) = H_m(\omega,\theta) H_n * (\omega,\theta) \frac{\left[\cos\left(kx_{mn}\cos\theta + ky_{mn}\sin\theta\right) - i\sin\left(kx_{mn}\cos\theta + ky_{mn}\sin\theta\right)\right]}{\sqrt{\varphi_{mm}(f)\varphi_{nn}(f)}}, \tag{9}$$
$$G(\theta|\omega) = \frac{S(\omega,\theta)}{S(\omega)} s,$$

where $N = M(M+1)/2$ and M is the number of wave signals. θ is the wave direction. Assuming the directional spreading function $G(\theta|\omega)$ is divided into K partitions and is approximated as follows:

$$G(\theta_k|\omega) = \sum_{k=1}^{K} \exp\left[x_k(\omega)\right] I_k(\theta), \quad (k = 1, 2, \ldots, K),$$
$$I_k(\theta) = \begin{cases} 1, & (k-1)\Delta\theta \le \theta \le k\Delta\theta \\ 0 \end{cases}. \tag{10}$$

Substituting (12) into (9), after some mathematical manipulations and inserting an error term ε_i, the cross-energy spectrum becomes as follows:

$$\varphi_i = \sum_{k=1}^{K} \alpha_{ik} \exp\left(x_k\right) + \varepsilon_i, \quad (i = 1, 2, \ldots, 2N). \tag{11}$$

The subscripts $i = 1$ to N and $N+1$ to 2N represent real parts and imaginary parts of the complex cross-energy spectrum φ_i and α_{ik}, respectively. The error term ε_i is assumed to have the probability of their occurrence expressed by the normal distribution having the mean value of 0 and the variance σ^2. The likelihood function of x_k and σ^2 is given by the following:

$$L\left(x_1, x_2, \ldots, x_k; \sigma^2\right) = \frac{1}{\left(2\pi\sigma^2\right)^N} \exp\left\{-\frac{1}{2\sigma^2} \sum_{i=1}^{2N} \left[\varphi_i - \sum_{k=1}^{K} \alpha_{ik} \exp\left(x_k\right)^2\right]\right\}. \tag{12}$$

With a basic assumption that the wave component is independent of each other in the frequency domain and the directional function is a continuous and smooth one, it yields a limiting condition of x_k which reads as follows:

$$x_k - 2x_{k-1} + x_{k-2} \approx 0 \tag{13}$$

To make the directional function smoother, (13) is equivalent to minimizing the following equation:

$$\sum_{k=1}^{K} \left(x_k - 2x_{k-1} + x_{k-2}\right)^2. \tag{14}$$

Therefore, the estimation of directional spreading function should maximize the likelihood of (12) and minimize that of (14) at the same time, which is equivalent to maximizing the following equation:

$$\sum_{i=1}^{2N}\left[\varphi_i - \sum_{k=1}^{K} \alpha_{ik} \exp\ (x_k)^2\right] + u^2\left[\sum_{k=1}^{K}\left(x_k - 2x_{k-1} + x_{k-2}\right)^2\right], \tag{15}$$

where u^2 is an additional hyperparameter. The introduction of this hyperparameter aims to meet the requirement of maximizing the likelihood (12) and minimizing that of (14) simultaneously. The optimal solution of u^2 and σ^2 should minimize Akaike's Bayesian Information Criterion (ABIC) to achieve the most suitable balance between smoothness and continuousness. Consequently, the resultant directional function is the potentially most suitable one. The ABIC reads as follows:

$$\text{ABIC} = -2\ \ln \int L\left(x, \sigma^2\right) p\left(x|u^2, \sigma^2\right) dx\ , \tag{16}$$

where $p(x|u^2, \sigma^2)$ is the prior distribution of $x = (x_1, x_2, \ldots, x_k)$:

$$p\left(x\,|\,u^2, \sigma^2\right) = \left(\frac{u}{\sqrt{2\pi}\,\sigma}\right)^K \exp\left[-\frac{u^2}{2\sigma^2}\sum_{k=1}^{K}\left(x_k - 2x_{k-1} + x_{k-2}\right)^2\right]. \tag{17}$$

The hyperparameter u and σ^2 can be numerically solved so that the approximation of directional spreading function and spectral density is determined. A flowchart demonstrating the procedure of the proposed approach is shown in Figure 2.

3. Numerical Validation and Application

The most convenient and valid way to test the estimation method of wave spectrum is via numerical experiments and is widely adopted for validation purposes in spectrum estimation [6, 25, 26]. Therefore, two numerical experiments are conducted on structures with various geometries to test the performance of the proposed approach on directional spectrum estimation.

3.1. Numerical Experiment 1: Circular Cylinder. Circular cylinder is one of the most common offshore structures either in aspect of scientific research or engineering practice and is one of the very few geometries with analytical solutions for wave diffraction problems. First, the analytical solution of the diffraction problem for the circular cylinder is introduced. As demonstrated in Figure 3(a), regarding a bottom-fixed circular cylinder in regular wave field with a wave height of H, frequency ω, the incident wave surface elevation reads as follows:

$$\eta(x,t) = \frac{H_w}{2} e^{ikx - i\omega t}. \tag{18}$$

The disturbed wave field, i.e., superposition of incident and diffracted waves, is written in the polar coordinate system as follows:

$$\eta(r,\theta,t) = \frac{H_w}{2}\left\{\sum_{m=0}^{\infty} \beta_m\left[J_m(kr) - \frac{J_m{}'(ka)}{H_m{}'(ka)} H_m(kr)\right]\cos(m\theta) e^{-i\omega t}\right\}. \tag{19}$$

Using relationship between wave pressure p and surface elevation η described by Airy wave theory, (19) becomes as follows:

$$p(r,\theta,z,t) = \rho g \frac{H_w}{2}\frac{\cosh(kz)}{\cosh(k\ d)}\left\{\sum_{m=0}^{\infty} \beta_m\left[J_m(kr) - \frac{J_m{}'(ka)}{H_m{}'(ka)} H_m(kr)\right]\cos(m\theta) e^{-i\omega t}\right\}. \tag{20}$$

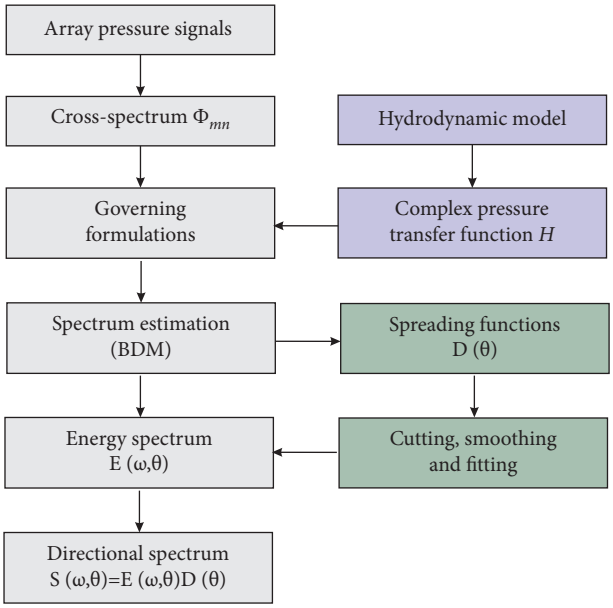

Figure 2: Flowchart of the proposed approach for wave spectrum estimation.

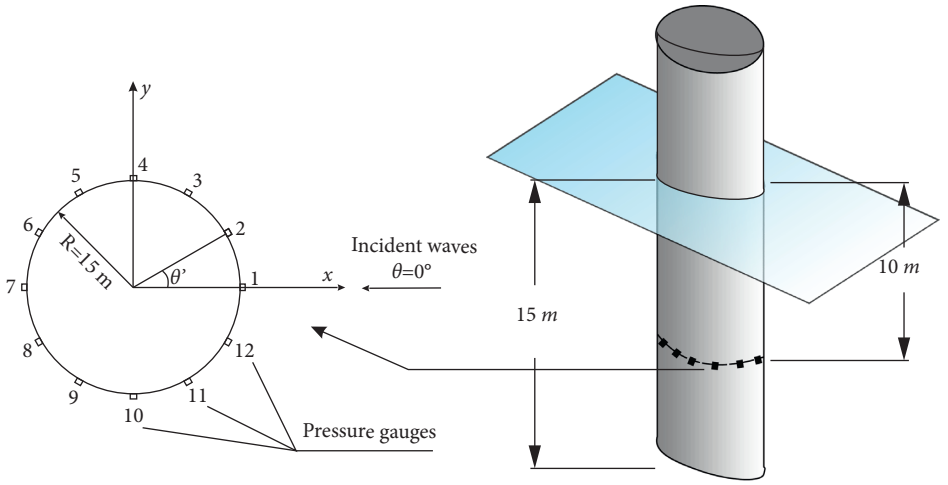

Figure 3: Structure layout and deployment of pressure gauges.

Assuming a pressure gauge is installed at location (x, y, z) in the Cartesian coordinate system and is converted to the polar coordinate system as (r, θ', z). If the incident wave direction is θ, the transfer function H of wave pressure at the gauge reads as follows:

$$H(\theta,k)=\rho g\frac{\cosh(kz)}{\cosh(k\ d)}\frac{\{\sum_{m=0}^{\infty}\beta_m[J_m(ka)-J_m{}'(ka)/H_m{}'(ka)H_m(ka)]\cos[m(\pi-(\theta-\theta'))]\}}{e^{ia\cos(\theta-\theta')}}. \tag{21}$$

Wave number k can be directly determined by frequency ω using dispersion relation and hence transfer function is also the function of wave frequency and direction, i.e., $H(\theta,\omega)$. Once the transfer function H is given, the directional wave spectrum can be estimated using (7) associated with the numerical procedure of BDM.

In the numerical experiment, the stochastic incident waves are determined by a JONSWAP spectrum associated with the cos2s-type directional spreading function. The spreading function writes as follows:

$$D(\theta)=G_0\cos^{2s}\left(\frac{\theta-\theta_0}{2}\right)=\frac{\Gamma^2(s+1)}{\Gamma(2s+1)}\cos^{2s}\left(\frac{\theta-\theta_0}{2}\right), \tag{22}$$

where s is the spreading parameter and θ_0 is the main wave direction. The input spectral parameters in the numerical experiment are significant wave height of $H_s = 3.5$ m , peak wave period $T_p = 9$s , peak enhancement factor$\gamma = 3.3$, which represents an observed extreme wave condition in nearshore area [27]. Main wave direction $\theta_0 = 0^\circ$ and spreading parameter $s = 15$. Twelve pressure gauges are evenly deployed at the depth of -10m around the cylinder, of which radius is 15m and the water depth is 15m, as illustrated in Figure 3.

In the numerical experiment, stochastic wave pressures on the cylinder are generated using the following formulation:

$$p_i(x, y, z, t) = \sum_{n=1}^{N} H_i(\omega_n, \theta_n, z) e^{i\left(k_n\left(x\cos\theta_n + y\sin\theta_n\right) - \omega_n t + \sigma_n\right)}, \tag{23}$$

where H is the analytical pressure transfer function (24) and i denotes the i^{th} wave pressure gauge and n denotes the n^{th} random components adopted. The sampling frequency is set at 3 Hz and the simulation duration is 600s. Afterward, the generated pressure data are fed to the presented approach to perform the spectrum estimation and the results are discussed.

3.2. Numerical Experiment 2: Quasirectangle Cofferdam. Cofferdam is a common facility to create a dry and safe construction environment when the foundation of offshore structures takes place below the water surface [27]. To perform accurate evaluation of hydrodynamic loads and structural safety, it is essential to estimate the wave spectra which the cofferdam is actually encountering. A quasirectangle cofferdam with rounded corners used for cross-sea bridge foundation construction is taken as an example in this study, as shown in Figure 4. The dimensions of the cofferdam are $23 \times 14.8 \times 12.3$ m. The cofferdam bottom is set at -4.4 m and the water depth is 10m. Eleven pressure gauges, which are a part of the structural health monitoring system, are embedded on the surface to monitor the real-time hydrodynamic load of the cofferdam. Due to the large scale of the structure, diffracted waves significantly affect the wave field which brings challenges to the accurate estimation of the directional wave spectrum.

Because of the complex geometry, the diffracted waves are difficult to obtain analytically and the numerical method, i.e., boundary element method (BEM), is hence employed to calculate the transfer function of diffracted waves and pressures. In BEM, a particular Green function that satisfies the boundary conditions in wave diffraction problems is introduced and the three-dimensional integration problem is reduced to a two-dimensional integration problem. The body surface is discretized into finite quadrilateral elements and the potentials and their derivations are calculated to evaluate the wave pressure. The details of employed BEM can be found in authors' previous article [24] and for the sake of conciseness, the details are not listed here. The BEM model and panel mesh of the cofferdam is illustrated in Figure 5(a). A total number of 11 complex pressure transfer functions are calculated using the BEM model and the real and imaginary part of the complex transfer function of wave pressure at #4 gauge on the cofferdam are shown as an example in Figures 5(c) and 5(d).

The stochastic wave pressure signals are simulated using (23) in Section 3.1 with the complex transfer function calculated by the BEM model. The still water level is +2.37 m, which represents a measured extreme wave condition. The input spectral parameters remain the same as employed in Section 3.1 and different main wave directions of 30°, 45°, and 60° are applied and tested. The sampling frequency is 3 Hz and the simulation time duration is 600s. The generated pressure data are fed to the presented approach to perform the spectrum estimation and the results are discussed.

3.3. Engineering Application. The real engineering practice for the cofferdam described of the numerical experiment 2 in Section 3.2 is taken as an engineering application. As illustrated in Figure 6, the steel thin-walled cofferdam for bridge foundation construction was set up at 25.72°N, 119.61°E in the China East Sea. The cofferdam was supported by 13 steel-concrete composite piles, of which the diameter is 2.2 m. The piles were fully fixed on the seabed rocks. Wave pressure was measured using 11 CSW560 flush type pressure gauges, of which the measuring range is 0 to 200 kPa and the measuring error is less than 0.5%. In addition, for validation purposes, the wave elevations were also measured using a single-point SBY 2–1 ultrasonic wave gauge deployed 80 m away from the cofferdam, of which the measuring accuracy is ±0.2 m for wave heights and ±0.25 s for wave periods. The field measurement of an extreme wave event was conducted on the morning of September 29, 2015, when Typhoon Dujuan was passing through the studied sea area. During the measurement, the storm eye was around 119.40°E, 25.00°N, which was about 80 km south from the tested cofferdam, as shown in Figure 7. The pressure at the storm center was 925 kPa and the maximum wind speed of the storm was 35 m/s. Actual wave pressure data on the cofferdam were successfully collected during the extreme wave events. More information about configurations of the in-situ measurement can also be found in a previous study [27]. The measured pressure time series were used to estimate the directional wave spectrum using the presented approach.

4. Result and Discussion

4.1. Numerical Experiment 1: Circular Cylinder

4.1.1. Effect of Gauge Arrays. Previous studies show that the success of spectrum estimation heavily depends on the appropriate choice of gauge array and therefore, it is necessary to investigate the effect of the array on the estimations. Four different plans with a various number of gauges and array patterns are tested, as shown in Table 1. Estimation of directional spectra contains two aspects, i.e., estimation of spreading function $D(\theta)$ and estimation of spectral density $S(f)$. $S(f)$ representing the energy distribution is relatively easy to estimate while $D(\theta)$ containing directional

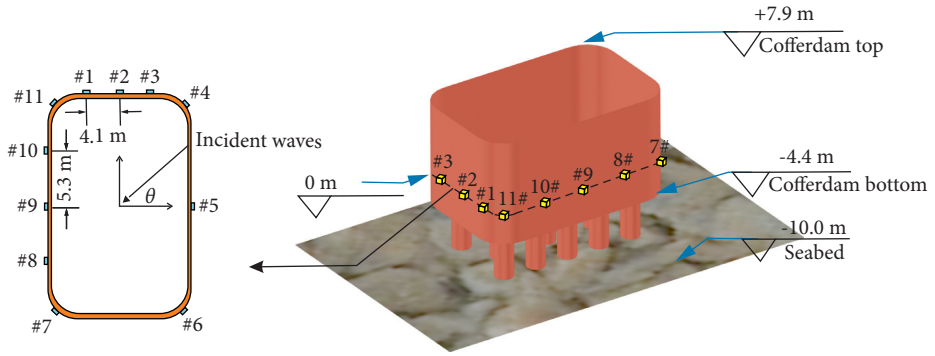

Figure 4: Cofferdam layout and deployment of pressure gauges.

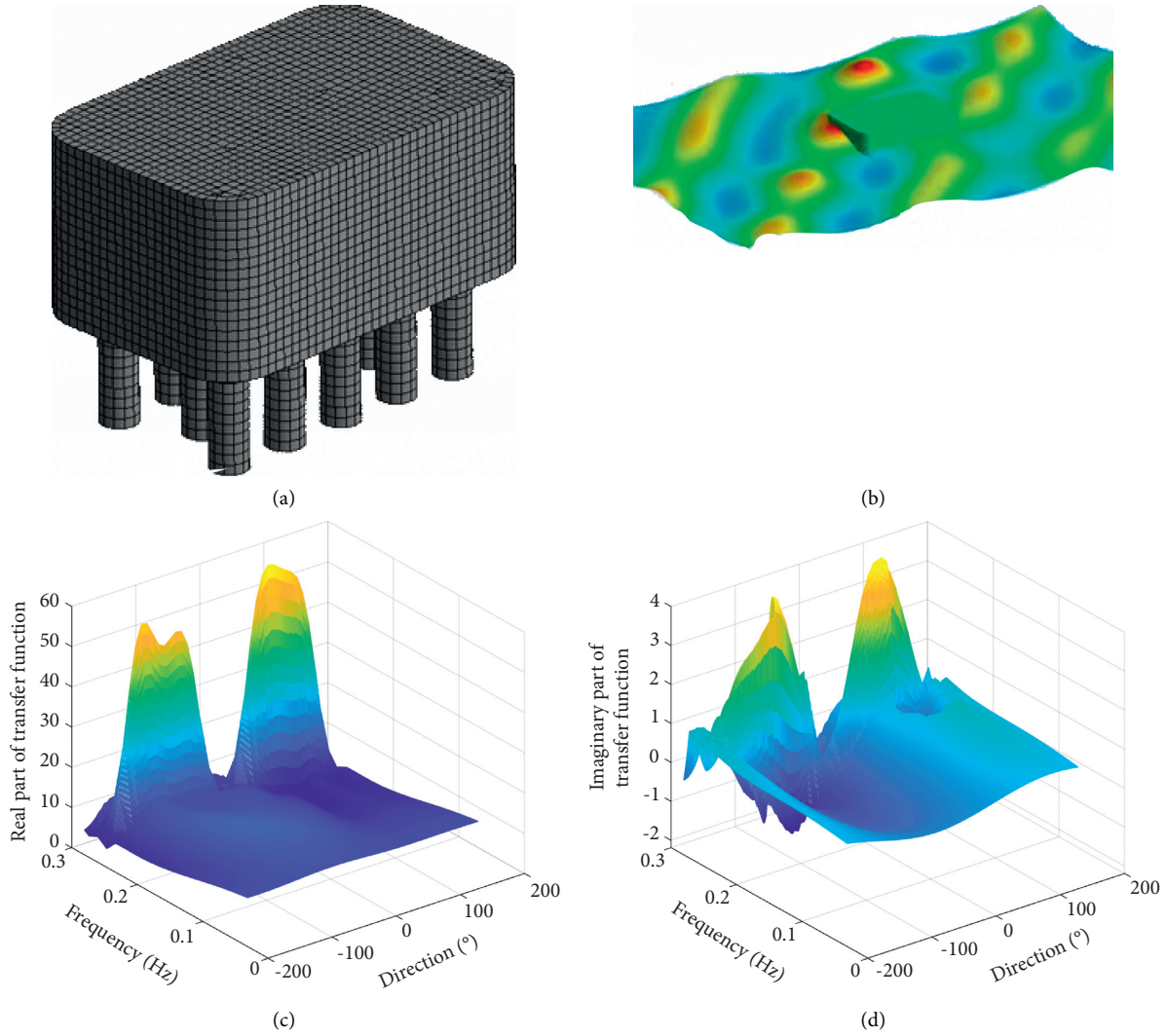

Figure 5: BEM model and pressure transfer function on the cofferdam: (a) panel mesh of cofferdam; (b) wave field simulation around the cofferdam; (c) real part of the pressure transfer function at #4 pressure gauge; (d) imaginary part of the pressure transfer function at #4 pressure gauge.

information is trickier and more important and hence draws more attention in previous studies [4, 6, 28]. Therefore, the estimation of $D(\theta)$ is a priority in this study and will be put more discussions. The corresponding estimated spreading functions $D(\theta)$ are illustrated in Figure 8. It can be observed that Plan 1, which employs 7 gauges, gives the most plausible result. Though Plans 2 and 3 reasonably predict the shape of the target spreading function, they slightly underestimate the

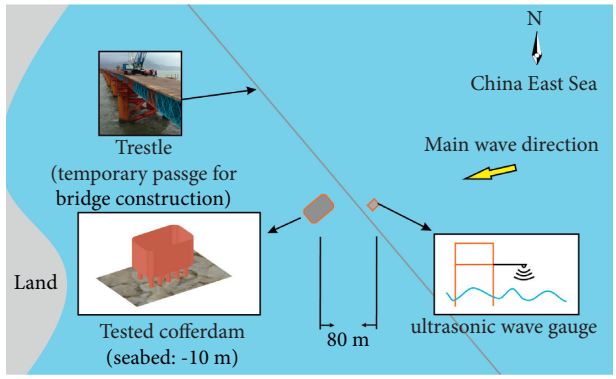

Figure 6: Layout of the measurement site.

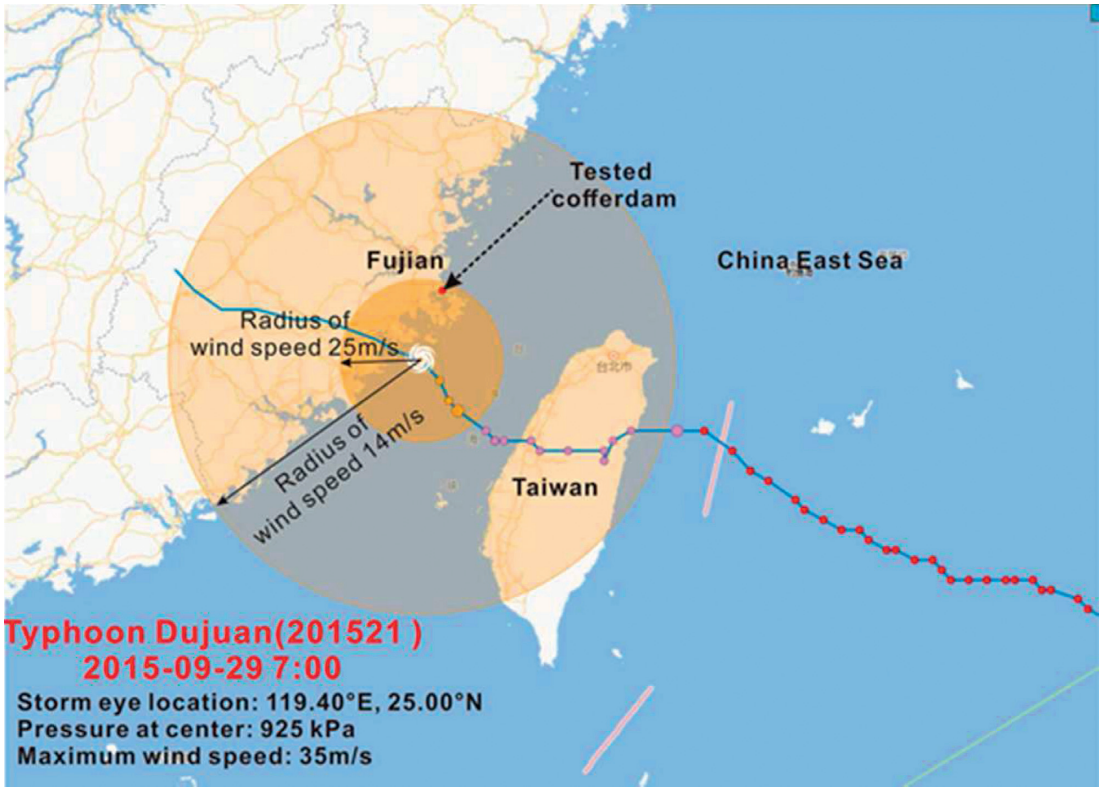

Figure 7: Location of the typhoon during the measurement.

Table 1: Different plans to test the effect of array pattern.

Array pattern	Gauge no.	Number of employed gauges
Array 1	4, 3, 2, 1, 12, 11, 10	7
Array 2	4, 2, 1, 12, 10	5
Array 3	3, 1, 11	3
Array 4	5, 6, 7, 8, 9	5

peaks. Plan 4 deviates significantly from the target and is not applicable. It is worthwhile to notice that in Plan 1, compared with the target directional function, the estimated spreading function has two small 'wings' in directions of -180° to -90° and 90° to 180°. This phenomenon is due to the fact that the diffracted waves are a series of cylindrical waves which are scattered from the cylinder surface in all directions, as demonstrated in Figure 9(a) and Figure 1(b). The proposed approach separates all wave components and the side "wings" represent the diffracted wave components. Since we are only interested in the incident waves, the spreading function is cut off at the tails and only the main peak which represents the incident waves is retained, as explained in Figure 8(b). This cutting action is conducted in all the following results to manually eliminate the diffracted components.

To enhance the advantage of the proposed approach, the estimated results are compared with the conventional approach [5] (4), i.e., using pressure signals to estimate the directional spectrum without considering the diffraction effect, and the comparison is shown in Figure 10. It can be seen that the proposed approach successfully estimates the spreading function while the conventional approach

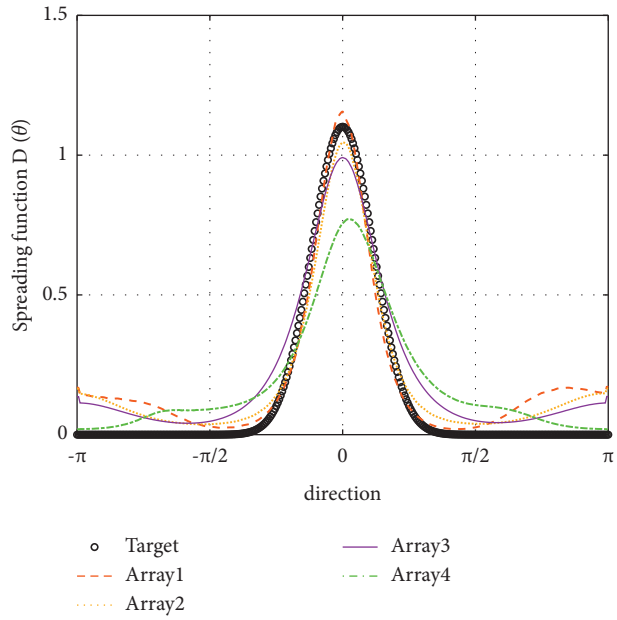

Figure 8: Estimated spreading function using different arrays.

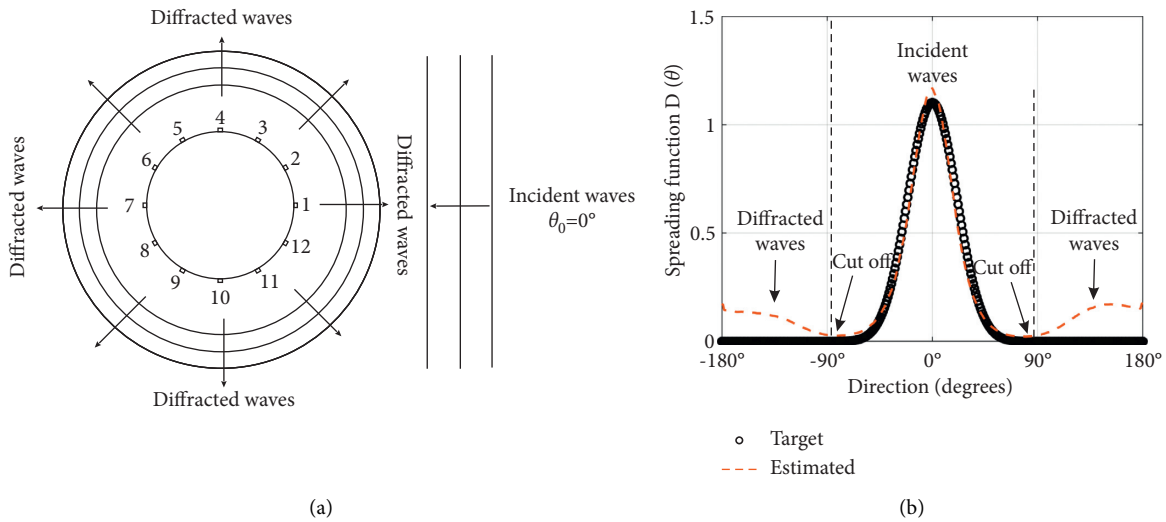

Figure 9: Separation of the incident and diffracted wave spectral components: (a) sketch of diffracted waves; (b) incident and diffracted spectral components.

underestimates the peak and overestimates the width of the spreading function because it cannot separate the coupled incident and diffracted wave components. With respect to the estimated spectral density $S(f)$, Figure 10(b) shows that the conventional approach significantly overestimates the spectral density while the presented approach aligns with the target well. Figure 11 illustrates the estimated three-dimensional directional spectra and shows that the conventional approach poses significant discrepancies of the direction and energy distribution in the estimated spectrum and overestimates the significant wave height and main wave direction. The presented approach agrees well with the target spectrum. It again proves that it is necessary to consider the diffraction effect in spectrum estimation and the conventional approach may lead to significant errors.

4.1.2. Effect of Spreading Coefficient. The spreading coefficient s in the spreading function $D(\theta)$ dominates the width of wave direction distribution and represents different types of sea states. To test the ability of the proposed approach on spectrum estimation with different spreading coefficients s, stochastic wave pressure data with $s = 10$, 25, and 75 are generated and used to perform the spectrum estimation. According to Goda [29], these three typical spreading coefficients represent sea states of wind wave ($s = 10$), short-distance decaying swell ($s = 25$), and long-distance decaying swell ($s = 75$). The estimated spectra are compared with the target and presented in Figure 12. Note that all estimations are performed using Array 1 validated in the previous section, and diffracted components are eliminated. All spectra are normalized by the maximal value in the target

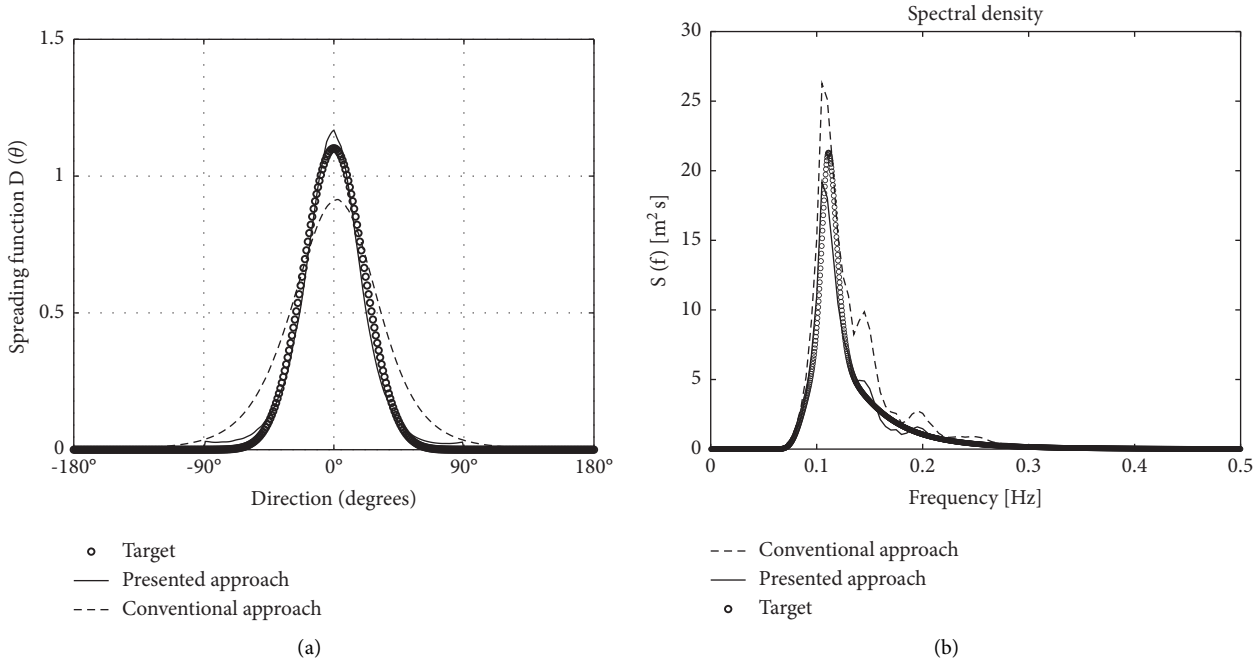

Figure 10: Comparison of estimated spreading function and spectral density: (a) spreading function; (b) spectral density.

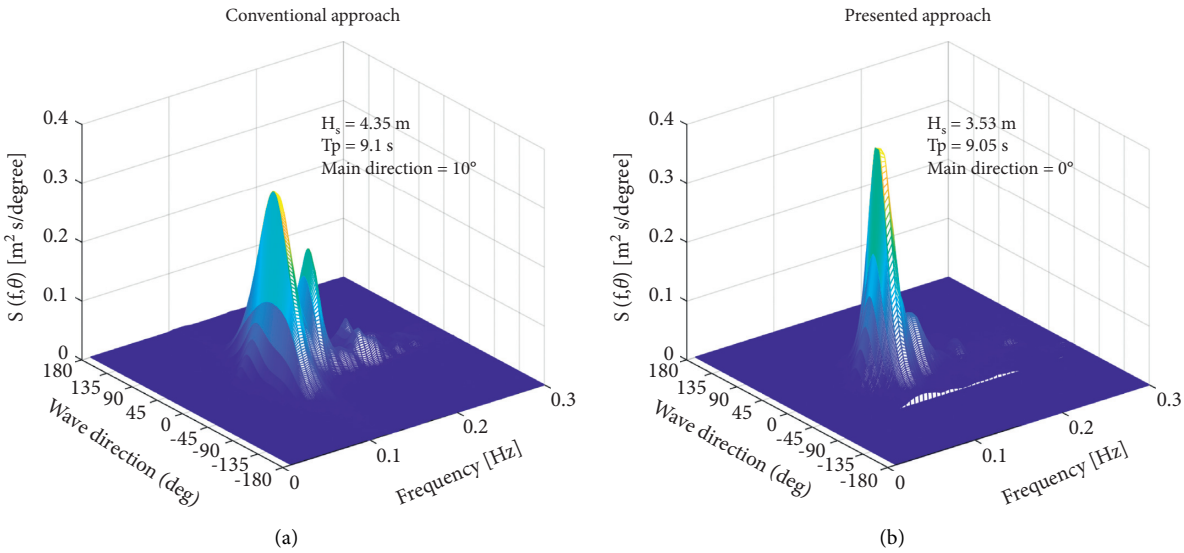

Figure 11: Continued.

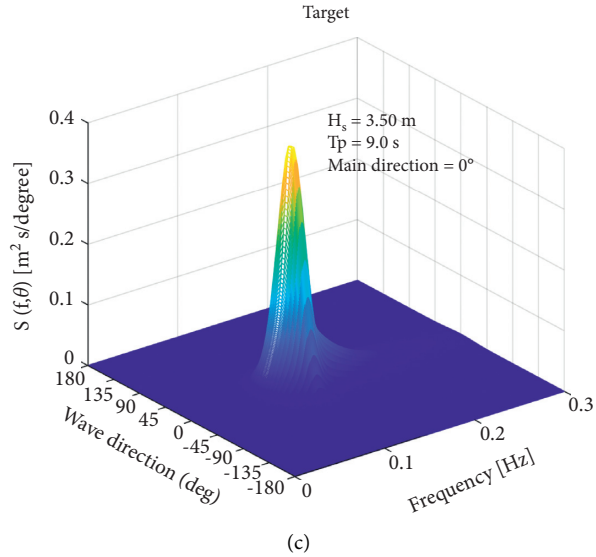

(c)

Figure 11: Comparison of estimated directional wave spectra: (a) conventional approach; (b) presented approach; (c) target spectrum.

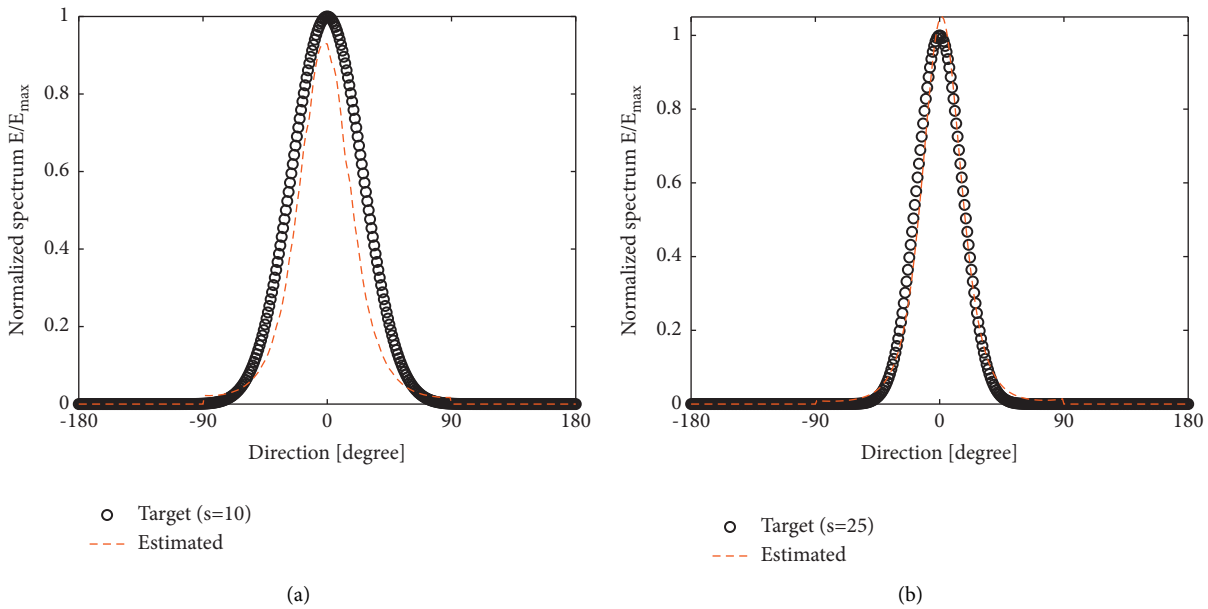

(a) (b)

Figure 12: Continued.

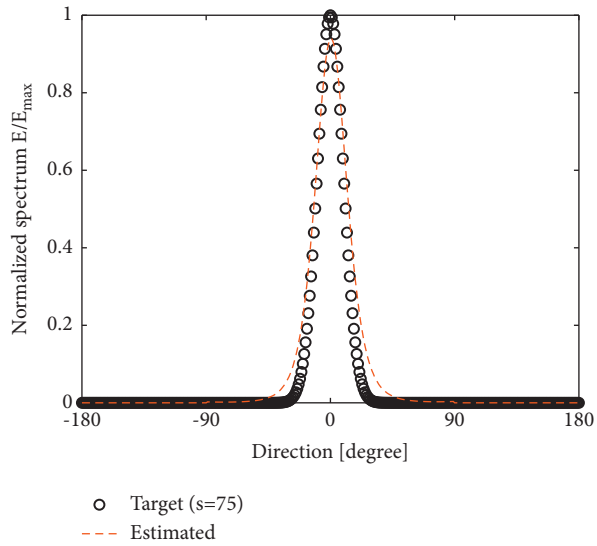

(c)

FIGURE 12: Estimated spreading function under various sea states: (a) spreading coefficient (s) = 10; (b) spreading coefficient (s) = 25; (c) spreading coefficient (s) = 75.

spectra, i.e., $E(\theta, f)/E(\theta, f)_{\max}$ in order to have a better view for comparison. It shows that the proposed approach estimates reasonable directional spectra for all spreading coefficients, though it seems to slightly underestimate the width of directional spreading for scenario $s = 10$, and some slight deviations in the peak estimations. Nevertheless, it shows that the presented approach can give plausible directional estimations under various sea states.

4.1.3. Effect of Background Noise. In engineering practice, measurement data inevitably contain background noise, and therefore is necessary to investigate the effect of noise on estimating performance. Noise level is usually measured by signal-noise-ratio (SNR), which is defined as the ratio of signal power to noise power:

$$\mathrm{SNR} = \frac{P_{\mathrm{Signal}}}{P_{\mathrm{Noise}}}. \tag{24}$$

The unit of SNR is dB and a large value of SNR indicates good quality signals. In this study, artificial Gaussian white noise is mixed into the simulated pressure signals to generate pressure data with noise, and pressure data with various levels of noise (SNR = 100, 50, 20, and 10) are fed to the estimation approach to test its performance against noise. The estimated directional spectra are normalized and shown in Figure 13. Note that to illustrate the original estimations, the diffraction components, i.e., the side wings, are not cut off in the results. It indicates that the estimated results have a reasonable agreement with the target when SNR = 100, 50, and 20, while it underestimates the peak value and overestimates the width of spreading function when SNR = 10. With the increasing background noise, the accuracy of estimated spectra drops and leads to deviations in directional spreading. However, in general, the results reveal that the

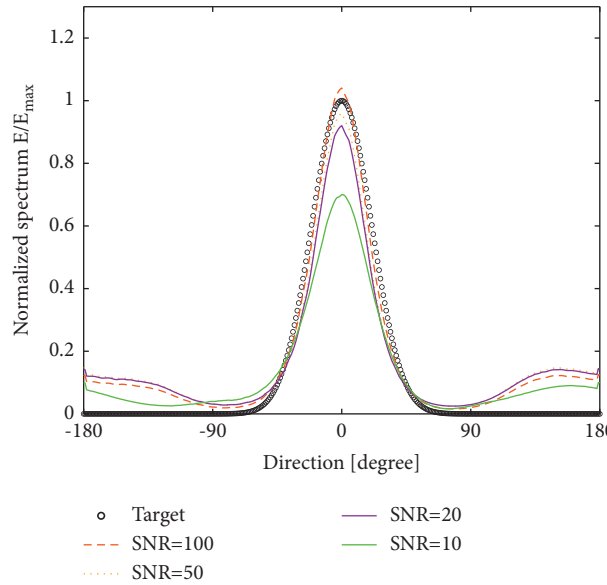

FIGURE 13: Estimated spectra under various levels of background noise in pressure data with SNR = 100, 50, 20, and 10.

presented method performs well against background noise which should attribute to the good noise resistance of the BDM itself. (11) shows that BDM has considered a Gaussian error term in its governing formulations and hence can, to a considerable degree, eliminate the background noise and gives favorable estimation. The good performance in noise resistance of the method provides a basis for further application into field measurement.

4.2. Numerical Experiment 2: Quasirectangle Cofferdam. This numerical experiment is used as a proof-of-concept study and aims to further deploy into a real in-situ

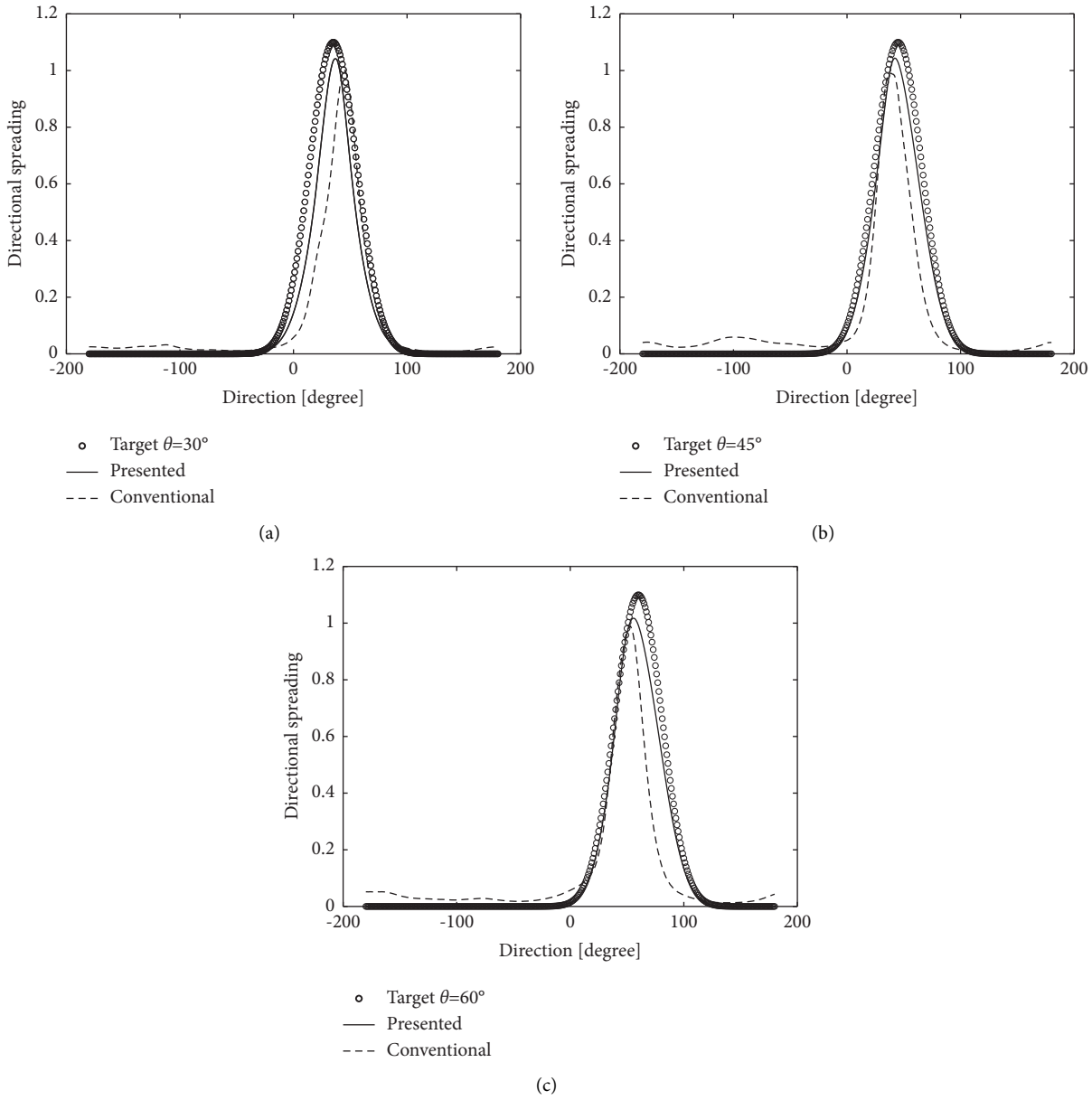

Figure 14: Estimated spreading functions under various wave directions: (a) $\theta = 30^{\circ}$; (b) $\theta = 45^{\circ}$; (c) $\theta = 60^{\circ}$.

application. By performing the same procedure in Section 4.1, the effect of gauge array, spreading coefficients and background noise can be tested to choose the best array and validate the presented approach. For the sake of conciseness, the similar results are not illustrated and discussed again. This section will pay more attentions to the effect of wave direction on spectrum estimation. Since the cofferdam is a noncentrosymmetric geometry and the effect of incident wave directions on spectrum estimation should be carefully discussed. In this case, 5 gauges including #1, #2, #4, #5, and #6 are taken as the estimation array. The input simulated pressure signals are mixed with Gaussian white noise with SNR = 20. The estimated spreading function $D(\theta)$ and spectral density $S(f)$ regarding various incident wave directions of 30°, 45°, and 60° are illustrated in Figures 14 to 17, respectively. Note that according to the long-term in-site observation, the main wave directions at the studied cofferdam concentrate in a relative narrow range about 30°–60° due to the local seabed topography and opening direction of the strait, as shown in Figures 6 and 7. Therefore, only wave directions of 30°, 45°, and 60° are tested and discussed. The estimated results using the presented approach are also compared with the conventional approach to enhance the effect of diffracted waves. Figure 14 shows that, in general, the presented approach reasonably estimates most of the spreading functions and main wave directions, while some slight discrepancies in main directions are still observed in case $\theta = 30^{\circ}$ and $\theta = 60^{\circ}$ and the presented approach underestimates the width of directional functions in case $\theta = 30^{\circ}$. Nevertheless, the presented approach still shows advantages over the conventional approach, which obviously underestimates the width of the spreading function and

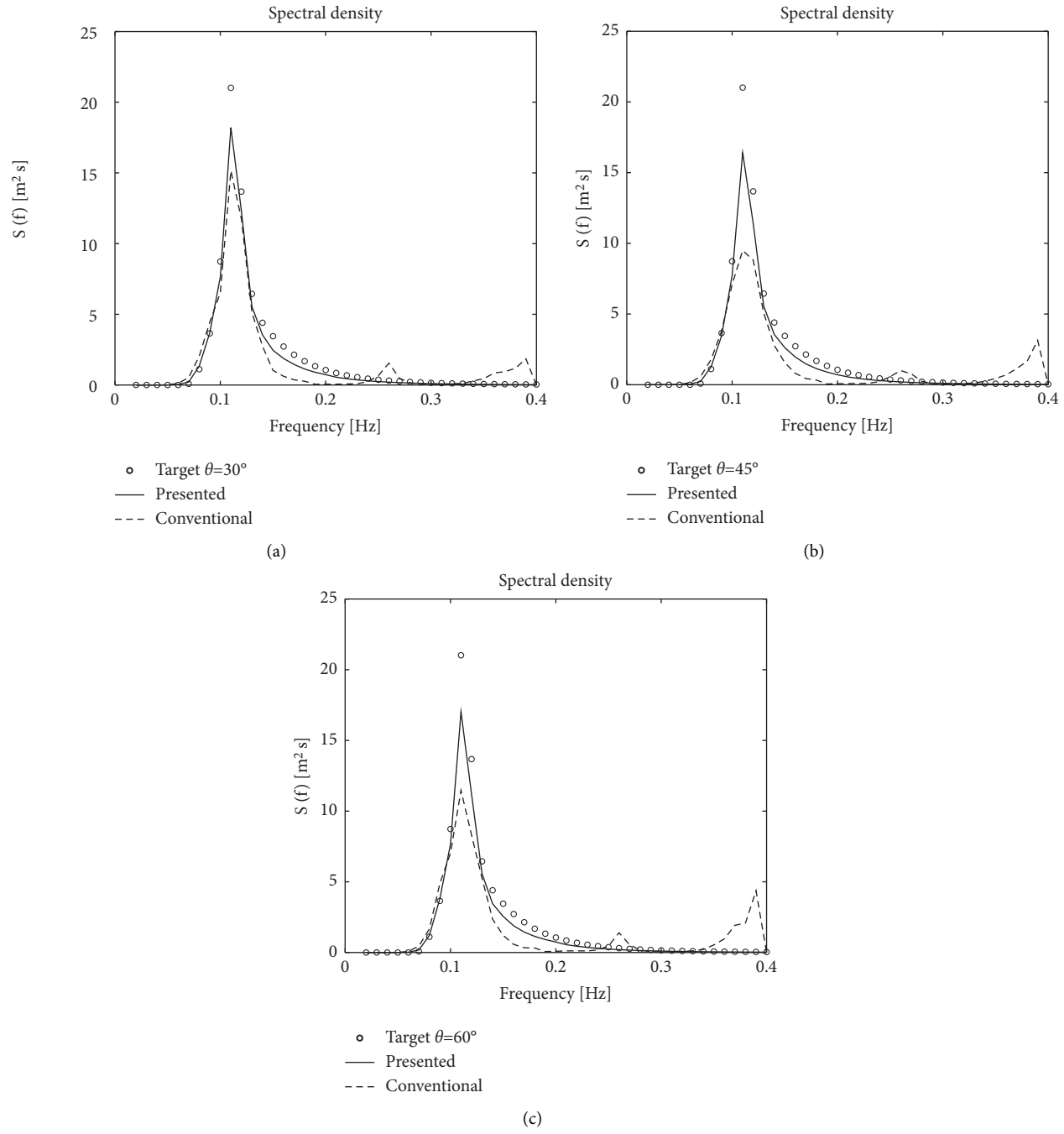

Figure 15: Estimated spectral density under various wave directions: (a) $\theta = 30^{\circ}$; (b) $\theta = 45^{\circ}$; (c) $\theta = 60^{\circ}$.

predicts inaccurate main directions due to a lack of ability to separate incident and diffracted wave components. In Figure 15, it reveals that the conventional approach significantly underestimates the peak energy and spectral width. The conventional approach also causes some unnecessary high frequency components, which could impose errors in wave spectra for real engineering applications. Compared with conventional approach, the presented approach obviously improves the spectral density estimation by considering the coupled relationship between incident and diffracted waves. It indicates that the presented approach can yield appreciable spectrum estimations for various wave directions and provides basis for further application into in-situ measurement.

4.3. Application: Field Measurement Data Analysis. A series of wave pressure measurement data during typhoon Dujuan in 2015 on an actual quasirectangle cofferdam, which has been discussed in Section 4.3, is applied to estimate the directional wave spectrum. Figure 16 shows four samples of estimated three-dimensional directional spectra collected at

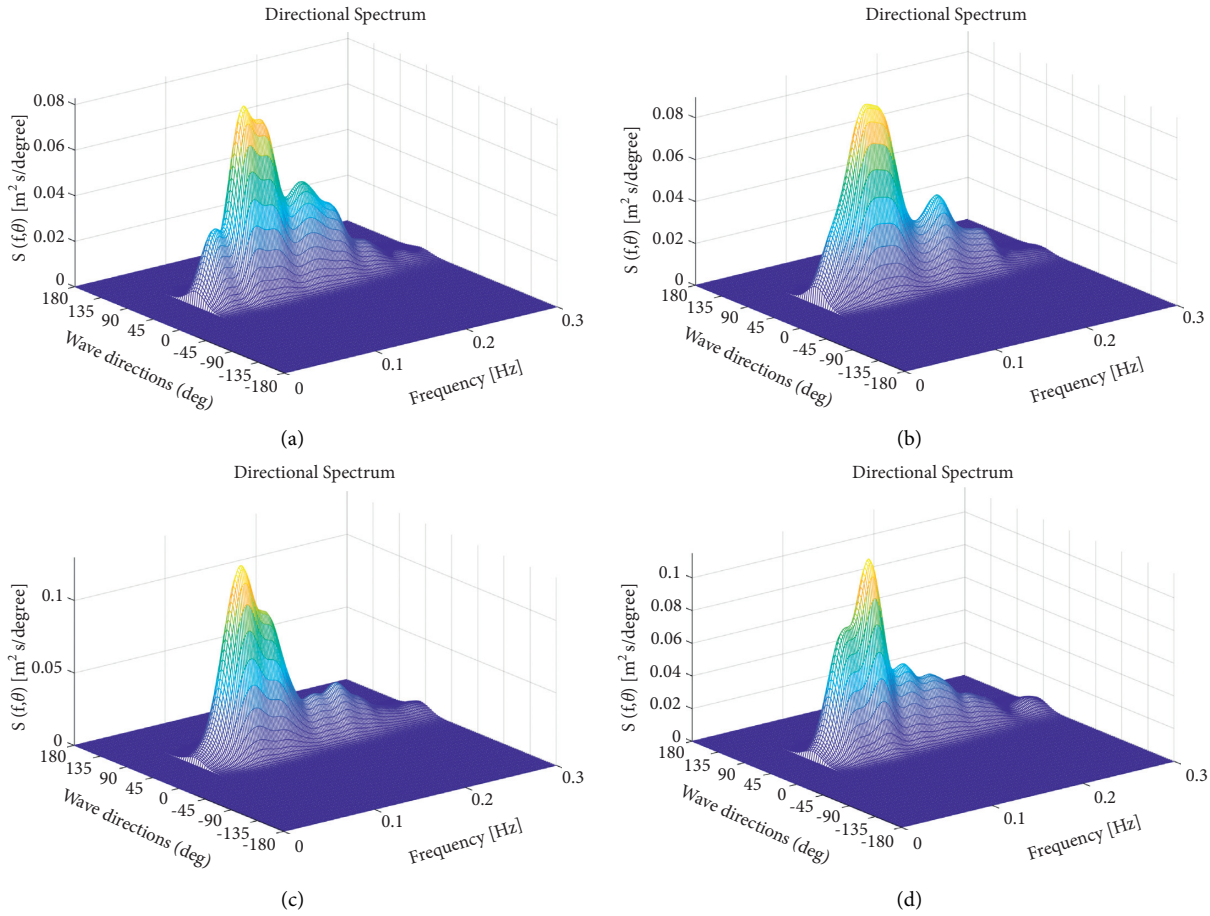

Figure 16: Estimated directional spectra at different moments during Typhoon Dujuan: (a) 2015/09/29 0 : 00; (b) 2015/09/29 0 : 10; (c) 2015/09/29 1 : 10; (d) 2015/09/29 2 : 00.

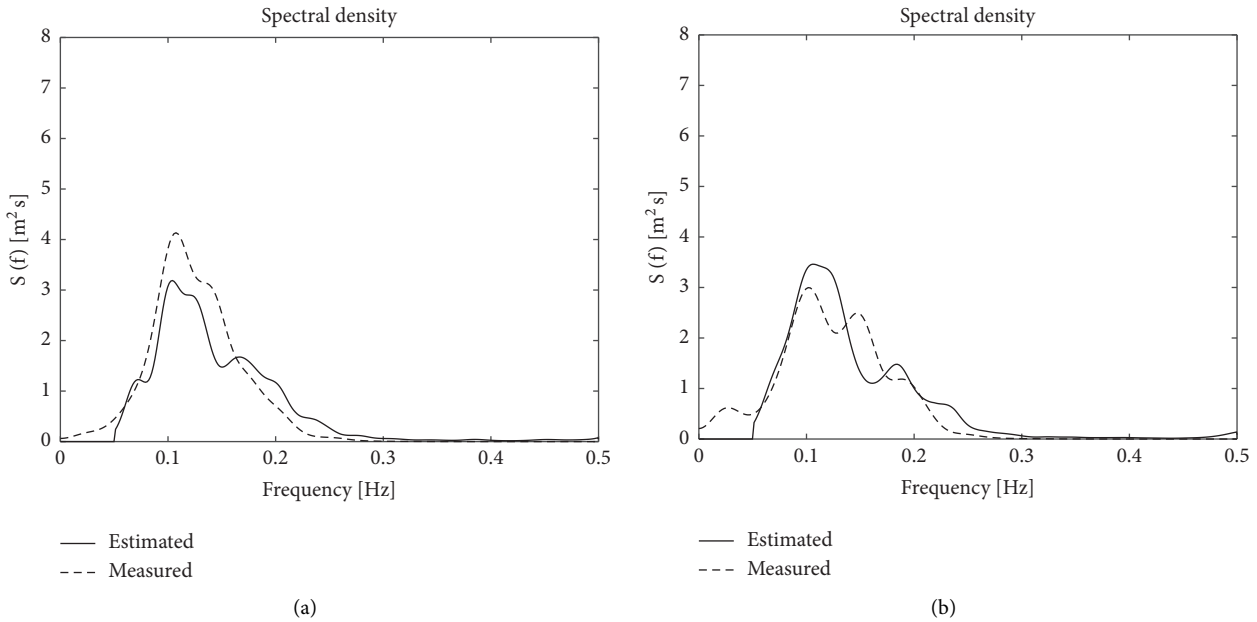

Figure 17: Continued.

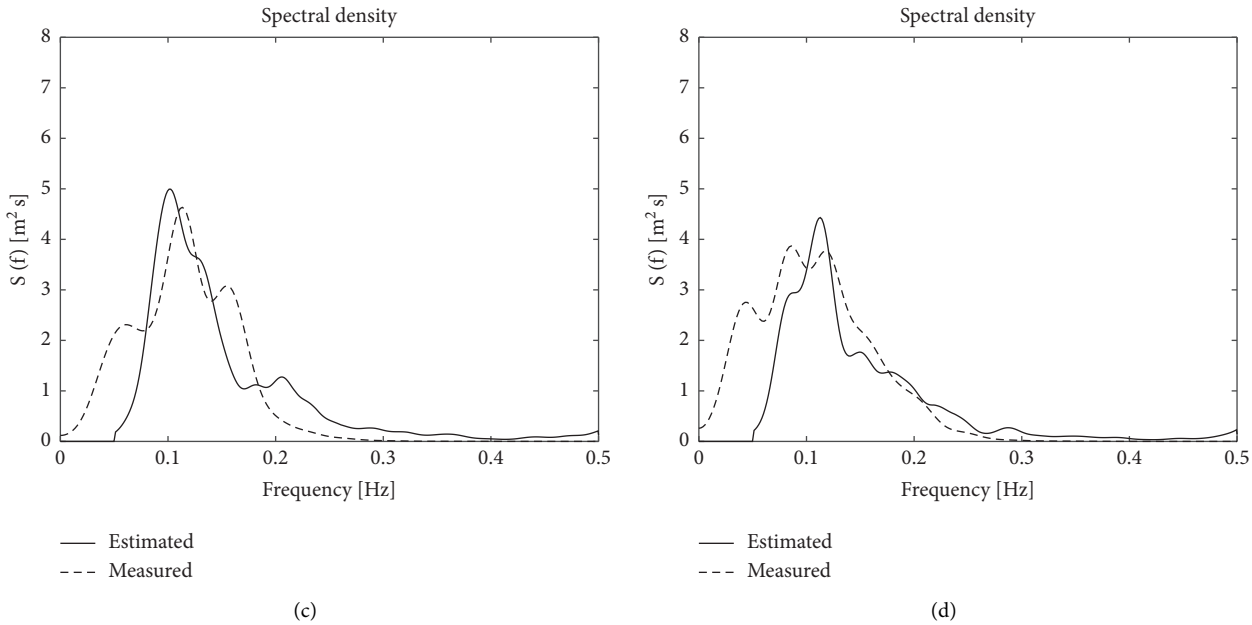

Figure 17: Estimated and measured spectral density at different moments during Typhoon Dujuan: (a) 2015/09/29 0 : 00; (b) 2015/09/29 0 : 10; (c) 2015/09/29 1 : 10; (d) 2015/09/29 2 : 00.

different moments during 2015/09/29 0 : 00 to 2015/09/29 02 : 00. It indicates that the presented approach works robustly on the measurement samples. The measured directional spectra reveal that during this typhoon event, the main wave directions are $\theta = 49^{\circ}$–61° and the fitting spreading coefficient $s = 22.5$–28.8, representing sea states transiting from wind waves to short distance decaying swells. To validate the results, the estimated spectral density is compared with measured spectral density, which is collected using a single-point style ultrasonic wave gauge, as introduced in Section 3.3 and Figure 6. Note that the wave gauge is only capable of analyzing two-dimensional spectra because the elevation data at a single point is insufficient for wave directional estimation. Nevertheless, the comparison of spectral density can, to a certain extent, prove the consistency and validity of the presented approach in spectrum estimation. Figure 17 demonstrates the comparison of estimated and measured spectral density. It indicates that the presented approach estimates the spectral density with a reasonable agreement, though some deviations are found in low frequency range. It should be noted that the wave gauge is about 80m away from the cofferdam, and the spatial variability of wave spectral characteristics may cause these deviations in estimated and measured spectra, which is a reasonable explanation of deviations in the comparison of spectral density in Figure 17. In general, the presented approach works well in in-situ measurement and can estimate the wave spectra with plausible accuracy. It provides proof-of-concept evidence for potential applications in more offshore engineering practice.

5. Conclusion

In the present study, the diffraction wave theory is introduced into the estimation of directional wave spectrum to consider the effect of diffracted waves using array pressure data from existing pressure gauges on structures. Two numerical experiments are conducted as proof-of-concept studies to test and evaluate the feasibility of the presented approach under various structures and wave scenarios. The performance of the presented approach using various gauge arrays, different wave directions and spreading coefficients, and multiple levels of background noise is evaluated and discussed, respectively. The presented approach is also deployed into an in-situ measurement application and compared with wave observation data to test its validity in engineering practice.

The numerical experiments show the validity of the presented approach. By using the correct transfer function, either analytical or numerically modeled, the presented approach can estimate the directional spectra under various wave scenarios with a plausible agreement. The gauge array significantly affects the spectrum estimation and a sensitive test is necessary. A high level of background noise can lead to deviations in estimated spectra while the presented approach has a good noise resistance which should attribute to the BDM method. The presented approach shows apparent advantages over the conventional approach in diffracted and incident wave field, which indicates that considering the diffraction effect in spectrum estimation is essential. The presented approach works well in in-situ applications and can estimate the wave spectra with plausible accuracy. The estimated spectra during Typhoon Dujuan in 2015 show that the sea states which the cofferdam was actually encountering have the main wave directions of 49°–61° and the fitting spreading coefficient $s = 22.5$–28.8, representing sea states transiting from wind waves to short distance decaying swells. The experiment results and engineering application provide proof-of-concept evidence of the presented approach for potential applications in more engineering practice.

The presented approach uses existing pressure gauges which are a part of the structural health monitoring (SHM) system, is a low-cost alternative for spectrum estimation, and shows potentials and advantages for engineering practice. However, this article aims at a proof-of-concept study and some limitations should be pointed out. At present, only a uni-modal incident wave situation is considered. If the incident waves are bimodal, i.e., the superposition of two or more sea states, the diffracted components may fall into the incident directional range, and therefore, the spectral components of the incident and diffracted waves are mixed and cannot be manually eliminated. This case requires autorecognition and separation of diffracted and incident components, which may call for a more advanced mathematical model in spectrum estimation. Another inherent difficulty in separating incident and diffracted waves is that diffracted waves are usually cylindrical waves which means they may distribute in all directions. When the incident waves spread in a wide range, they inevitably overlap over the diffracted waves and may affect the estimated spectrum. Selection for the most suitable gauge array under these scenarios should be very careful and requires further investigation and knowledge. Note that the diffraction effect is only significant for large-scale structures and becomes negligible for components like offshore structure legs. In the future, more experimental or measured data should be collected to further test the validity of the presented method under more complex sea states. Some advanced methods [30] are worthwhile to implement to further improve the accuracy and smoothness in estimated spectra.

Data Availability

The spectral data presented in the figures are available from the corresponding author upon request.

Conflicts of Interest

The authors declared no potential conflicts of interest with respect to the research, authorship, and/or publication of this article.

Acknowledgments

This work was supported financially by the National Natural Science Foundation of China (Grants no. 52008349), Postdoctoral Science Foundation of China (Grants nos. 2020M683356, 2021T140573), and the Fundamental Research Funds for the Central Universities (Grants no. 2682021CX004).

References

[1] J. Liu, A. Guo, H. Li, and H. Hu, "Methodology for wave force monitoring of bottom-mounted cylinder using the measurement of the wave surface elevation around the body surface," *Journal of Fluids and Structures*, vol. 78, pp. 197–214, 2018.

[2] Z. Ti, M. Zhang, Y. Li, and K. Wei, "Numerical study on the stochastic response of a long-span sea-crossing bridge subjected to extreme nonlinear wave loads," *Engineering Structures*, vol. 196, Article ID 109287, 2019.

[3] R. MacCamy and R. A. Fuchs, "Wave Forces on Piles: A Diffraction Theory," in *Corps of Engineers,* Beach Erosion Board, Washington, DC, USA, 1954.

[4] N. Hashimoto, K. Kobune, N. Hashimoto, and K. Kobune, "Directional Spectrum Estimation from a Bayesian Approach," in *Proceedings of the 21th ICCE*, pp. 62–76, ASCE, Malaga, Spain, 1988.

[5] G. L. Howell, "Shallow water directional wave gages using short baseline pressure arrays," *Coastal Engineering*, vol. 35, no. 1-2, pp. 85–102, 1998.

[6] M. Isobe and K. Kondo, "Method for estimating directional wave spectrum in incident and reflected wave field," in *Proceedings of the 19th ICCE*, pp. 467–483, Houston, TX, USA, 1984.

[7] Y. U. Yu, L. M. Shao, and Dalian, "Estimation of directional spectrum and reflection coefficient of incidentand reflected waves in the phase-locked wave field," *Ocean Engineering*, vol. 21, pp. 34–41, 2003.

[8] C. Lee, J.-S. Jung, and M. C. Haller, "Asymmetry in directional spreading function of random waves due to refraction," *Journal of Waterway, Port, Coastal, and Ocean Engineering*, vol. 136, no. 1, pp. 1–9, 2010.

[9] J. Liu, Q. Fang, A. Guo, and H. Li, "Real-time nonlinear cylinder wave force reconstruction in stochastic wave field considering second-order wave effects," *Journal of Fluids and Structures*, vol. 98, Article ID 103132, 2020.

[10] J. M. Nichols, "Structural health monitoring of offshore structures using ambient excitation," *Applied Ocean Research*, vol. 25, no. 3, pp. 101–114, 2003.

[11] S. F. Barstow, J.-R. Bidlot, S. Caires, M. A. Donelan, W. M. Drennan, and H. Dupuis, "Measuring and Analysing the Directional Spectrum of Ocean Waves," *COST Office*, 2005.

[12] H. E. Krogstad and S. F. Barstow, "Recent Advances in Wave Measurement Technology," in *Proceedings of the 9th International Offshore and Polar Engineering Conference*, Brest, France, 1999.

[13] N. F. Barber, "Finding the direction of travel of sea waves," *Nature*, vol. 174, no. 4440, pp. 1048–1050, 1954.

[14] B. Strong, B. Brumley, E. Terray, and G. W. Stone, "The performance of ADCP-derived directional wave spectra and comparison with other independent measurements," in *Proceedings of the OCEANS 2000 MTS/IEEE Conference and Exhibition Conference Proceedings (Cat No 00CH37158)*, pp. 1195–1203, IEEE, Providence, RI, USA, september 2000.

[15] M. Isobe, K. Kondo, and K. Horikawa, "Extension of MLM for estimating directional wave spectrum," *Proc Symp on Description and modeling of directional seas*, pp. 1–15, 1984.

[16] A. Lygre and H. E. Krogstad, "Maximum entropy estimation of the directional distribution in ocean wave spectra," *Journal of Physical Oceanography*, vol. 16, no. 12, pp. 2052–2060, 1986.

[17] U. D. Nielsen, "Estimations of on-site directional wave spectra from measured ship responses," *Marine Structures*, vol. 19, no. 1, pp. 33–69, 2006.

[18] E. A. Tannuri, P. C. Mello, J. S. Sales, A. N. Simos, and V. L. F. Matos, "Estimation of directional wave spectrum using a wave-probe array," *Marine Systems & Ocean Technology*, vol. 3, no. 2, pp. 123–129, 2007.

[19] Y. Goda, "Random seas and design of maritime structures," *Advanced Series on Ocean Engineering*, World Scientific, vol. 33, World Scientific, Singapore, 3 edition, 2010.

[20] S. Draycott, T. Davey, D. M. Ingram, A. Day, and L. Johanning, "The SPAIR method: isolating incident and reflected directional wave spectra in multidirectional wave basins," *Coastal Engineering*, vol. 114, pp. 265–283, 2016.
[21] T. Iseki and K. Ohtsu, "Bayesian estimation of directional wave spectra based on ship motions," *Control Engineering Practice*, vol. 8, no. 2, pp. 215–219, 2000.
[22] T. Iseki and D. Terada, "Bayesian estimation of directional wave spectra for ship guidance system," *International Journal of Offshore and Polar Engineering*, vol. 12, 2002.
[23] E. A. Tannuri, J. V. Sparano, A. N. Simos, and J. J. Da Cruz, "Estimating directional wave spectrum based on stationary ship motion measurements," *Applied Ocean Research*, vol. 25, no. 5, pp. 243–261, 2003.
[24] Z. Ti, Y. Li, and S. Qin, "Numerical approach of interaction between wave and flexible bridge pier with arbitrary cross section based on boundary element method," *Journal of Bridge Engineering*, vol. 25, 2020.
[25] M. Donelan, A. Babanin, E. Sanina, and D. Chalikov, "A comparison of methods for estimating directional spectra of surface waves," *Journal of Geophysical Research: Oceans*, vol. 120, no. 7, pp. 5040–5053, 2015.
[26] N. Hashimoto, T. Nagai, and T. Asai, "Extension of the maximum entropy principle method for directional wave spectrum estimation," *European Journal of Pain*, vol. 11, pp. 466-467, 1994.
[27] Z. Ti, K. Wei, S. Qin, D. Mei, and Y. Li, "Assessment of random wave pressure on the construction cofferdam for sea-crossing bridges under tropical cyclone," *Ocean Engineering*, vol. 160, pp. 335–345, 2018.
[28] N. Hashimoto, T. Nagai, and T. Asai, "Extension of the maximum entropy principle method for directional wave spectrum estimation," in *Proceedings of the Symposium on Description and Modeling of Directional seas,* Paper No. A-6, Technical University of Denmark, Kongens Lyngby, Denmark, pp. 1–15, 1984.
[29] Y. Goda, "Statistical variability of sea state parameters as a function of wave spectrum," *Coastal Engineering in Japan*, vol. 31, no. 1, pp. 39–52, 1988.
[30] U. D. Nielsen, "Introducing two hyperparameters in Bayesian estimation of wave spectra," *Probabilistic Engineering Mechanics*, vol. 23, no. 1, pp. 84–94, 2008.

Hindawi
Shock and Vibration
Volume 2021, Article ID 5027939, 9 pages
https://doi.org/10.1155/2021/5027939

Research Article

Structure-Acoustic Coupling Analysis of Vibration and Underwater Acoustic Radiation of a Ring-Stiffened Conical Shell

Qingtao Gong,[1] Zhanyang Chen ,[2] Hongbin Gui,[2] and Dong Yu[2]

[1]*Ulshan Ship and Ocean College, Ludong Universtity, Yantai 264025, China*
[2]*School of Ocean Engineering, Harbin Institute of Technology at Weihai, Weihai 264209, China*

Correspondence should be addressed to Zhanyang Chen; chen_1228@163.com

Received 13 August 2021; Accepted 27 October 2021; Published 11 November 2021

Academic Editor: PengYao Yu

Copyright © 2021 Qingtao Gong et al. This is an open access article distributed under the Creative Commons Attribution License, which permits unrestricted use, distribution, and reproduction in any medium, provided the original work is properly cited.

The underwater acoustic radiation of the submarine power cabin has recently become a hot topic in the industry and also in the academia. In this article, the vibration and underwater acoustic radiation of a ring-stiffened conical shell with bases are investigated numerically by means of the combination of the finite element method and boundary element method. The acoustic radiation field is obtained by the traditional acoustic field model and ISO acoustic field model, respectively. A series of numerical examples are given, and the results are compared. Besides, the sound pressure at different positions with frequency is further studied. It is shown that the sound radiated by the structure mainly propagates to the side directions of the shell and propagates relatively less to the front side and the rear side.

1. Introduction

Fluid-structure interaction of flexible structures is a common phenomenon in both engineering and natural environments [1, 2]. In general, the surface vessels and submarines belong to flexible structure. The power cabin, which is located at the stern, directly determines the vibroacoustic characteristics and level of the whole ship. Consequently, structure-acoustic coupling analysis of the stern has great significance to the development of acoustic stealth. In physical applications, researchers and scholars usually regard the stern of submarine as a ring-stiffened conical shell and have conducted abundant research on the vibroacoustic problem [3–5].

The acoustic radiation is caused by the structural vibration. However, the structural vibration in the fluid medium is quite different from that in air or vacuum. Besides the vibration of structure itself, there is an interaction between the structure and fluid medium. When the structure is excited to produce vibration, the vibration boundary may compress the surrounding fluid to make the vibration propagate outwards in the form of wave, i.e., acoustic radiation. Meanwhile, the vibration of the surrounding fluid will occur and act on the structure as a radiation force, which is called the acoustic-structure coupling problem [6, 7]. The underwater acoustic radiation of the submarine occurs in the complex environment with an interaction of the structural vibration and water medium. Zou et al. [1] pointed out that the interaction belongs to a strong coupling problem, which could not be neglected. Thus, for underwater acoustic radiation problems, the acoustic-structure coupling effect has to be considered.

Generally speaking, for some regularly shaped structures, such as plates, cylindrical shells, spherical shells, and so on, analytical solution to the acoustic-structure coupling problem is available, while for most elastic structures, numerical simulation is the only method for calculation of acoustic radiation induced by the vibrating surface of structures. Two basic numerical methods are used to deal with acoustic problems. One is the acoustic finite element method (FEM) [8, 9]. The other one is the acoustic boundary element method (BEM) [1, 10, 11]. Liu et al. [12] studied the dynamic response and acoustic radiation of a blade-shafting-shell coupled system operating under unsteady excitation. Dynamic and acoustic experiments of the blade-shafting-shell coupled system were conducted. The results verified the accuracy of

the simulation model. Qu et al. [13] investigated the structural and acoustic responses of a coupled propeller-shafting-submarine pressure hull system under different propeller force excitations. Finally, computed results were compared with those solutions obtained from the coupled FEM/BEM. The effects of the ring and the bearing stiffness on the acoustic responses of the coupled system were discussed. Zou et al. [14] established a calculation method of underwater acoustic radiation for three-dimensional structures arbitrarily covered by acoustic coatings based on the three-dimensional sonoelasticity theory for ships [1, 2]. As an example, the acoustic radiation of a flat plate covered by acoustic coatings was numerically calculated and compared with analytical results, which verified the correctness of the proposed method. Moreover, a series of results for the cylindrical shell structure with partial acoustic coatings were presented, which showed the interest of this method in engineering practice.

Thus, the main purpose of this paper is to study the sound pressure level obtained by the different acoustic field models. By analyzing and quantifying the sound pressure level of different positions around the sound source, the spatial distribution law of acoustic radiation is presented, which will provide a reference for the acoustic stealth performance of submarine.

2. Finite Element Model and Relevant Parameters

2.1. Acoustic Finite Element Method. The FEM is widely used to investigate enclosure acoustic characteristics. According to the Helmholtz equation, the integral expression in the acoustic field can be written as

$$\int_V \tilde{p}\left(\nabla^2 p(x,y,z) - k^2 p(x,y,z) + j\rho_0 \omega q(x,y,z)\right)\mathrm{d}V = 0. \tag{1}$$

After a series of analysis and formula, we have

$$\int_V (\nabla\tilde{p}\cdot\nabla p)\mathrm{d}V - \omega^2\int_V\left(\frac{1}{c^2}\tilde{p}p\right)\mathrm{d}V = \int_V j\rho_0\omega\tilde{p}q\mathrm{d}V - \int_V (j\rho_0\omega\tilde{p}v\cdot n)\mathrm{d}\Omega. \tag{2}$$

Equation (2) consists of four parts, and the first item on the left side can be expressed as

$$\int_V (\nabla\tilde{p}\cdot\nabla p)\mathrm{d}V = \{\tilde{p}_i\}^T\cdot\int_V\left(\mathbf{B}^T\cdot\mathbf{B}\right)\mathrm{d}V\cdot\{p_i\} = \{\tilde{p}_i\}^T\cdot\mathbf{K}\cdot\{p_i\}, \tag{3}$$

where **K** is the stiffness matrix.

$$K_{ij} = \int_V\left(B^T\cdot B\right)\mathrm{d}V = \int_V\left(\frac{\partial N_i}{\partial x}\cdot\frac{\partial N_j}{\partial x} + \frac{\partial N_i}{\partial y}\cdot\frac{\partial N_j}{\partial y} + \frac{\partial N_i}{\partial z}\cdot\frac{\partial N_j}{\partial z}\right)\mathrm{d}V. \tag{4}$$

The second item on the left side of equation (2) can be expressed as follows:

$$-\omega^2\int_V\left(\frac{1}{c^2}\tilde{p}p\right)\mathrm{d}V = -\omega^2\{\tilde{p}_i\}^T\cdot\mathbf{M}\cdot\{p_i\}, \tag{5}$$

where **M** is the mass matrix.

$$M_{ij} = \int_V\left(\frac{1}{c^2}N_iN_j\right)\mathrm{d}V. \tag{6}$$

The first item on the right side of equation (2) can be expressed as follows:

$$\int_V j\rho_0\omega\tilde{p}q\mathrm{d}V = \{\tilde{p}_i\}^T\cdot\{Q_i\}, \tag{7}$$

where $\{Q_i\}$ is the acoustic excitation.

$$\{Q_i\} = \int_V\left(j\rho_0\omega N^T q\right)\cdot\mathrm{d}V. \tag{8}$$

The second item on the right side can be expressed as follows:

$$-\int_V (j\rho_0\omega\tilde{p}v\cdot n)\mathrm{d}\Omega = -j\omega\{\tilde{p}_i\}^T\cdot\mathbf{C}\cdot\{p_i\}, \tag{9}$$

where **C** is the damping matrix.

$$C_{ij} = \int_{\Omega_Z}\left(\rho_0 AN_iN_j\right)\mathrm{d}\Omega. \tag{10}$$

The dynamic equation of acoustic system will be obtained by substituting equations (4), (6), (8), and (10) into equation (2).

$$\left(K + j\omega C - \omega^2 M\right)\cdot\{p_i\} = \{Q_i\}. \tag{11}$$

The Helmholtz solution in physical space will be obtained by solving the above equation.

2.2. Relevant Parameters. For the presented FEM/BEM scheme, LMS Virtual.Lab is applied to establish the FEM model and conduct the modal analysis. A ring-stiffened conical shell model with bases is built and shown in Figure 1(a), where steel is selected as the material, and density, Poisson's ratio, elastic modulus, and loss factor are 7800 kg/m^3, 0.3, 210 GPa, and 0.001, respectively. The whole bases mainly consist of ribbed slabs, a plate, and a web, as shown in Figure 1(b). The main dimensions and relevant parameters are listed in Table 1.

The combination of FEM and BEM is used for the underwater structure-acoustic coupling analysis of the ring-

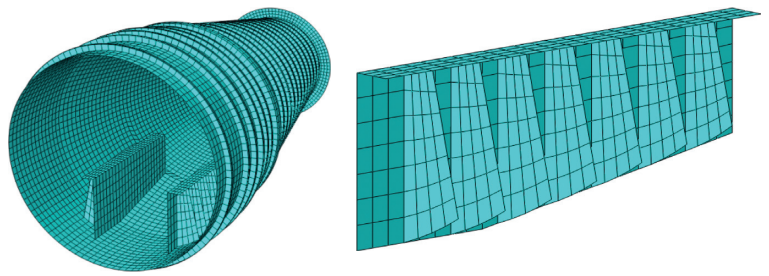

(a) (b)

Figure 1: Finite element model. (a) Ring-stiffened conical shell. (b) Base.

Table 1: Main dimensions and relevant parameters.

Item	Value
Full length (mm)	3200
Thickness (mm)	7
Diameter of the structural front-end (mm)	1750
Diameter of the structural back-end (mm)	840
Rib interval (mm)	150
Rib thickness (mm)	5
Plate thickness (mm)	10
Thickness of web (mm)	5
Thickness of ribbed slabs (mm)	5
Web width (mm)	100
Base length (mm)	1200
Distance of plate's front-end to shell surface (mm)	370
Distance of plate's back-end to shell surface (mm)	532.5
Distance from web to the longitudinal center plane of shell (mm)	325

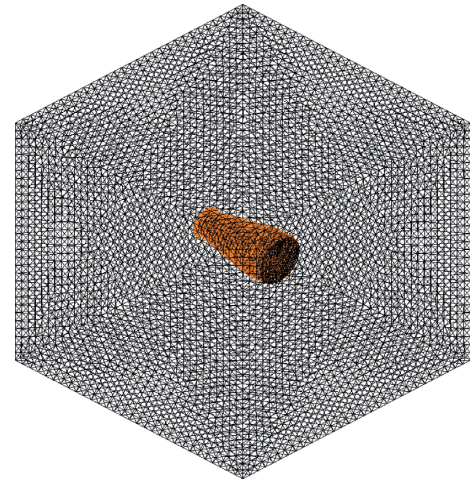

Figure 2: Fluid-structure coupled finite element model.

stiffened conical shell in this study. The technical specification of the computing hardware used to conduct the numerical simulation in this paper is Intel Core i5-9400F CPU with 8 GB RAM. To investigate the coupled effect between the shell structure and external fluid medium, the finite element model of water ($\rho_w = 1000\,\text{kg/m}^3$) is built by the acoustic finite element tetrahedral meshes, the size of which is $10\,\text{m} \times 10\,\text{m} \times 10\,\text{m}$, as shown in Figure 2. The middle part is removed for the shell structure. The conical shell that is located in the central part of the fluid medium is established by the structural finite element quadrilateral meshes. Besides, the inside of the conical shell is regarded as vacuum.

3. Underwater Vibration and Acoustic Radiation of the Ring-Stiffened Conical Shell

3.1. Vibration Modal Analysis in Vacuum. Prior to the acoustic radiation analysis, it is necessary to obtain the modes of the structure in vacuum. The results are presented in Figure 3. It is shown that the first two-order vibrations mainly occur on the shell, and the amplitudes of vibrations are small. Large radial vibration occurs only at the edge of the base web. Besides, the last six-order vibrations mainly occur at the base, which result from the vibrations of the web and ribbed slab, and the amplitudes are larger than those of first two-order vibrations.

3.2. Establishment of Model for Acoustic Radiation. In this section, the acoustic analysis of the ring-stiffened conical shell system is conducted, and the acoustic radiation field of the structure at different frequencies is studied. The sinusoidal exciting force is imposed normally on the plate of the base with amplitude of 100 Pa. The acoustic field model is built in the *xoy* and the *yoz* planes, respectively, the size of which is 20000 mm long × 20000 mm wide. The central axis of the conical shell coincides with the intersection of two fields. Besides, according to the ISO standard, the ISO acoustic field model is also established. The model is shown in Figure 4.

3.3. Results and Discussion from Different Acoustic Field Models. Due to the essence of FEM and restrictions of mesh, the frequency of 2970 Hz will reach the limit of the computer's calculation ability. Thus, the frequency range is from 50 Hz to 2950 Hz, and the step is 50 Hz. Figure 5 presents the distribution of sound pressure level (dB) corresponding to different frequencies in the *xoy* plane. It is obvious that the acoustic radiation field takes a symmetrical distribution around the central axis in the *xoy* plane. The largest radiated sound pressure occurs in the areas on both sides of structure, and the sound pressure in front of the shell takes the second place, and the one behind the shell reaches the minimum. This trend becomes more and more obvious as the frequency

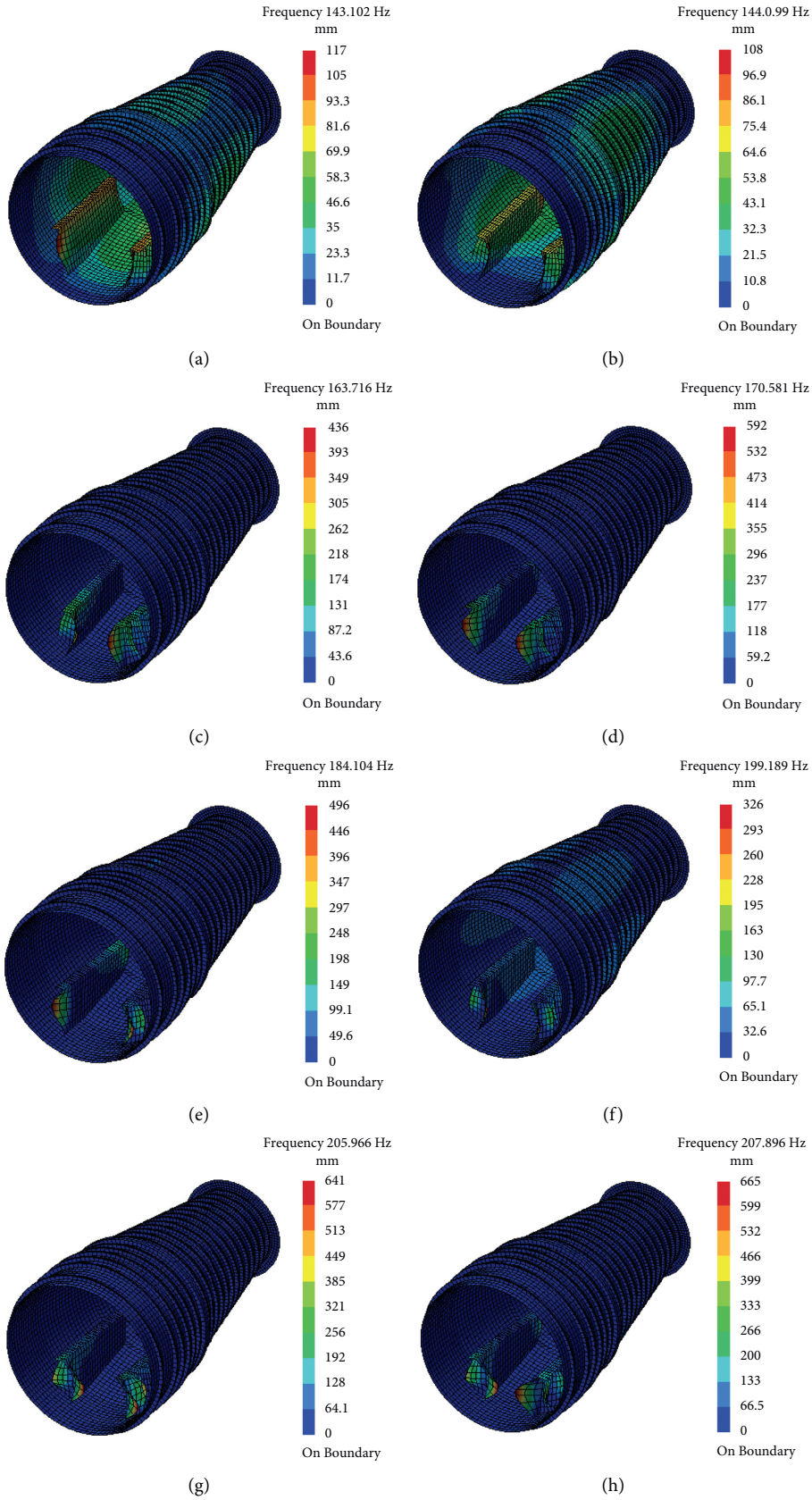

Figure 3: Modal shape of the ring-stiffened conical shell in vacuum. (a) The 1st order. (b) The 2nd order. (c) The 3rd order. (d) The 4th order. (e) The 5th order. (f) The 6th order. (g) The 7th order. (h) The 8th order.

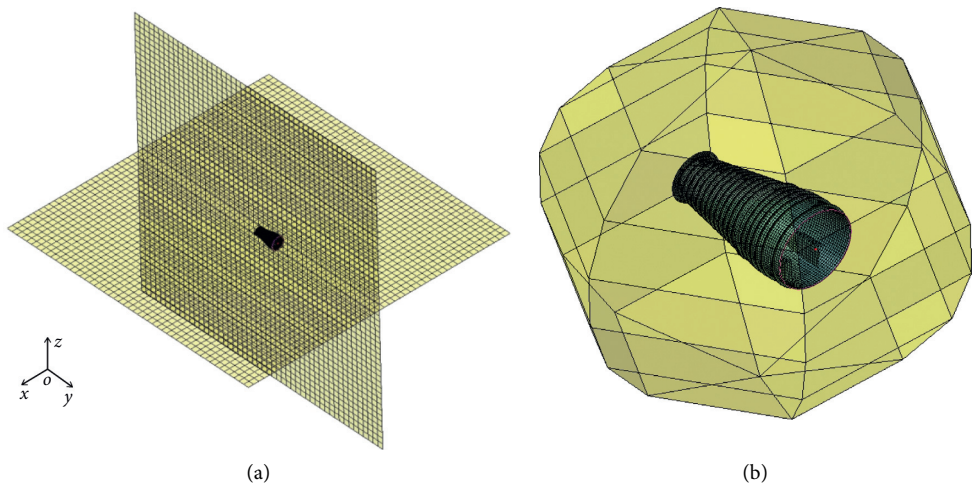

Figure 4: Models of acoustic field and structure. (a) Planar acoustic field model. (b) ISO acoustic field model.

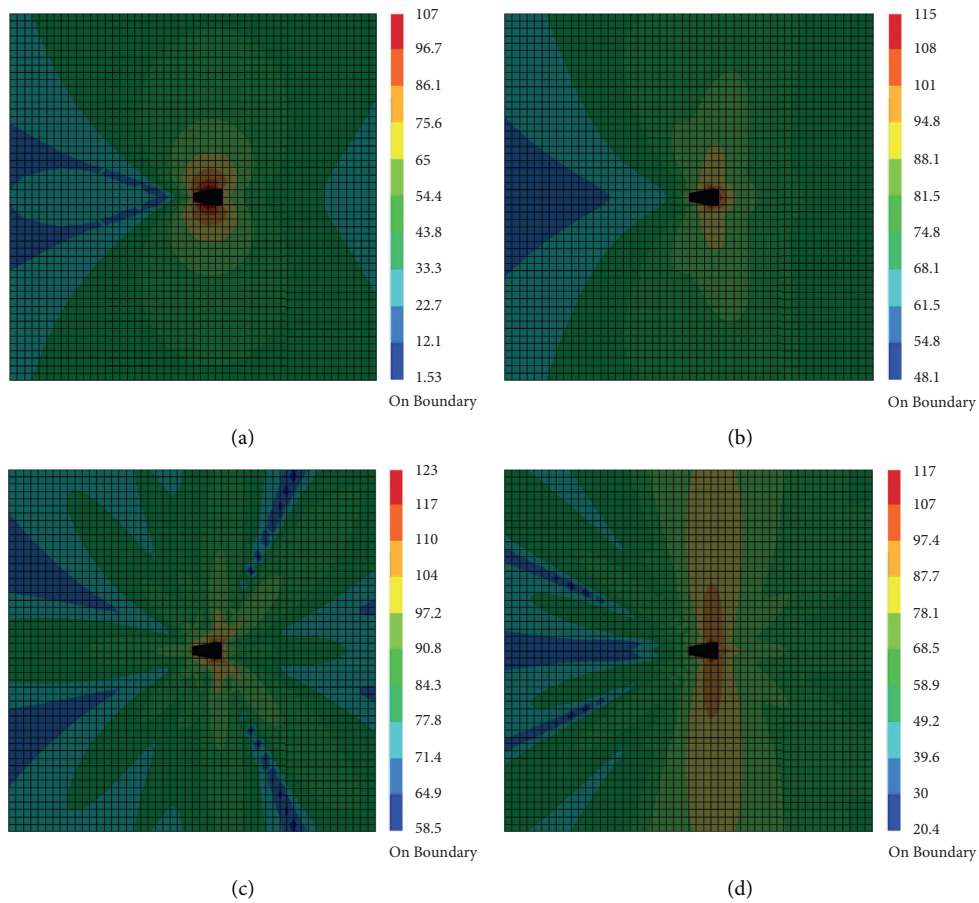

Figure 5: Acoustic radiation field at different frequencies in the *xoy* plane. (a) 50 Hz. (b) 1000 Hz. (c) 2000 Hz. (d) 2950 Hz.

increases. Besides, the higher the frequency is, the more the lobes of the acoustic radiation field are and the more complex the waveform becomes. This indicates that the modal shapes become more complex as the frequency increases. The acoustic field radiated by the ring-stiffened conical shell mainly propagates to both sides and is closer to the bases.

Figure 6 presents the distribution of sound pressure level in the *yoz* plane. On the whole, the distribution in the *yoz* plane is similar to that in the *xoy* plane. However, since the source is on the bottom of the shell, the acoustic radiation field is not asymmetrical, and the sound pressure below the shell is greater than that above the shell. Compared with the sound pressure level in the *xoy* plane, the sound pressure

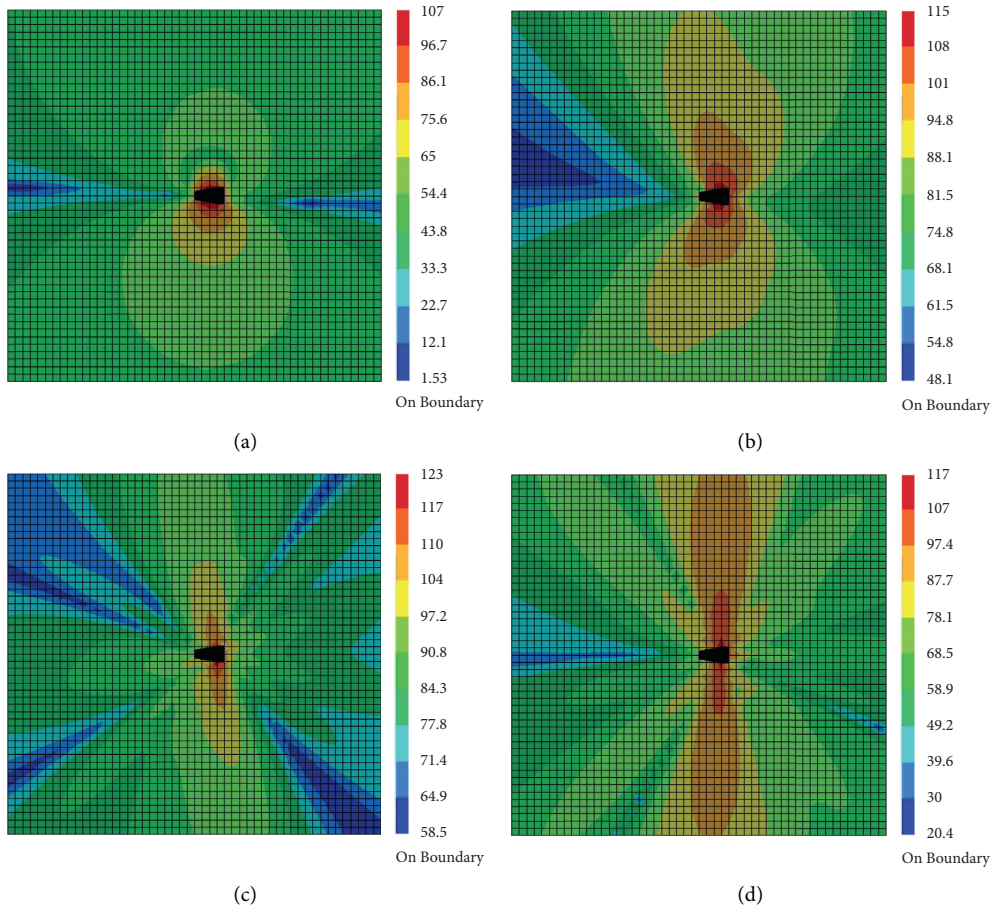

Figure 6: Acoustic radiation field at different frequencies in the *yoz* plane. (a) 50 Hz. (b) 1000 Hz. (c) 2000 Hz. (d) 2950 Hz.

below and above the shell is greater than that of each side at the same frequency. Thus, it can be seen that the sound radiated by the ring-stiffened conical shell travels further in both up and down directions.

In order to verify the conclusions above, the distribution of sound pressure level in the ISO acoustic field at different frequencies is calculated and presented in Figure 6, which shows the distribution of sound pressure at the same distance from the structure. The sound pressure below and above the shell is greater than that of other directions, and the sound pressure around the stern structure reaches the minimum. As discussed previously, the sound mainly spreads up and down, which has been further confirmed by Figure 7.

3.4. Changes of Sound Pressure with Frequency and Positions. The changes of sound pressure with frequency in different positions are further studied, which can provide more convincing evidence. The six sample field points in both the *xoy* plane and the *yoz* plane are selected to analyze the sound pressure level, as shown in Figure 8. Figure 9 presents the sound pressure level of the six field points. Obviously, the change of sound pressure level with frequency is in a relatively stable state of fluctuation. The sound pressure of Point *c* is the largest, and the sound pressure of Point *a* takes the second place, and the sound pressure of Point *b* is the lowest. So, we can conclude that the sound radiated by the shell mainly spreads to both sides, and the sound pressure in front of the shell is greater than that behind the shell in the *xoy* plane. Besides, although Point *f* is closest to the shell, the sound pressure of Point *f* is the minimum, while the sound pressure of Point *d* and Point *e* is almost the same. This also indicates that the sound pressure in both up and down directions is greater than that in front of the shell.

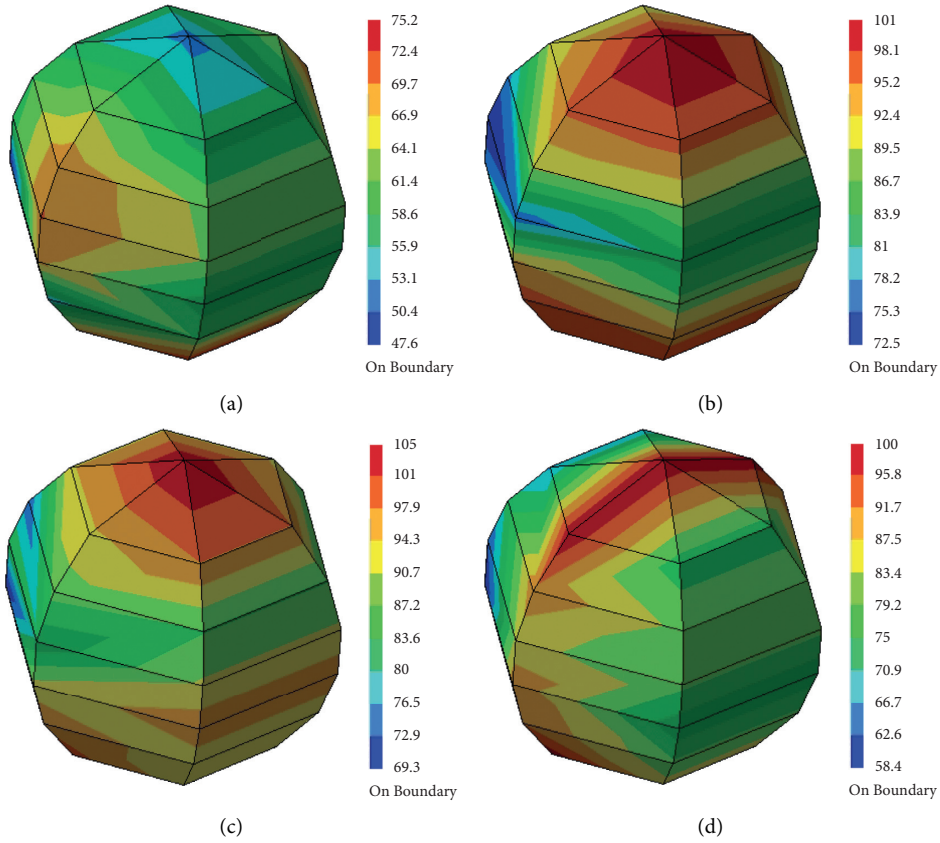

Figure 7: Acoustic radiation field at different frequencies based on ISO standard. (a) 50 Hz. (b) 1000 Hz. (c) 2000 Hz. (d) 2950 Hz.

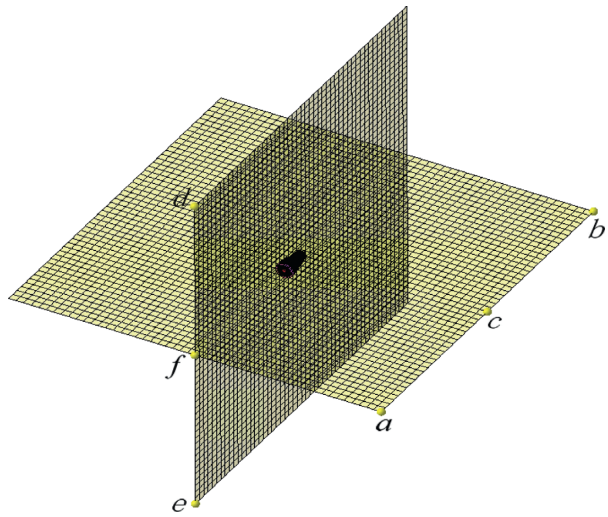

Figure 8: Six sample field points in the planar acoustic field.

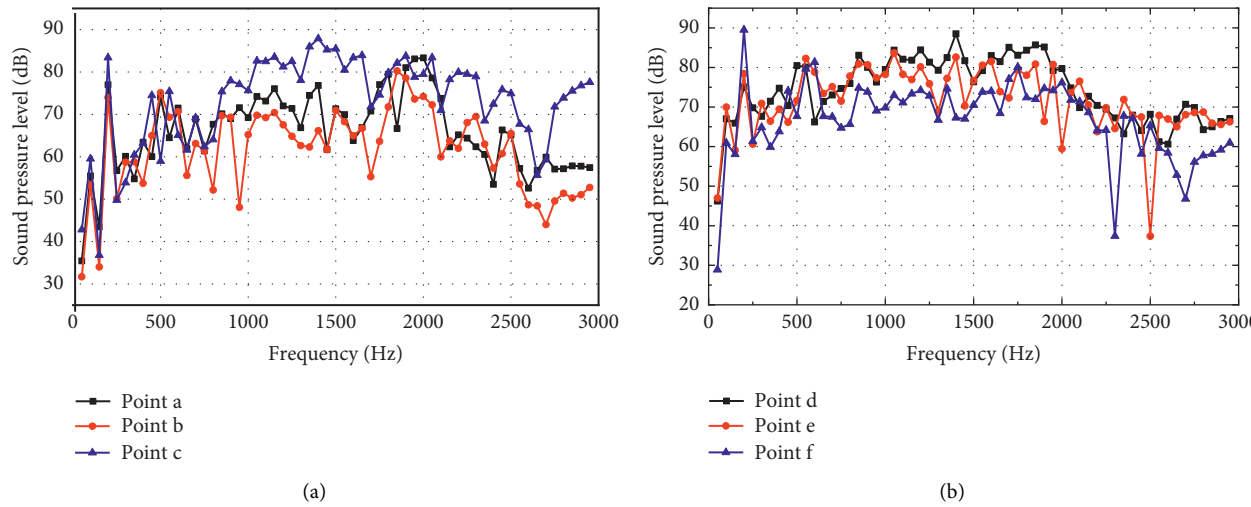

Figure 9: Sound pressure level of the six monitoring points with frequency. (a) In the *xoy* plane. (b) In the *yoz* plane.

4. Conclusions

A numerical analysis on the vibroacoustic responses of a typical ring-stiffened conical shell is carried out by using LMS Virtual.Lab. Some conclusions are drawn as follows:

(1) The first two-order vibrations mainly occur on the shell, and the amplitudes are small. The last six-order vibrations mainly occur at the base, which result from vibrations of web and ribbed slab, and the amplitudes are larger than those of first two-order vibrations.

(2) The distribution of sound pressure level obtained by the planar acoustic field model is the same as that of the ISO acoustic field model. The sound radiated by the structure mainly propagates to the side directions of the shell and propagates relatively less to the front side and the rear side. With the increase of the frequency, lobes of the acoustic radiation field become more and the waveforms become complex.

(3) Although some rules and conclusions obtained by this paper can provide an efficient tool for the analysis of the underwater acoustic radiation of the ring-stiffened conical shell, the physical model experiment is needed in the future for further validation.

Data Availability

All data, models, and codes generated or used during the study are available from the corresponding author upon request.

Conflicts of Interest

The authors declare that they have no conflicts of interest.

Acknowledgments

The authors acknowledge the financial support from the National Natural Science Foundation of China (grant no. U2006229) and Key Research and Development Program of Shandong Province (grant nos. 2019JZZY010125 and 2020CXGC010701).

References

[1] M.-S. Zou, Y.-S. Wu, and S.-X. Liu, "A three-dimensional sono-elastic method of ships in finite depth water with experimental validation," *Ocean Engineering*, vol. 164, pp. 238–247, 2018.

[2] Y.-s. Wu, M.-s. Zou, C. Tian et al., "Theory and applications of coupled fluid-structure interactions of ships in waves and ocean acoustic environment," *Journal of Hydrodynamics*, vol. 28, no. 6, pp. 923–936, 2016.

[3] W. Guo, T. Li, X. Zhu, Y. Miao, and G. Zhang, "Vibration and acoustic radiation of a finite cylindrical shell submerged at finite depth from the free surface," *Journal of Sound and Vibration*, vol. 393, pp. 338–352, 2017.

[4] C. Wang and J. C. S. Lai, "The sound radiation efficiency of finite length circular cylindrical shells under mechanical excitation II: limitations of the infinite length model," *Journal of Sound and Vibration*, vol. 241, no. 5, pp. 825–838, 2001.

[5] M. Chen, D. Luo, and X. Chen, "Analytical solutions of radiation sound pressure of double cylindrical shells in fluid medium," *Applied Mathematics and Mechanics*, vol. 23, no. 4, pp. 463–470, 2002.

[6] W. Desmet, *A Wave Based Prediction Technique for Coupled Vibro-Acoustic Analysis*, Katholieke University Leuven, Belguim, 1998.

[7] B. Pluymers, W. Desmet, D. Vandepitte, and P. Sas, "Application of an efficient wave-based prediction technique for the analysis of vibro-acoustic radiation problems," *Journal of Computational and Applied Mathematics*, vol. 168, no. 1, pp. 353–364, 2004.

[8] L. Chen, H. Chen, C. Zheng, and S. Marburg, "Structural-acoustic sensitivity analysis of radiated sound power using a finite element/discontinuous fast multipole boundary element scheme," *International Journal for Numerical Methods in Fluids*, vol. 82, no. 12, pp. 858–878, 2016.

[9] C.-J. Zheng, C.-X. Bi, C. Zhang, H.-F. Gao, and H.-B. Chen, "Free vibration analysis of elastic structures submerged in an infinite or semi-infinite fluid domain by means of a coupled

FE-BE solver," *Journal of Computational Physics*, vol. 359, pp. 183–198, 2018.

[10] L. W. Jiang, M. S. Zou, S. X Liu, and H. Huang, "Calculation method of acoustic radiation for floating bodies in shallow sea considering complex ocean acoustic environments," *Journal of Sound and Vibration*, vol. 476, 2020.

[11] S. Li and Q. Huang, "A fast multipole boundary element method based on the improved Burton-Miller formulation for three-dimensional acoustic problems," *Engineering Analysis with Boundary Elements*, vol. 35, no. 5, pp. 719–728, 2011.

[12] Y. Liu, J. Han, Z. Xue, Y. Zhang, and Q. Yang, "Structural vibrations and acoustic radiation of Blade-shafting-shell coupled system," *Journal of Sound and Vibration*, vol. 463, Article ID 114961, 2019.

[13] Y. Qu, J. Su, H. Hua, and G. Meng, "Structural vibration and acoustic radiation of coupled propeller-shafting and submarine hull system due to propeller forces," *Journal of Sound and Vibration*, vol. 401, pp. 76–93, 2017.

[14] M.-S. Zou, L.-W. Jiang, and S.-X. Liu, "Underwater acoustic radiation by structures arbitrarily covered with acoustic coatings," *Journal of Sound and Vibration*, vol. 443, pp. 748–763, 2019.